Université de Lille

Thèse de doctorat

Low-Frequency Ultrasound Device for Pressure Ulcers Early Stage Diagnosis by Skin Mechanical Impedance

Dispositif à ultrasons basse fréquence pour le diagnostic précoce des escarres par impédance mécanique de la peau

Thèse de doctorat de l'Université de Lille
École doctorale n°632 Sciences de l'Ingénierie et des Systèmes (ENGSYS)
Spécialité de doctorat: Génie Electrique (GE)

Thèse présentée et soutenue à Villeneuve d'Ascq, le 31 Mai 2023, par

ELIS MARINA SALES DE CASTRO

Composition du Jury :

Adrien Badel Professeur à Université Savoie Mont Blanc	Président
François Pigache Professeur à Ecole Nationale Supérieure d'Electrotechnique, d'Electronique, d'Informatique, d'Hydraulique et des Télécommunications	Rapporteur
Olivier Français Professeur à École supérieure d'ingénieurs en électrotechnique et électronique Paris	Rapporteur
Marie-Line Dahan Médecin gériatre, MD, PhD au Groupement Hospitalier de Territoire Grand Paris Nord-Est	Examinatrice
Pierre-Yves Rohan Maître de conférences at Ecole Nationale Supérieure d'Arts et Métiers	Examinateur
Masaya Takasaki Professeur à Saitama Univ. Graduate School of Science and Engineering, Japon	Examinateur
Frédéric Giraud Professeur à Université de Lille (L2EP)	Directeur de thèse
Betty Lemaire-Semail Professeure à Université de Lille (L2EP)	Co-directrice de thèse

To all the girls that albeit in an adverse context dare to dream of being scientists.

Acknowledgements

Inicialmente agradeço a minha família, meu pai Castor, minha mãe Elizane e meu irmão Elvis. Vocês são meu porto seguro. Obrigada por todo o amor e apoio que me trouxeram até aqui. Vovó Tina, dedico este estudo especialmente à senhora, meu coração está com a senhora sempre! Thank you, my Adrien, who supported and stayed by my side when I needed the most.

My french-brazilian family, thank you, for the time you all took to listen to me, life in Lille was easier and funnier because I have you here. And Patrícia, who not only take part on that, but also took some time to help me with my research. Thank you, Mogwai, for being the main soundtrack of my studies.

I would like to thank my supervisors, Professors Betty Lemaire-Semail and Frédéric Giraud, for the trust and guidance they gave to me. Also, Mr. Michel Amberg, that taught me so much and helped me so much. This project would not exist without you.

I thank my colleagues from L2EP, including ESPRIT and IRCICA! All the exchanges we had were important to the development of this project. And thank you for volunteering in my tests! Special thanks to Yisha, who more than a colleague became my sister!

Thank you, to the 'big guys' from STINTS, who guided, instigated and inspired us so much. Thank you, also, to all the ESRs: we have been through a lot, but it was fine because we were together. Special thanks to the team from Southampton, who hosted me and collaborated together. You all taught and motivated me so much!

I would like to thank the jury, Adrien Badel, François Pigache, Marie-Line Dahan, Masaya Takasaki, Olivier Français, and Pierre-Yves Rohan for the time to and availability given to read my thesis.

Finally, thank you, to all the researchers that came before me in this field (mostly named on my bibliography section), you built the foundation of this work. Thank you, also, to whoever took the interest to come and read all this. I hope I can help with the foundation of your own research.

Abstract

An important topic for the healthcare is skin integrity. Lesions brought on by pressure, shear, and friction over bony prominences, among other conditions, pose a threat to skin health. These wounds, namely Pressure Ulcers, take a long time and a lot of money to treat, which is bad for the patients' quality of life and expensive for the healthcare system. So far, PU diagnosis is made using imprecise methods, relying on the subjectivity of the healthcare staff. STINTS, a European Training Network funded by the Marie Skodowska-Curie Action, proposed various projects with the aim of comprehending the intricate biomechanical and biochemical pathways resulting in the loss of skin integrity, including the project presented in this thesis. The aim of this work is to develop a new device for early stage PU detection. The mechanical impedance measured through low-frequency ultrasound approach is yet unexplored in the field of chronic wounds. The device developed was used to analyse the data on healthy participants, to create a data set for healthy skin. Tests changing certain conditions of skin, such as hydration and microclimate creation were investigated and measurements of skin mechanics and other parameters, such as moisture and trans epidermal water loss were made. The findings from these tests, on healthy skin, indicate an association between skin parameters and the mechanical measurements. This study, however, has not taken into consideration patients in real risk of PU. Further studies are needed to investigate the diagnostic aspect in more detail.

Contents

General Introduction **1**

1 Introduction **4**

1.1 Pressure Ulcers: causes, risk factors and diagnosis 5

1.2 Low-Frequency Ultrasound on Pressure Ulcer Context 11

1.2.1 Sonophoresis – Transdermal Delivery 12

1.2.2 Debridement 13

1.2.3 Mechanical Stimulation Therapy 14

1.3 Skin Mechanical Properties 16

1.3.1 Skin description 16

1.3.2 Mechanical skin models 18

1.3.3 Studies on the *stratum corneum* 22

1.4 Skin tests on literature 24

1.4.1 Non-mechanical tests 24

1.4.2 Mechanical tests 26

1.5 Low-Frequency Ultrasound to Characterise Skin Mechanical Impedance 30

1.6 Chapter Conclusions 34

2 Low-Frequency Ultrasound Diagnostic Tool Design **36**

2.1 Langevin transducer, operating principle and modelling 37

2.2 Architecture of the Device 42

2.2.1 Low-frequency ultrasound generation 42

2.2.2 Conditioners and Sensors . . . 43
2.2.3 Normal force control . . . 46
2.3 Identification and Control of the System . . . 49
2.3.1 Electromechanical Model of the Langevin Transducer . . . 49
2.3.2 Identification of the parameters . . . 52
2.3.3 Controller Design . . . 55
2.4 Chapter Conclusions . . . 60

3 Acoustical Mechanical Impedance of Skin 62
3.1 Measurement Method . . . 62
3.2 Building the Protocol for Skin Tests . . . 69
3.2.1 Frequency of the probe . . . 69
3.2.2 Indentation force applied . . . 71
3.2.3 Matching layers . . . 74
3.3 Characterising SCH, TEWL and AMI on healthy skin . . . 76
3.4 Chapter Conclusions . . . 84

4 Skin Characterisation with Low-Frequency Ultrasound 86
4.1 Case Study: Distinguishing Skin in Two Sites . . . 87
4.1.1 Protocol . . . 88
4.1.2 Cohort of participants . . . 89
4.1.3 Results and discussion . . . 89
4.1.4 Study conclusion . . . 92
4.2 Case Study: what is the effect of Water, Razors, and Plasters on the skin? . . . 92
4.2.1 Protocol . . . 94
4.2.2 Cohort of participants . . . 95
4.2.3 Results and discussion . . . 95
4.2.4 Study conclusion . . . 98
4.3 Case Study: skin insulting with mechanical loading and tape-stripping . . . 99
4.3.1 Protocol . . . 101
4.3.2 Cohort of participants . . . 102

4.3.3 Results and discussion 104
4.3.4 Study conclusion 111
4.4 Chapter conclusions 111

5 Conclusions and Perspectives **113**
5.1 General Conclusions 113
5.2 Perspectives 116

A Appendix I **118**
A.1 Cohort for Palm - Forearm test 118
A.2 Cohort for WRaP test 119
A.3 Cohort for Soton test 120

List of Figures

1.1 PU at risk sites in different positions [1] 5

1.2 A diagram illustrating the vicious loop of cell and tissue destruction resulting in a PU [2] 6

1.3 PU stages and their deepnesses – adapted from [3] 7

1.4 Weekly mean total Pressure Ulcer Scale for Healing (PUSH) scores are shown by healing outcome [4]. 9

1.5 Braden PU scale [5] 10

1.6 Ultrasound range and its applications in healthcare 11

1.7 LFU cavitation bubbles in the skin medium [6] 13

1.8 Skin layers, with detail on their thicknesses. 17

1.9 A stress-strain curve of the skin, showing its different mechanical states, (I) elastic, (II) plastic, and (III) strain hardening phase [7] 18

1.10 Langer lines across the body [8] 19

1.11 Kelvin-Voigt skin model 19

1.12 Mechanical skin model considering an MDK system. Adapted from [9] 20

1.13 Typical curve for force against stress (penetration depth) using a nano-indenter [10] 21

1.14 *Stratum corneum* structure [11] 22

1.15 The variation of Young's Moduli (an elasticity unit) over the relativity humidity from the studies: [12, 13, 14, 15] – adapted from [16] 23

1.16 Resolution and penetration depth for skin imaging technologies, including OCT, presented in [17] 25

1.17 Biaxial test set-up of a mouse skin, presented in [18] 26
1.18 Skin tribometer device used in [19]: (a) schematic of the indentor; (b) indentation system and positioning of the subject's arm 27
1.19 Positioning for the rotating test presented in [20] 28
1.20 Set-up for tensile test *in-vivo* [21] 29
1.21 View of the probe used in [22], composed by an ultrasound scanner mode and a suction module 29
1.22 Observed values of acoustical force as a function of the vibration amplitude for 12 participants [23] 32
1.23 Displacement, separation distance, velocity, and acceleration of the skin interaction with an ultrasonic vibrating plate [24] 33
1.24 Comparison of real contact area optically estimated and of the plate impedance over two normal forces (1 and 3 N) and two ultrasonic vibration amplitudes.[25] . 33
1.25 Behaviour of the skin mechanical impedance Z_s and optically observed contact area A_O over different normal forces f_a applied.[25] 34

2.1 Langevin transducer's parts 38
2.2 Mason's electromechanical representation of a piezoelectric crystal, employing an ideal transformer. Adapted from [26] 39
2.3 Dynamic admittance in the Nyquist plane [27] 40
2.4 BVD schematic of a Langevin Transducer's electromechanical components . . . 40
2.5 Frequency sweep under different electric fields fro an LT [28] 42
2.6 Global architecture of SAMIS 43
2.7 Circuit of LFU input voltage supply 44
2.8 LT with a close look in the PE sensor and conditioner circuit for the strain sensor 45
2.9 Measurement of the displacement with a laser interferometer of the vibrating surface of an LT 45
2.10 Casing parts: bottom, always attached to normal force sensor, half of the central part, always attached to the LT, and assembled case 46
2.11 Results of a frequency sweep before and after casing the LT 47

2.12 Mounting structure: (A) LT and force sensor placement (B) holding arm, with a spring (C) tripod rod – to control the indentation force (D) tripod 48
2.13 GSV adapter and 3-axis force sensor 49
2.14 Equivalent mass-spring-damper model of the Langevin Transducer 49
2.15 Vibration displacement $W(t)$ represented in the rotating reference frame, rotating in a frequency ω 50
2.16 Frequency sweep for different amplitudes 52
2.17 Behaviour of the (a) velocity and (b) current, in the rotating reference frame for frequency variation, with a constant voltage V_d=12.47 V and V_q=0 54
2.18 Behaviour of the velocity, in the rotating reference frame for frequency variation, for a variety of voltage inputs V_d and $V_q = 0$ 56
2.19 Energetic macroscopic representation of a Langevin transducer 57
2.20 Energetic Macroscopic Representation (EMR) of the system (orange) with the controller structure (blue) and the tuning paths (in green and yellow) 57
2.21 Open loop step response, also for an initial $V_d = 2.08V$ and final $V_d = 12.47V$ and $V_q = 0$, at resonance. 58
2.22 Block diagram: system in (d, q) reference frame and vectorial controllers 59
2.23 Experimental and simulated results of a closed loop step response: (a) velocity (b) voltage 60

3.1 Mechanical skin model considering an MDK system 64
3.2 Acoustical mechanical force behaviour for a vibration increase: forearm skin of a healthy participant 66
3.3 Samples of Dragon Skin®10 NV, Dragon Skin 20 and Dragon Skin 30, designed for the preliminary tests 67
3.4 Acoustical force (g_r) of the 3 Dragon Skin elastomers as a function of the reference velocity U_{ref}: in red the d force component and in blue the q component . . 68
3.5 Probes tested for the device 70
3.6 Results of AMI on the forearm and palm of the hand using the LT probes of 40 kHz, 50 kHz and 60 kHz 71

3.7 Vibration velocity of the LT during a frequency sweep test for different normal forces 72
3.8 Set-up of the tests with the SAMIS 73
3.9 Relationship of indentation force and AMI for 0.2, 0.3, 0.4 and 0.5 N, in one participant's forearm. 74
3.10 Results of AMI before and after the application of matching layers, for 6 participants' forearms 75
3.11 Corneometer® CM825 probe and its measurement principle [29] 76
3.12 Above, tewameter sensors and principle of functioning. Below, the probe. [30] . . 77
3.13 Timeline for a simple trial 79
3.14 Absolute values of AMI for all the trials, for 13 participants 82
3.15 Correlation of SCH and AMI for the morning and afternoon tests, with linear trend lines 83
3.16 Correlation of TEWL and AMI for the morning and afternoon tests, with linear trend lines 83

4.1 Stress-strain (here named stretch) curves on the back of a human, presented on [31] 88
4.2 Sites tests for the palm – forearm test 89
4.3 Results for AMI on the palm and forearm 90
4.4 Results for SCH on the palm and forearm 91
4.5 Dynamic shear viscosity against frequency for skin from the back of the hand. Adapted from [32]. 93
4.6 Treatment and control sites in one participant 94
4.7 Timeline of the Water, Razor and Pad test (WRaP) tests 95
4.8 Results for AMI on the forearm for the different treatments 96
4.9 Results for SCH on the forearm for the different treatments 97

4.10 Magnets load, used to create a PU model on rats *in-vivo*. (a) Irreversible PU resulting from the loading, detected by both eye and devices assessment (b) Reversible PU with no visible trace, but detected by the devices (c) No damage detected. In the photos, dashed light blue circles indicate where the pressure was applied to the skin, orange, and dark blue hexagons indicate the location of the flexible and rigid arrays on the wound, respectively, and grey dots represent the electrodes [33] 99
4.11 Variation of measured elastic modulus, average TEWL value and average friction coefficient with number of tape-stripping [34] 100
4.12 Protocol for the insults testing 101
4.13 Set-up for the forearm intermittent loading – the black support for the arm was also used during the measurements 102
4.14 Loads used for the loading insult and set-up for SAMIS measurements 103
4.15 Insults to the lower back, delineating the inflammation marks 103
4.16 Correlation plots and respective R values, on the forearm 104
4.17 Box plot of SCH results for the control and 2 insults on the forearm, before the insults, right after insulting and after a 30-minutes recovery time 105
4.18 Box plot of TEWL results for the control and 2 insults on the forearm, before the insults, right after insulting and after a 30-minutes recovery time 105
4.19 Box plot of AMI results for the control and 2 insults on the forearm, before the insults, right after insulting and after a 30-minutes recovery time 106
4.20 Correlation plots and respective R values, on the lower back 107
4.21 Box plot of SCH results for the control and 3 insults on the lower back, before the insults, right after insulting and after a 30-minutes recovery time 108
4.22 Box plot of TEWL results for the control and 3 insults on the lower back, before the insults, right after insulting and after a 30-minutes recovery time 109
4.23 Box plot of AMI results for the control and 3 insults on the lower back, before the insults, right after insulting and after a 30-minutes recovery time 109
4.24 Results comparing AMI on the forearm and lower back (baseline sites), with p-value to show that the SAMIS can distinguish the 2 sites 110

4.25 Effect of inflammation with tape-stripping on the forearm and lower back: baseline, insult and recover 110

List of Tables

1.1 Results of PUSH scores for all ulcers and by healing outcome for week 1 measurements [4]. . . . 8
1.2 Summary of the Evidence Supporting LFU as an Adjunctive Therapy 14
1.3 Mechanical properties extracted from an interaction of force $g_r(t)$ with skin [35] . 20
1.4 Summary of skin tests 35

2.1 Resonance frequency for a variation on the input voltage 52

3.1 Dragon skin rubbers mechanical features 67
3.2 Dragon skin rubbers AMI 68
3.3 System and controller parameters for the three LT probes 70
3.4 Resonance frequency for a variation on the normal force applied 72
3.5 Cohort of participants for the repeatability test 80
3.6 Normality tests executed for AMI results 81
3.7 t-test results for morning and afternoon tests 82

4.1 t-Test found in the Palm – Forearm 91
4.2 t-Test found in the WRaP test – AMI 96
4.3 t-Test found in the WRaP test – SCH 98
4.4 Averages found in the WRaP test 98
4.5 One-way ANOVA forearm 104
4.6 One-way ANOVA lower back 107

A.1 Participant data for the Palm-Forearm test 118
A.2 Participant data for the WRaP test 119
A.3 Participant data for insulting tests 120

Acronyms

AFM Atomic Force Microscopy

AMI Acoustical Mechanical Impedance

ANOVA Analysis of Variance

BMI Body Mass Index

CW Chronic Wounds

DSP Digital Signal Processor

EMR Energetic Macroscopic Representation

HFU High-Frequency Ultrasound

ICU Intensive Care Unit

LFU Low-Frequency Ultrasound

LT Langevin Transducer

MI Mechanical Impedance

OCT Optical Coherence Tomography

PE Piezoelectric

PI Proportional and Integral Controller

PLC Polycaprolactone

PPE Personal Erotective Equipment

PU Pressure Ulcer

PUSH Pressure Ulcer Scale for Healing

SAMIS Skin Acoustical Mechanical Impedance Sensor

SC *Stratum Corneum*

SCH *Stratum Corneum* Hydration

SEM Sub-epidermal Moisture

STINTS Skin Tissue INTegrity under Shear

TEWL Trans-Epidermal Water Loss

WRaP Water, Razor and Pad test

Symbols

Y	Young's modulus
v_p	Poisson's ratio
i	Subscript denoting the indenter properties (in indentation skin test)
T	Torsion (in torsion skin test)
ϕ	Torsion angle (in torsion skin test)
R_d	Radius of the disk (in torsion skin test)
h	Skin thickness
$P_ext(t)$	Suction pressure (in suction skin test)
$\delta(t)$	Vertical displacement of the skin's surface (in suction skin test)
r_0	Aperture radius (in suction skin test)
σ_0	Initial stress (in suction skin test)
t	Time
σ	Stress in skin, from Kelvin-Voigt model
K_s	Elastic modulus of skin
D_s	Viscous modulus of skin
ω	Angular frequency
g_r	Reaction force
Z_s	Mechanical Impedance of Skin
$u(t)$	Vibration velocity
$a(t)$	Vibration acceleration
r	Radius of the indenter

E^*	Complex modulus
M	Mass coefficient of the Langevin transducer's model
D	Damping coefficient of the Langevin transducer's model
K	Spring coefficient of the Langevin transducer's model
N	Piezoelectric transformation factor
C_0	Intrinsic-damped capacitance of the transducer
$i_0(t)$	Input current of the Langevin transducer
$w(t)$	Vibration amplitude
$v(t)$	Voltage applied on the Langevin transducer
$\dot{w}(t)$	Vibration velocity
$\ddot{w}(t)$	Vibration acceleration
$i_s(t)$	Sensor's current
$v_s(t)$	Sensor's voltage
C_s	Sensor's capacitance
G_c	Current sensor gain
d	Subscript denoting the variables on the direct axis
q	Subscript denoting the variables on the quadrature axis
K_P	PI proportional coefficient
K_I	PI integral coefficient
$t_{5\%}$	Settling time
$CLTF$	Closed-loop transfer function
S	Hardness of a material in Shore A scale
AMI	Acoustical mechanical impedance, the real part of Z_s
$p-value$	Hypothesis testing
A	Surface (in TEWL measurement)
m	Water transported (in TEWL measurement)
C	Diffusion constant (in TEWL measurement)
p	Vapour pressure of the atmosphere (in TEWL measurement)
x	Distance from skin surface to point of measurement (in TEWL measurement)

G_{cv}, G_{cu}	Conversion factors of voltage and velocity
G_a, G_b	Discretized constants of the controller
T_s	Sampling period of the microcontroller

General Introduction

The skin integrity is a major subject for the healthcare system. Among some issues that challenge the skin health, pressure ulcers are wounds caused by pressure, shear and friction, over bony prominences. These wounds are very difficult to heal, which costs a lot of money and time for the healthcare system and is especially harmful for the patients' quality of life.

These wounds tend to appear on patients with low mobility, notably wheelchair users and Intensive Care Unit (ICU) patients, that stay long periods of time on a bed, and the occurrence of pressure ulcers in the latter situation can extend the stay of the patient in the hospital.

Although many efforts have been made over the years, it is still difficult to diagnose early stage pressure ulcers. Furthermore, the methods available nowadays are subjective to the healthcare professionals.

In this context, the Skin Tissue INTegrity under Shear (STINTS), a European Training Network from Marie Skłodowska-Curie Action (research and innovation programme under grant agreement No 811965), proposed different projects with the aims to understand the complex biomechanical and biochemical pathways leading to loss of skin integrity. To reduce the societal and financial costs of pressure ulcers, the projects involved understanding of skin behaviour, the design of more effective preventative aids, early stage diagnosis (non-invasive biomarkers and sensors, and smart materials). From the diagnosis axis of STINTS, the project presented in this thesis arose in University of Lille, in Laboratory of electrical engineering and power electronics (L2EP).

Knowledge on the skin mechanical behaviour under low-frequency ultrasound stimulation can be a clue to assess skin integrity. When the death of the cells starts, some of its mechanical characteristics change, as well as the interstitial fluids around them.

Piezoelectric devices have a wide range of application, such as ultrasonic cleaning, loudspeakers, voltage multiplier transformers, medical imaging or even electric cigarette lighters. In this project, a piezoelectric device was used to develop the Skin Acoustical Mechanical Impedance Sensor (SAMIS), with the aim to characterise the mechanical behaviour of the skin. Low-frequency ultrasound piezoelectric devices are the main field of research of the L2EP group located in Research Institute on software and hardware devices for information and advanced communication (IRCICA), mostly used to design tactile feedback plates and to analyse skin dynamics when in contact with haptic surfaces.

The SAMIS is then designed thanks to the scientific background of the team, but dedicated to skin mechanical characterisation for a medical objective. As the current version of the device is a prototype, it was only possible to assess healthy skin, which is a fundamental step before reaching a pressure ulcer at-risk population.

In Chapter 1, the aetiology, risk factors and consequences of PU are presented. Then, we introduce low-frequency technology in the context of skin healthcare, including mechanisms of cleansing of wounds, transdermal drug delivery and therapy. The mechanics of skin are also explored, showing the mechanical tests found in the literature, the model used for this project and specific studies on the *stratum corneum*, the layer of interest for early pressure ulcer diagnosis. A small introduction is made on the skin characterisation using low-frequency ultrasound, majorly focused on friction reduction and tactile devices.

The development of SAMIS is described in Chapter 2. The chapter starts with the Langevin transducer, as well as the presentation of its electrical and electromechanical models and the non-linearities of the PE ceramics. The architecture necessary to generate and measure the vibration on the device is detailed, including the schematic of the circuits and the sensors involved. Finally, the identification and control of the device are described. This chapter is closed with the identification and controller design of the device.

Chapter 3 explains of the methodology of measurements, once the device is properly controlled. Tests with phantom skins are presented to validate the probe and its measurements. In the chapter, it is also presented the many attaints made for the preparation of the protocol, considering the choice of the probe used, by testing three devices with different resonance frequencies. The normal force applied was also studied, as well as the need for an acoustic

propagating media. Once these parameters are set, experiments with healthy skin were made to evaluate the repeatability and reproducibility of the measures. The chapter is closed with the test of skin using the SAMIS, the Corneometer® and Tewameter® to provide a comparison of our measurements with other skin parameters, measured with commercial devices.

For the skin analysis in different conditions, tests presented in Chapter 4 were made. Three case studies are presented, to compare skin in different sites or conditions; firstly, tests comparing skin with varied features, as the skin over the body is different according to its site; then, skin before and after the application of water, after shaving and after the creation of a microclimate. The last case studied consisted of measurements of healthy skin after submitted to insults, such as loading and tape-stripping. The insults aimed to simulate damage over the skin, as the device was conceived, in the future, to be a medical tool.

Finally, the conclusions and perspectives of this project are pointed out. The efforts and the outcomes of this work are exposed, and hints to consolidate the hypothesis are suggested for the continuation of this research.

Chapter 1

Introduction

As a complex tissue composed by several layers, the skin is an organ responsible for the protection of the underlying tissues, regulation of the somatic temperature, reserve of nutrients, transport of water and sensitive nerve endings [36]. Skin integrity has, therefore, an important role in ensuring that this tissue performs its functions correctly.

External forces (friction, shear, and pressure), poor nutrition, and microclimate are examples of risk factors for the skin integrity that may lead to Chronic Wounds (CW), such as vascular ulcers, diabetic ulcers and Pressure Ulcer (PU) [37], [38]. These wounds not only reduce substantially the patients' quality of life, but also represent high costs on healthcare, depending on the size and duration [38].

In this chapter, the aetiology of PU is presented, as well as the current diagnostic methods for it. Then, Low-Frequency Ultrasound (LFU) in the context of CW, notably applied for treatment and recovering of skin integrity. Since the skin mechanical properties are important on its health study, the description and characterisation of its layers, as well as skin mechanical models are presented. Then, the current methodologies to assess skin properties, including mechanical and non-mechanical tests, are reminded. Finally, the use of LFU is for skin characterisation is described, which is the foundation of this project's hypothesis.

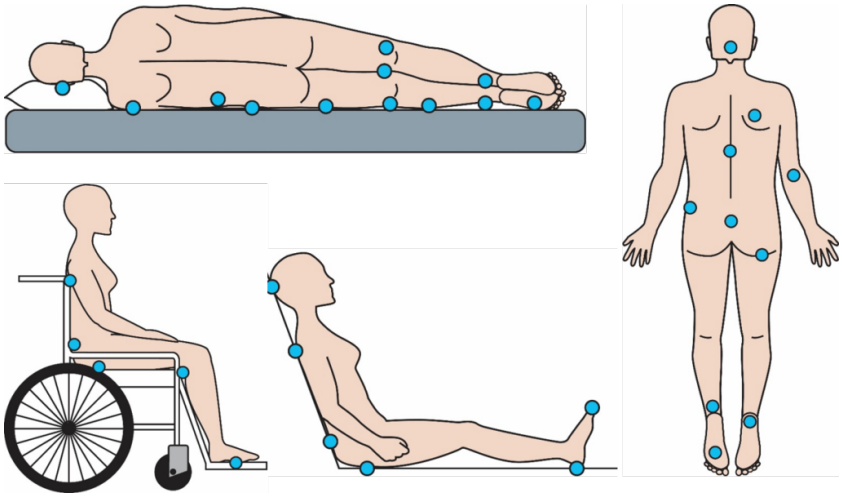

Figure 1.1: PU at risk sites in different positions [1]

1.1 Pressure Ulcers: causes, risk factors and diagnosis

PUs are wounds that happen mostly in patients with low mobility, such as wheelchair users and Intensive Care Unit (ICU) patients, who stay long periods of time in the same position. The common sites of PU risk are presented in Figure 1.1, since in these areas, there is a sustained pressure over a bony prominence: among them, the sacrum, and the heels are the sites of highest incidence of PU [39].

This pressure leads to tissue ischaemia and cell deformation, that ultimately lead to cell necrosis. Furthermore, a combination of shear and friction over skin may affect the underlying capillary bed, contributing to local tissue hypoxia [40]. Due to the nature of PU aetiology, the recuperation of the skin and underlying tissues is very difficult, as the blood flow is also damaged in that region. The vicious cycle of PU, as presented in Figure 1.2, begins with a triggering event caused by persistent mechanical deformations, which causes the primary, direct deformation damage (first damage event), which then causes secondary inflammatory-oedema-related damage (second damage event), which then causes tertiary ischaemic damage (third damage event) [2].

This type of wound is classified in several stages, according to its severity and deepness. Stage-I indicates the beginning of the wound, when only the outmost layers of the skin are affected. In stage-II, adipose or deeper tissues are not exposed yet, but partial damage to

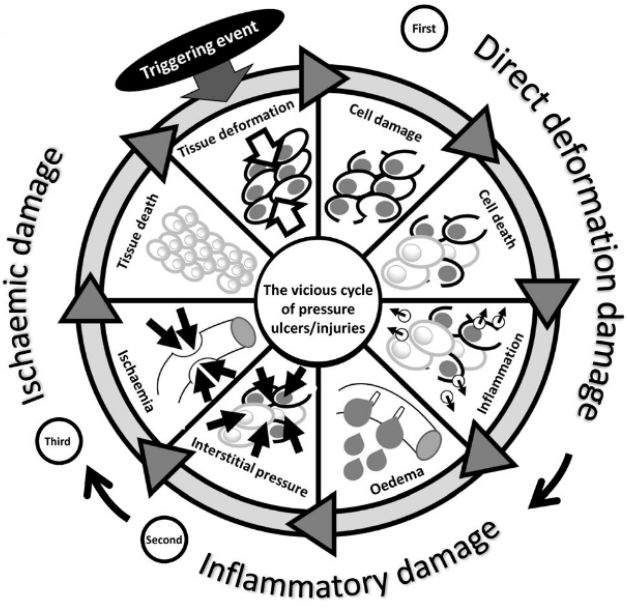

Figure 1.2: A diagram illustrating the vicious loop of cell and tissue destruction resulting in a PU [2]

the dermis is detectable. When adipose tissue becomes visible in the ulcer bed, the CW is considered in stage-III and when other tissues, such as muscle, tendon, ligament, cartilage, or bone are visible, the CW is classified as stage-IV [40]. The more severe the state of the wound, the more expensive and lengthy the treatment, which can cost up to thousands of euros or even, be unrecoverable. The advancements of PU stages are presented in Figure 1.3.

The main categories of PU treatment inculde the analysis of: positioning and support surfaces, nutrition, infection, wound bed preparation, dressings, and surgery [41].

Positioning and support surfaces rely on the fact that PUs result from the soft tissues being compressed against a bony prominence. It makes sense to believe that applying pressure to an ulcer may cause a delay in healing. In order to ease pressure on bony prominences, patients should be repositioned. Since it is unknown, the turning interval must be determined empirically. Although posture has been shown to reduce pressure incidence, its effectiveness is not universal [42]. To enhance the repositioning and relief of pressure in certain points of the body, support surfaces can be used [43].

Nutrition needs must be met through in order to support the development of granulation

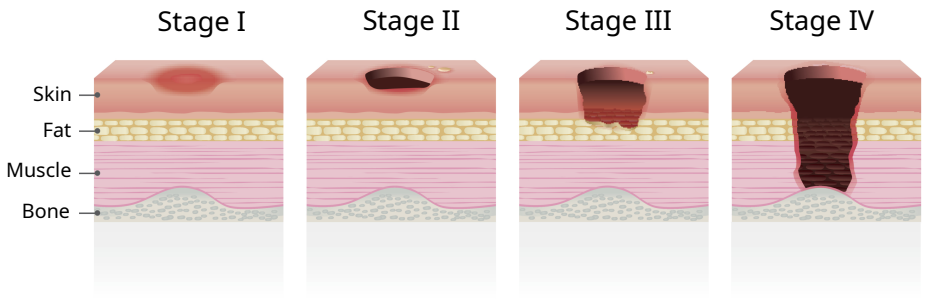

Figure 1.3: PU stages and their deepnesses – adapted from [3]

tissue. The patient's weight at the time of entry in the healthcare system is an excellent place to start. When a person's condition changes in a way that raises the possibility of undernutrition, it is important to evaluate body weight. The objective is to get as near to the ideal body weight as you can. To identify patients who are out of the ordinary, it is helpful to assess prealbumin levels (which represent recently consumed protein) and serum albumin levels (which reflect long-term protein consumption). Early detection of actual or probable nutritional need enables prompt management to prevent nutritional decline because undernutrition is linked to poor clinical outcomes, including an increased risk of mortality [44, 45].

Infection is a major problem in CW healing. It has been shown that beta hemolytic streptococci at any tissue level or at high concentrations inhibit a variety of wound-healing processes, including spontaneous healing and surgical closure of pressure ulcers. It is important to carry out cultures to separate both aerobic and anaerobic microorganisms [46].

Wound bed preparation is done by debridement and oxygenation of the wound. An environment with sufficient oxygenation and tissue perfusion will enhance wound healing. The supply of oxygen to the wound will be hampered by insufficient tissue perfusion [47]. Ohter inhibitors of wound healing include necrotic tissue, an increased bacterial load, senescent cells, and cellular debris. The type of debridement selected may be influenced by the state of the wound, the medical provider's skills and, the patient's general health [48].

Dressings are the protection put over a CW. It is essential for these materials to provide a moist wound-healing environment. In a wet wound environment, migration and matrix formation are physiologically encouraged, and autolytic debridement is encouraged, which speeds up

wound healing. Additionally lowering pain, moist wound healing [49].

Surgery of PU is a remaining invasive option. For lesions that have not responded to less aggressive care or when quick closure, this procedure is necessary. Pressure necrosis is caused by the compression of soft tissue between the skeleton and support surfaces. Pressure points are reduced when prominences are removed through a surgical treatment [50].

The lenght of the treatment may vary from patient to patient, and depends on the treatment applied. A Pressure Ulcer Scale for Healing (PUSH) was proposed by [51], as an instrument to measure the healing process of a PU. In [4], a study of PUSH in PU patients is presented. Their study only included participants residents from each of the sites who had a stage 2 or greater PU for a 6-month duration. The PUSH considered: length and width of the wound, exudate amount, i.e. ooze, pus or other secretion drainage that seeps from a wound, and tissue type. Table 1.1 presents the standard deviation on the amount of these characteristics on a PU when healed and unhealed. And, Figure 1.4 illustrates the weekly mean of PUSH scores measured on the study.

Table 1.1: Results of PUSH scores for all ulcers and by healing outcome for week 1 measurements [4].

	All ulcers (N=32)	Healed (N=21)	Unhealed (N=11)
Mean total PUSH score	8.6 ($\pm$3.06)	7.6 ($\pm$2.99)	10.5 ($\pm$2.30)
Length x width	5.6 ($\pm$2.33)	4.9 ($\pm$2.37)	7.0 ($\pm$1.48)
Exudate amount	0.4 ($\pm$0.49)	0.3 ($\pm$0.48)	0.5 ($\pm$0.52)
Tissue type	2.6 ($\pm$0.91)	2.4 ($\pm$0.87)	3.0 ($\pm$0.90)

The diagnosis of these wounds in early stages is commonly taken by visual assessment, using informatory forms such as the Braden scale [5], as presented in Figure 1.5. Lacking objective ways to estimate the PU risk, the nurses evaluate many factors such as the colour, the oedema, the firmness, the temperature, the presence of non-blanchable erythema, of bruising, of scaling and dryness, some characteristics of the skin that can indicate the presence of a PU. Other risk factors to PU are the sensory perception, nutrition, activity, mobility of the patient and the incidence of friction and shear [5].

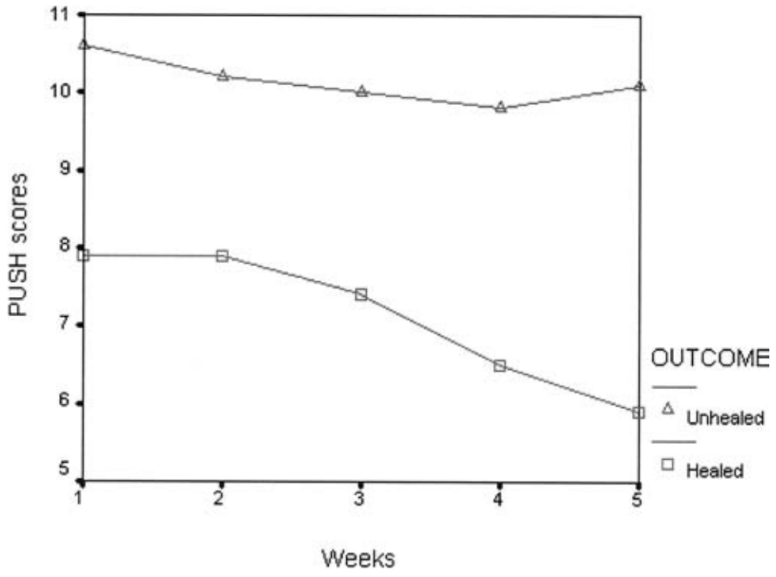

Figure 1.4: Weekly mean total Pressure Ulcer Scale for Healing (PUSH) scores are shown by healing outcome [4].

Although being the most used tool for PU diagnosis, visual assessment is subjective and demands much time from healthcare professionals. Furthermore, how to assess an erythema on patients with different skin colours? In these cases, stage I PUs are quite tricky to detect. Studies propose other techniques to determine the skin parameters and thus identify the risk of skin damage, such as imaging, bio-capacitance measurements or inflammatory biomarkers [52].

Skin mechanical parameters, e.g. viscoelasticity, damping effect, stiffness, can also indicate the presence of pressure ulcers [53]. Due to the degradation of the skin, changes in the consistency of damaged tissue changes may characterise a CW symptom [54]. However, to this day, no consistent study related these characteristics to PU.

The analysis of the mechanical behaviour of the skin using Low-Frequency Ultrasound (LFU) is in development. For many years, ultrasound for diagnosis is restricted to imaging, where the frequency range is high (> 1 MHz), while LFU in healthcare is mainly studied for therapy. However, if it is possible to analyse skin mechanics with this technology, then these findings can be applied in diagnosis field.

BRADEN SCALE FOR PREDICTING PRESSURE SORE RISK

Patient's Name _____ Evaluator's Name _____ Date of Assessment

SENSORY PERCEPTION ability to respond meaningfully to pressure-related discomfort	**1. Completely Limited** Unresponsive (does not moan, flinch, or grasp) to painful stimuli, due to diminished level of consciousness or sedation OR limited ability to feel pain over most of body.	**2. Very Limited** Responds only to painful stimuli. Cannot communicate discomfort except by moaning or restlessness OR has a sensory impairment which limits the ability to feel pain or discomfort over ½ of body.	**3. Slightly Limited** Responds to verbal commands, but cannot always communicate discomfort or the need to be turned OR has some sensory impairment which limits ability to feel pain or discomfort in 1 or 2 extremities.	**4. No Impairment** Responds to verbal commands. Has no sensory deficit which would limit ability to feel or voice pain or discomfort.
MOISTURE degree to which skin is exposed to moisture	**1. Constantly Moist** Skin is kept moist almost constantly by perspiration, urine, etc. Dampness is detected every time patient is moved or turned.	**2. Very Moist** Skin is often, but not always moist. Linen must be changed at least once a shift.	**3. Occasionally Moist** Skin is occasionally moist, requiring an extra linen change approximately once a day.	**4. Rarely Moist** Skin is usually dry, linen only requires changing at routine intervals.
ACTIVITY degree of physical activity	**1. Bedfast** Confined to bed.	**2. Chairfast** Ability to walk severely limited or non-existent. Cannot bear own weight and/or must be assisted into chair or wheelchair.	**3. Walks Occasionally** Walks occasionally during day, but for very short distances, with or without assistance. Spends majority of each shift in bed or chair.	**4. Walks Frequently** Walks outside room at least twice a day and inside room at least once every two hours during waking hours.
MOBILITY ability to change and control body position	**1. Completely Immobile** Does not make even slight changes in body or extremity position without assistance.	**2. Very Limited** Makes occasional slight changes in body or extremity position but unable to make frequent or significant changes independently.	**3. Slightly Limited** Makes frequent though slight changes in body or extremity position independently.	**4. No Limitation** Makes major and frequent changes in position without assistance.
NUTRITION usual food intake pattern	**1. Very Poor** Never eats a complete meal. Rarely eats more than ⅓ of any food offered. Eats 2 servings or less of protein (meat or dairy products) per day. Takes fluids poorly. Does not take a liquid dietary supplement OR is NPO and/or maintained on clear liquids or IVs for more than 5 days.	**2. Probably Inadequate** Rarely eats a complete meal and generally eats only about ½ of any food offered. Protein intake includes only 3 servings of meat or dairy products per day. Occasionally will take a dietary supplement OR receives less than optimum amount of liquid diet or tube feeding.	**3. Adequate** Eats over half of most meals. Eats a total of 4 servings of protein (meat, dairy products) per day. Occasionally will refuse a meal, but will usually take a supplement when offered OR is on a tube feeding or TPN regimen which probably meets most of nutritional needs.	**4. Excellent** Eats most of every meal. Never refuses a meal. Usually eats a total of 4 or more servings of meat and dairy products. Occasionally eats between meals. Does not require supplementation.
FRICTION & SHEAR	**1. Problem** Requires moderate to maximum assistance in moving. Complete lifting without sliding against sheets is impossible. Frequently slides down in bed or chair, requiring frequent repositioning with maximum assistance. Spasticity, contractures or agitation leads to almost constant friction.	**2. Potential Problem** Moves feebly or requires minimum assistance. During a move skin probably slides to some extent against sheets, chair, restraints or other devices. Maintains relatively good position in chair or bed most of the time but occasionally slides down.	**3. No Apparent Problem** Moves in bed and in chair independently and has sufficient muscle strength to lift up completely during move. Maintains good position in bed or chair.	

© Copyright Barbara Braden and Nancy Bergstrom, 1988 All rights reserved Total Score

Figure 1.5: Braden PU scale [5]

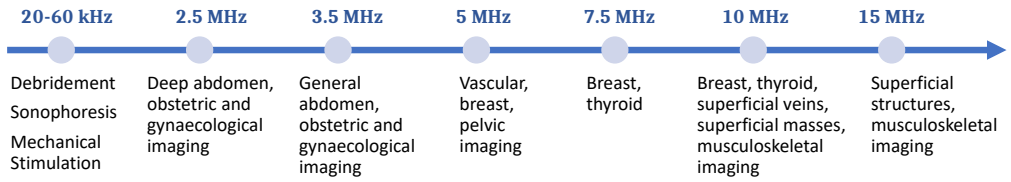

Figure 1.6: Ultrasound range and its applications in healthcare

1.2 Low-Frequency Ultrasound on Pressure Ulcer Context

The ultrasounds generated with Piezoelectric (PE) devices have a wide range of frequencies, and for each application there is a specific range used, as depicted in Figure 1.6. For example, imaging requires High-Frequency Ultrasound (HFU) and the depths of the images depend on the frequency used. The HFU imaging is obtained by the reflection of sound waves through tissue. Each tissue vibrates differently, according to its structure, vascularity, and density. Assessing these properties of skin tissues, it is possible to identify its keratin, collagen, and water content, for instance. In the ultrasound imaging field, the superficial anatomy of skin structures and neoplasms require a very high-frequency ultrasound. The tissues closer to the transducer are better seen using the highest frequency waves. Then, for dermatology, ultrasound is generally within the range of 13.5 to 100 MHz [55].

In skin healthcare, low and high-frequency ultrasounds have many applications. The former, typically ranging between 20 and 1000 kHz, is often used for therapy while high-frequency ultrasound ($>$1 MHz) is largely associated to imaging, even though it can also be used for sonophoresis [55].

The LFU device chosen for this project is a Langevin Transducer (LT). It uses the inverse piezoelectric effect to produce longitudinal vibrations, in the same direction of the applied field. Created in 1922 by Paul Langevin, it has a high conversion efficiency [56], using two metal bolts to amplify the displacement (that is usually tiny for PE materials). In this project, a LT is used to produce LFU, to characterise skin mechanical properties and, in a further application, hopefully for diagnosis of PU.

1.2.1 Sonophoresis – Transdermal Delivery

Transdermal delivery is a non-invasive path for drug administration. This method is beneficial because it avoids the degradation of molecules by the gastrointestinal tract and reduces the side effects of some dyspeptic drugs, in comparison to oral delivery. If compared to hypodermic injection, not only does it bypass the pain of the patients but also the risk of medical sharps, needle contamination and needle misuse [57].

The enhancement of skin permeability by sonophoresis is generated by LFU incidence. Vibration is transferred to the skin and the interstitial fluid, and this movement yields micro-bubbles by a phenomenon called cavitation. These bubbles serve as a carrier for molecules and particles inside the tissue. When produced by high frequencies, bubbles are regularly smaller and more abundant than the ones produced by LFU [57] and they can deliver only small molecules inside the body, i.e. the frequency range used for the cavitation is selected according to the size and quantity of the particles to be delivered.

Cavitation also makes the stratum corneum permeable because the bubbles formed and the vibration along the skin temporally change parameters such as the structure of the cell membrane function, and permeability [58]. It occurs mostly in the interface between keratinocytes and lipid bilayers [6].

The review published in [57] gathers studies using LFU to deliver molecules of different sizes and weights, for vaccination, hydrophilic permeants (e.g. sucrose), and particles (e.g. insulin). It is shown that, when varying the frequency and intensity of the LFU waves, bubbles with different sizes are generated. Thus, the LFU variables are tuned for each application. For example, high molecular weight molecules ($>$1000 g/mol) and particles require mostly a frequency of 20 kHz and intensity ranging from 0.1 to 50 W/cm^2. For hydrophilic molecules, the frequency ranges from 20 to 60 kHz and the intensities, from 1.08 to 7.5 W/cm^2.

Figure 1.7 depicts the effect of LFU application and the drug delivery over the skin. An advantage of this technique is that the parameters of skin permeability can be adjusted by changing the vibration frequency, intensity, and duration of exposure [6].

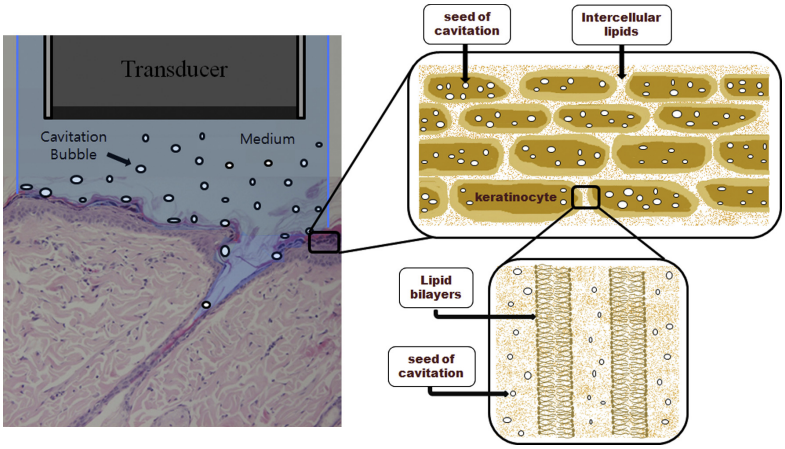

Figure 1.7: LFU cavitation bubbles in the skin medium [6]

1.2.2 Debridement

The debridement procedure is essential to the treatment of CW and consists of the removal of dead skin and bacterial biofilms. It is an expected and necessary component of wound care and aids wound bed preparation [59].

In CW, biofilms and unhealthy tissue cause infections and delay or impede the healing process. To remove these debris' layers, the process of debridement is applied, by surgical or autolytic/enzymatic mechanisms, exposing healthy tissue to the wound bed via epithelial cell migration. Debridement methods include autolytic, mechanical, surgical, hydro surgical and even larval [60], as well as ultrasound methods.

The treatment with non-contact LFU include a coupling medium between the device and the skin. The waves produced work as a non-invasive tool for the debridement of wounds. Due to its long wavelengths and high amplitudes – proportional to the input energy – LFU vibrations induce greater movements of the tissue molecules, producing cavitation and micro-streaming, which aid the debridement therapy.

In clinical environment, some commercial products, such as the Sonic One® are in use for in contact debridement of wounds. This precise product works at 22.5 kHz and is one of the most common devices for the removal of dead tissue and biofilms [61].

A systematic review [62] presented studies about debridement using LFU. The studies in the summary involved different types of wounds, considering acute types such as burn wounds

and trauma wounds. Among 25 papers, 9 mentioned the use of LFU on PU. A summary of the findings is shown in Table 1.2 (excluding 2 of them, that didn't have any evidence).

Table 1.2: Summary of the Evidence Supporting LFU as an Adjunctive Therapy

	Healing					Antimicrobial		Pain	Duration
Study	Complete Wound Closure	Decrease in Wound Size	Increase in Tissue Granulation	Increase in Rate of Healing	Improved Tissue Characteristic	Decrease in Exudate Amount	Decrease in Infection	Pain Decrease	
Bell and Cavorsi [63]		✓	✓			✓			4,3wk
Breuing et al.[64]		✓							3-8mo
Cole et al. [65]		✓	✓		✓	✓	✓	✓	2-18mo
Driver et al. [66]		✓		✓					–
Kavros et al. [67]	✓			✓					90d
Thomas et al. [68]				✓					4wk
Voigt et al. [69]				✓					–

The papers included in the review consider the complete wound closure, decrease in wound size, increase in tissue granulation, increase in rate of healing, decrease in infection and pain decrease. Most of the studies point out that LFU debridement can decrease the size of a wound and increase its rate of healing. One study indicates a complete wound closure. However, the results expected require a long duration and consistent treatment, having sessions at least 3 times a week.

Thus, studies denote that LFU, through different mechanisms, is advantageous to the treatment of CW. Hopefully, in this case of study the results will also be positive, since the device developed aims not only identify but also complement treatment of PU.

1.2.3 Mechanical Stimulation Therapy

The benefits of LFU treatment in the proliferative healing phase are due to mechanical stimulation, which activates the fibroblasts cells, generating collagen over the wound. Fibroblasts, the

major cell type in connective tissue, are crucial for the restoration and remodelling of an injured tissue.

The energy radiated from ultrasound is converted to mechanical and heat energy and is absorbed by tissues – notably the ones containing high amounts of protein and collagen, improving the healing process due to tissue extensibility and increased blood flow [70]. However, it is important to consider the parameters of LFU application, due to the risk of hot spots, burns or endothelial injury caused by excessive heat. Deeper tissues can also be reached by therapeutic LFU, when using higher intensities. Treatments in these internal injuries are enhanced by the effects of collagen production and extensibility, enhance of enzymatic activity, higher cell membrane permeability and nerve conduction velocity, achieved by the use of LFU [71].

The LFU therapy by stimulation of cell activity can induce cell angiogenesis, acting in the initial inflammatory to proliferative stage. In the first phase, the LFU non-thermal effects produce degranulation of mast cells that are sensitive to mechanical stimulation. The activation of these cells releases inflammatory mediators, such as histamine, serotonin, heparin, and serine proteases, results in the destruction of infectious agents [72].

Although using *in vitro* analysis of rat cells, in [73], the effects with different ultrasound intensities were analysed to establish the ideal radiation level. The tests were performed in the fibroblasts cells, and it was shown that the irradiation of 1 MHz ultrasound reflected an increase of the number of living cells in the culture. The models were divided in four groups varying the intensity of 0.2 or 0.6 W/cm^2 in pulse mode (duty cycle of 10% and 20%) to stimulate fibroblasts and cell repair.

Another study with *in vitro* tests [74] has proposed that LFU can stimulate the regeneration of skin by increasing the keratinocyte growth factor (also due to fibroblast trigger). In this case, the cell culture included dermal fibroblasts from neonatal foreskin. The ultrasound probe was tuned with 0.002 W/cm^2 and 40 kHz. The experiments led related that the keratinocyte growth factor was indeed increased after LFU treatment.

For human testing, the work of [75] evaluated LFU therapy in CW. The subjects selected for this study were receiving wound care in a single, hospital-based outpatient wound program. To assess and follow the microcirculation and tissue oxygenation, baseline TcPO 2 and Perimed PIM 2 scanner testing were performed. The LFU MIST® therapy [76] chosen was characterised

by 40 kHz of frequency and 1.25 W/cm^2 of intensity. Between the device and the wound, a coupler of sterile saline in a disposable reservoir was used, creating a vaporized mist. The outcomes of this research were optimistic regarding the use of LFU in CW. The tests have shown that the microcirculation and oxygenation were improved, plus early reduction in wound size was correlated with an increase in angiogenesis in the wound bed, due to the mechanisms explained in this section.

LFU in healthcare is highly used for CW treatment. The mechanisms of healing are diverse (debridement, heat, stimulation of fibroblasts, etc) and they act simultaneously, thus it is difficult to separate the effects from each other. The use of LFU in the diagnosis of CW is not found in literature, to our knowledge, but, as it is described in the next subsection, it can be used for skin characterisation.

1.3 Skin Mechanical Properties

Skin functions include barrier against pathogens, UV light, chemicals, temperature. The skin also regulates the amount of water released and ensures the protection of the organs and adipose tissue against mechanical external aggressions [77]. Therefore, its mechanical properties can be a skin integrity assessment tool.

1.3.1 Skin description

The skin is a multilayered tissue that changes over the body location. Mainly, we can distinguish hairy and glabrous skin. In Figure 1.8, the layers of skin in a hairy site, i.e., non-glabrous skin, is illustrated.

In the figure, the layers presented start with the outmost layer of skin, the *Stratum Corneum* (SC); it is thin, firm, naturally wrinkled and composed by dead piled keratinized cells, the corneocytes. Then, the viable epidermis, highly connected to the SC, and also naturally wrinkled. The dermis, the main layer of skin, is composed by connective cells and its mechanics are characterised as elastic and naturally contracted. The hypodermis, the deeper layer of skin, is filled with adipose tissue and behaves as a cushion, protecting the organs [8].

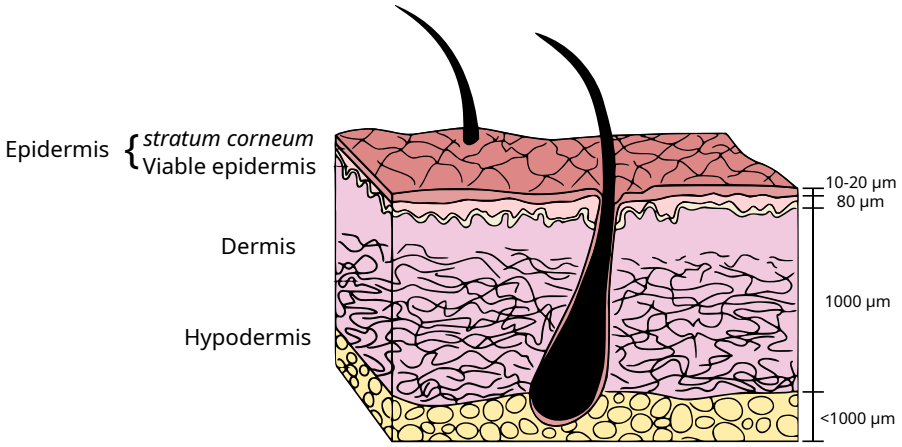

Figure 1.8: Skin layers, with detail on their thicknesses.

At some points of the body, such as the palm of the hands and the sole of the feet, the skin, namely glabrous skin, is thicker, does not have hair and has an additional layer, the *stratum lucidum* [77]. The mechanical properties of skin depend on the site studied, moisture content, age, gender, or even pigmentation. In [78], for instance, tests with 300 participants have shown that the skin's elastic ability to recover after stretching is highly affected by the age. In [9], it was demonstrated that the viscosity of skin is highly related to the skin site tested.

For mechanical matter, skin is considered as a viscoelastic tissue, having elastic (ability to resist a stress and to return to its original size and shape, once the stress force is removed) and viscous (resistance to deformation at a given rate) material properties. The elasticity is related to the energy storage, while the viscosity is associated with the energy loss of the mechanical energy applied.

When the skin is submitted to a stress, then a strain deformation appears, until a failure point, where the tissue breaks. A curve that characterises stress over strain of the skin is presented in Figure 1.9. On the figure, the skin behaviour is divided in states, where (I) represents the elastic phase, (II) is the plastic phase and (III) is the strain hardening phase, before the failure.

The viscoelastic properties of skin vary according to the site, type of test and direction studied, as the skin is an anisotropic tissue. In a skin study, based on the stabbing of cadavers, Karl Langer [79, 80, 81] found wounds consistently oval. Relating the shape and direction of the wounds, he inferred that the skin has different tension lines across the body and created a

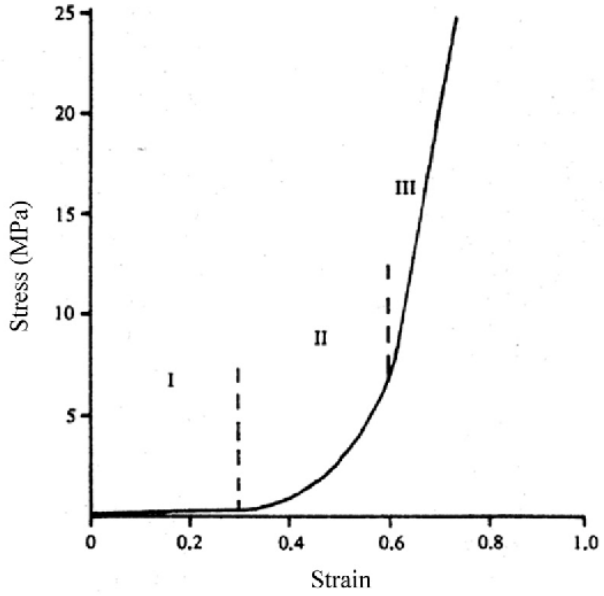

Figure 1.9: A stress-strain curve of the skin, showing its different mechanical states, (I) elastic, (II) plastic, and (III) strain hardening phase [7]

map of the anisotropic behaviour of human skin according to these lines, named Langer lines, as presented in Figure 1.10. Later, it was found that collagen and elastin fibres on the skin are predominantly arranged in the direction of these lines [82].

The Langer lines are important not only for the study of skin, but also for surgical incisions' orientation, for instance, as the direction of the incision highly affects the healing time, as well as the aesthetics of the scar, for the patients [83].

Tests on literature are proposed to study the numerous mechanical characteristics of skin through different types of stress. Each technique has a model, properties to be considered, advantages and drawbacks. The next subsection presents the most important ones.

1.3.2 Mechanical skin models

The Kelvin-Voigt skin model (Figure 1.11) is an established mathematical skin model, where D_s denotes the viscous modulus and K_s, the elastic modulus of the skin, varying with the angular frequency ω, when the skin is submitted to a vibrating stimulation of force $g_r(t)$ and vibration velocity $u(t)$. It consists in the linearization of the viscoelastic properties.

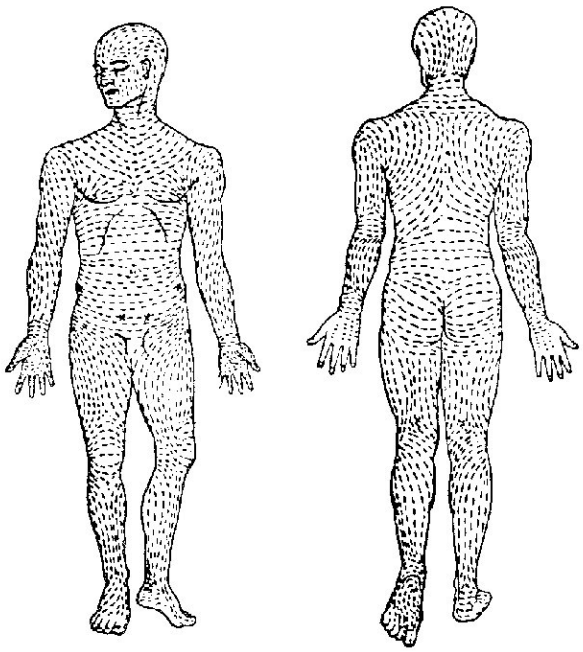

Figure 1.10: Langer lines across the body [8]

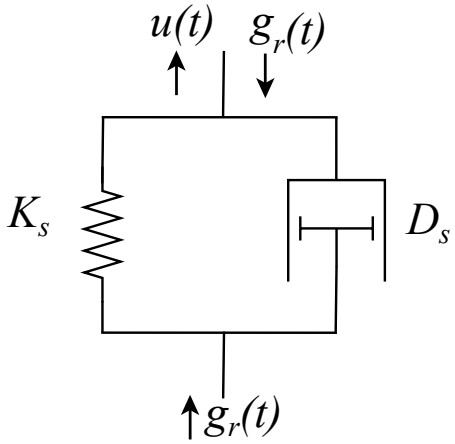

Figure 1.11: Kelvin-Voigt skin model

The model presented in the figure is also known as the “generalised one branch Kelvin-Voigt model”, because the model can also be presented with a network of branches [84, 85], or include a mass on the system, as it is presented in Figure 1.12 [86, 9].

One common way to study the skin mechanics is to apply forces over it and do measurements of its viscoelastic parameters. When a sinusoidal force ($g_r(t)$) is applied to a surface,

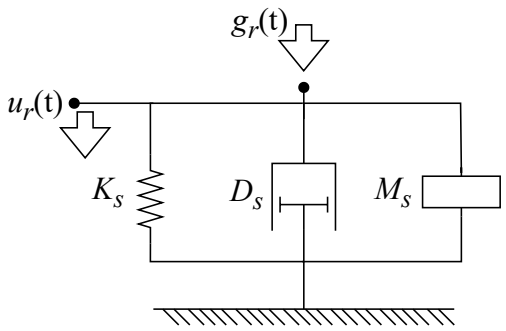

Figure 1.12: Mechanical skin model considering an MDK system. Adapted from [9]

such as skin, the stress ($\sigma(t)$) is yielded by a movement with the velocity, $u(t)$ and an acceleration $a(t)$. From this interaction, some ratios are interesting to describe a dynamic system. Table 1.3 presents these properties and the relationships that define them.

Table 1.3: Mechanical properties extracted from an interaction of force $g_r(t)$ with skin [35]

Mechanical impedance	$g_r(t)/u(t)$
Dynamic stiffness	$g_r(t)/\sigma(t)$
Apparent mass	$g_r(t)/a(t)$
Mobility	$u(t)/g_r(t)$
Compliance	$\sigma(t)/g_r(t)$
Inertance	$a(t)/g_r(t)$

When studying the dynamic stiffness/compliance of the skin, for a whole cycle of a loading test (load and unload), a different response is expected for each part of the cycle, highlighting an hysteresis phenomenon. Figure 1.13 presents a typical hysteresis for a loading and unloading of skin. This effect is due to the nature of the skin, as a connective tissue, composed by elastin and collagen fibres. This category of tissue is characterised by a load-history dependent behaviour [87], meaning that the loading curves of the skin depend on previous loading.

When analysing the Mechanical Impedance (MI), defined as the relationship between the sinusoidal vibration velocity and the force, a more linear behaviour is found, one of the advantages that makes this property be elected for our study. The mechanical impedance is presented in

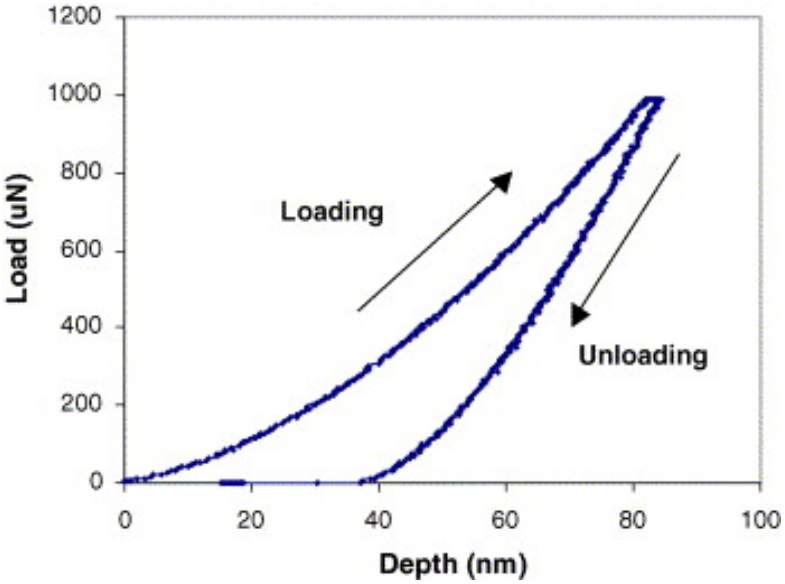

Figure 1.13: Typical curve for force against stress (penetration depth) using a nano-indenter [10]

(1.1).

$$Z_s(t) = \frac{g_r(t)}{u(t)} \tag{1.1}$$

Representing this model in the frequency domain, according to the Kelvin-Voigt model, we have (1.2):

$$Z_s(j\omega) = D_s + \frac{K_s}{j\omega} \tag{1.2}$$

The analogy of MI with electrical impedance is based on the analogy of force with voltage and velocity with current [35]. In this system, D_s is proportional to the power dissipated, in the form of heat, while K_s is the component that does not dissipate power, simply stores energy either in the potential form.

Representing the complex modulus $E*$ in terms of D_s and K_s, and considering an indenter with radius r, we have [88]:

$$E^* = E^{*'} + jE^{*''} \tag{1.3}$$

$$E^{*'} = \frac{K_s(\omega)}{2r} \tag{1.4}$$

$$E^{*''} = \frac{D_s(\omega)\omega}{2r} \tag{1.5}$$

It is expected that for different viscoelastic materials the MI will also be different. Thus, it should be possible to identify some properties of the skin, and its condition, simply by measuring its MI.

Note that most of the studies of skin consider it as a homogeneous material. However, in the study presented here, we aim to analyse only the epidermis mechanics, especially the SC. The device proposed for the project is intended to detect the wounds in an early stage.

1.3.3 Studies on the *stratum corneum*

The outmost layer of skin, the SC, has a particular arrangement of cells, named “brick and mortar”. The dead cells composing this layer, the corneocytes (represented by the bricks), are embedded in a lipid matrix (represented by the mortar) as depicted in Figure 1.14. This part of the skin, as its first layer, is highly related to the barrier functions [89].

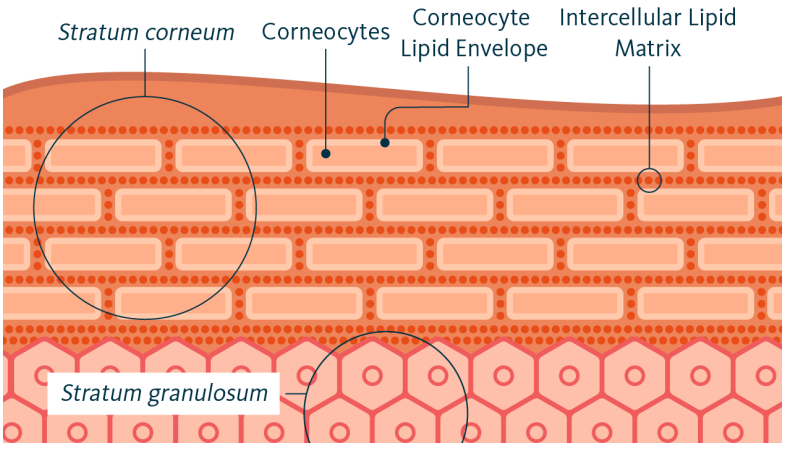

Figure 1.14: *Stratum corneum* structure [11]

The corneocytes are often replaced, since the epidermal cells migrate upwards to the skin surface as they die. Due to this constant change of cells, the structure, and composition of the

layer are also affected. The deeper layers of SC are thicker and more fragile than the outmost layers, which results in a higher influence on its overall mechanical behaviour [16].

A particularity found in the SC mechanics is the influence of the environmental relative humidity over its stiffness, in Young Modulus. In [90], loading tests were performed *in-vivo*, on the back of the hand, and the hysteresis loops of skin changed with the addition of moisture, and they found a substantial apparent softening of the skin. In Figure 1.15, an overview of this parameter in different *in vitro* studies is reported. It can be noted that the stiffness decreases with the increase of relative humidity. Moreover, it was found that the SC water content can reach up to 60% of the relative humidity, and up to twice its own thickness when fully hydrated [91], which might also reflect on its mechanics.

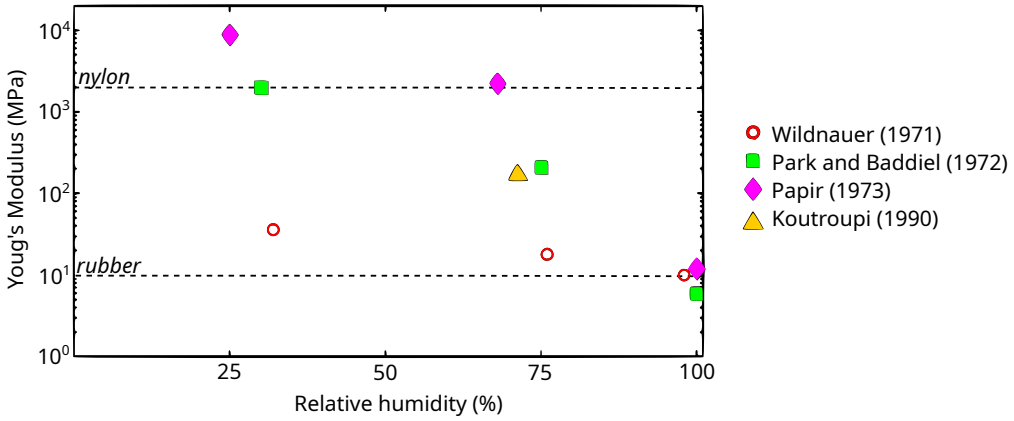

Figure 1.15: The variation of Young's Moduli (an elasticity unit) over the relativity humidity from the studies: [12, 13, 14, 15] – adapted from [16]

The results presented in [32] also suggest a relationship between moisture and both propagation velocity and damping length of ultrasound waves. This is explained by the softening effect of water on *stratum corneum*, which also reduces the skin viscosity, decreasing the propagation velocity. The studies presented in [92] and [93] also highlight this phenomenon as a change in the friction coefficient of a fingertip: it varies by more than one order of magnitude depending on dry or moist skin conditions.

As for the cells structure and the barrier functions, in [94], in vivo tests showed that the application of mechanical stress to the skin has an important influence in the water permeability of the epidermis (Trans-Epidermal Water Loss (TEWL)) and that the reciprocal relation is true.

Thus, the mechanical properties of skin suffer from variations when the barrier functions are compromised. The conclusions of [94] suggest an increase in the permeability from stretching the skin due to disorganisation of the SC cells.

1.4 Skin tests on literature

1.4.1 Non-mechanical tests

The study of the skin involves different parameters, depending on what is to be examined. For inflammation investigation, many studies have used the evolution of some molecular markers, such as the IL-1α – a cytokine produced by epithelial cells to yield inflammation, and accelerating the process of wound healing [95]. Evidence shows that for diaper rash, heat rash and erythema, the ratio of IL-1α/other proteins varies, when compared with healthy skin [96]. In the context of PU, Sebutapes®(a method to assess skin surface sebum levels) have been used to evaluate the IL-1α on the skin, and to investigate damage after skin suffers from mechanical loading or shear [97, 98]. In STINTS project, the team from University of Southampton uses IL-1α as one of the parameters to inspect PU incidence [99], developing a new methodology to extract these molecules for inflammation assessment [100].

Hydration is a crucial property of skin health; although when in high levels, it is a risk factor for PU [52], when moisture content is below a critical value, then it produces the accumulation of corneocytes on the cutaneous surface and, ultimately, a desquamation of skin [101]. Therefore, the study of water content on the SC is interesting when addressing to skin integrity, as this layer is the responsible for the water exchange with the environment. The measurement of *Stratum Corneum* Hydration (SCH) is highly documented in the matter of skin healthcare, and particularly for PU risk, it is a significant evaluation tool.

A phenomenon to evidence a proper skin barrier function is the TEWL. Related to SCH, TEWL measures the transport of water and heat from the skin to the environment. When the skin integrity is compromised, its TEWL increases [102]. The incidence of skin damage and TEWL level changes is reported in [103], where tests using a Tewameter®, a probe capable of measuring TEWL, were proposed. The study focused on skin damage due to Personal Ero-

tective Equipment (PPE) – respiratory masks, during COVID-19 pandemic. A 3-day monitoring was established to evaluate facial skin on bony prominences of healthcare workers, as they use PPE for long periods. Over the time, some participants presented changes in the levels of TEWL, which might indicate tissue damage on the area.

Another tool to identify skin inflammation is the Optical Coherence Tomography (OCT), investigated in STINTS project, also by the team from University of Southampton, in association with Philips, on the context of sensitivity of skin after shaving. The imaging of skin using OCT has been associated to oedema (fluid retention and swelling of skin) and erythema (redness) investigation [104, 105]. However, the imaging resolution of these measurements are not superficial enough to evaluate SC, as depicted on Figure 1.16, focusing on deeper sub-dermal layers [17].

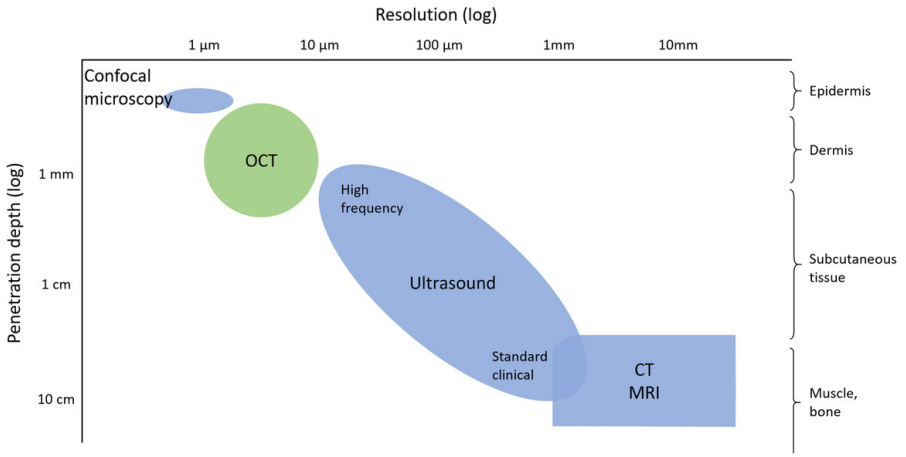

Figure 1.16: Resolution and penetration depth for skin imaging technologies, including OCT, presented in [17]

As presented in the figure, an interesting technology for skin analysis, notably the outmost layers, is using the microscope. In STINTS, the team from University of Birmingham used Atomic Force Microscopy (AFM) and DMRBE microscope, associated to fluorescence, to analyse the corneocytes cellular structure and maturation, respectively [89, 106]. In a study to address the skin damage due to the extensive use of personal PPE of healthcare workers, the study of corneocytes maturation revealed that skin adverse reactions often corresponded with a variation on the cell surface [106]. Nevertheless very convenient to study the SC, microscopic

techniques assess skin *in-vitro* and mostly take time to give results, when considering the time of the skin failure due to PU.

1.4.2 Mechanical tests

Many tests have been proposed to study skin mechanical properties, including *in-vivo*, i.e. with the skin in a living organism, and *in-vitro*, when a portion of the skin tested is extracted from the organism. The approach is to deform the skin to analyse its behaviour over the deformation. For the *in-vitro* tests, biaxial and uniaxial tensions are the used methods. The most common *in-vivo* tests found in the literature for that are the indentation, torsion, suction, and tension.

The *in-vitro* tests are great for the skin modelling, including its boundary conditions, despite the tricky conservation of the samples – as a saline solution and freezing might alter the mechanical behaviour of the tissue [107]. Furthermore, these tests allow higher loading values, until the failure of the tissue, and, consequentially, more visible stress-strain curves. The most common *in-vitro* tests are the uniaxial and biaxial tensions.

Uniaxial tests implicate the tensile test on a dog-bone shaped sample of skin gripped by clamps [108]. These tests allow the characterisation of the skin anisotropic behaviour and tearing. The biaxial tests have similarities with the uniaxial, as the skin is held by clamps. However, for the biaxial test, the sample shape must be square, and the tension is applied in 2 directions. Figure 1.17 presents the set-up of a biaxial test performed in [18], using the skin of a mouse's belly.

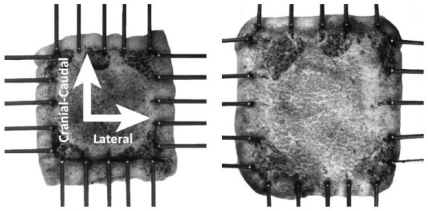

Figure 1.17: Biaxial test set-up of a mouse skin, presented in [18]

For *in-vivo* condition, the **indentation test** involves a normal force applied to the skin and the strain response is measured. The indenter consists of a cylindrical, conic, or spherical tip. The skin model is then studied thanks to its Young's modulus, that is defined as the mechanical

property related to stiffness. The relationship between stress and strain is defined by this modulus [109]. For the indentation test, the relationship of Poisson's ratio, the opposite of the ratio of transverse strain to axial strain, and Young's modulus is presented in equation (1.6), where Y is the Young's modulus, v_p is Poisson's ratio, and subscript i denotes the indenter properties [110]:

$$\frac{1}{Y_r} = \frac{1 - v_p^2}{Y} + \frac{1 - v_{pi}^2}{Y_i} \tag{1.6}$$

An example of set-up for the indentation test, using a conic probe, is presented on Figure 1.18.

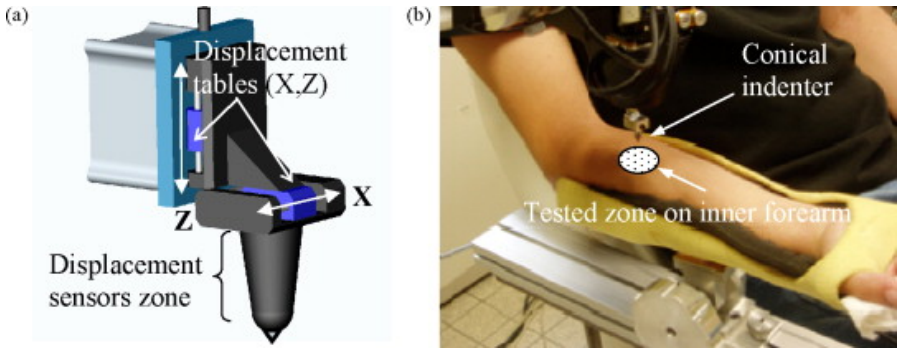

Figure 1.18: Skin tribometer device used in [19]: (a) schematic of the indentor; (b) indentation system and positioning of the subject's arm

In the **torsion test**, a constant rotation or torque is applied to the skin. In [111], a disk, driven by a magnetic field, is used. The skin rotation leads to an opposed moment, as the disk rotates to a balanced position. The torsion angle can be recorded with a light beam. For this test, the Young's modulus is defined according to equation (1.7), with T as the torque, v_p the Poisson's ratio, h the skin thickness, R_d the radius of the disk, and ϕ the rotation angle.

$$Y = \frac{2T(1 + v_p)}{4hR_d^2\phi} \tag{1.7}$$

In [20], a motor was used to perform this test, with a set-up as presented on Figure 1.19:

The **tension test** presented in [21] used two cantilever legs, one fitted with a strain gauge, and a set of acrylic pas with adhesive tape, to guarantee the skin is tensioned with the movement



Figure 1.19: Positioning for the rotating test presented in [20]

of the strain gauge. A suction cup was added to the set-up to yield a pressure over the skin before the gauges' extension, as it can be seen in Figure 1.20. With an initial pressure, the extension of the gauges would register the values on a relaxed skin. In the tensile tests, skin is loaded in parallel with its surface and the tension is recorded for a constant force applied.

Another *in-vivo* test is the **suction test**. It consists of the skin elevation due to a partial vacuum applied by a circular aperture, with the skin deformation measured by optical or ultrasound imaging devices.

The model presented in equation (1.8) was developed in [22], where $P_{ext}(t)$ is the suction pressure applied, $\delta(t)$ is vertical displacement of the skin's surface, h is the thickness of combined dermis and epidermis, r_0 is the aperture radius, indicating the measurement site of the skin, Y is the Young's modulus, σ_0 is the initial stress, and v_p is the Poisson's ratio.

$$P_{ext} = \frac{4\delta(t) \cdot h}{\delta(t)^2 + r_0^2} \cdot \left(\frac{Y}{1 - v_p} \cdot \left(\left[\left(\frac{\delta(t)^2 + r_0^2}{2r_0 \cdot \delta(t)} \right) \cdot \arcsin\left(\frac{2 \cdot r_0 \cdot \delta(t)}{\delta(t)^2 + r_0^2} \right) \right] - 1 \right) + \sigma_0 \right) \tag{1.8}$$

The set-up of the tests lead in [22] is presented in Figure 1.21:

As presented in this subsection, many skin models are available on literature. Besides the

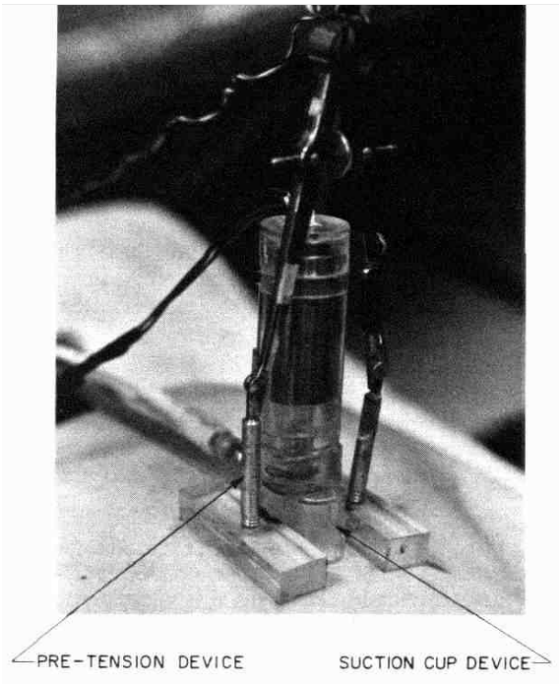

Figure 1.20: Set-up for tensile test *in-vivo* [21]



Figure 1.21: View of the probe used in [22], composed by an ultrasound scanner mode and a suction module

type of stimulation of skin, the skin models differ on the type of analysis made: is the skin considered as a whole tissue, or the study of the layers are also included? Which part of the skin behaviour is evaluated, if we consider the states of skin presented in Figure 1.9? These

considerations depend on what is searched when studying the skin.

In this work, the skin model used is the Kelvin-Voigt Skin Model, viscoelastic type, as it fits well the acoustical nature of the device we have developed, to assess the outmost layer of the skin, the SC.

1.5 Low-Frequency Ultrasound to Characterise Skin Mechanical Impedance

As previously explained, the studies of skin mechanical properties often rely on tests such as stretching [112], sucking [113] or applying torsion [114] to the skin and analysing its deformations. The use of LFU to characterise skin mechanics has been recently explored.

The interest of LFU methodology as a measurement of the skin started in the field of haptics. As this technology is commonly used to produce tactile illusions, it was noticed that the friction has an important role on the sensory system when it comes to textures. In [115], an ultrasound device vibrating at 25 kHz is implemented to produce tactile rendering on a touchscreen. The principle of the tactile devices using piezoelectricity is to simulate textures by modulating the voltage across the PE material according to the contact surface. For the user, when in contact with the touchscreen, the vibrating forces of the device are sensed as a bump or a hole. Various other works can be found on the field of LFU interacting with skin aiming the friction reduction between an ultrasonic vibrating device and skin, such as those presented in [116], [117].

Due to the bidirectional nature of PE materials, it was noticed that these LFU tactile devices could collect data from the interaction between the skin of the finger and the contacting surface. In the literature, the first use of this technique is found in 2007, where a tactile device, namely the T-Pad [118], was proposed, using LFU for friction reduction and the calculation of the friction coefficient during the contact.

In 2016, the T-Pad [118] was used to find the finger's skin damping in a study that highlighted the role of skin damping in ultrasonic friction reduction [119]. The vibration was applied to the finger's skin with a frequency sweeping from 30 to 34 kHz. Another study using 34 kHz to measure skin impedance was presented in [120], where a PE a glass plate was studied in no-

load and in contact conditions. The plate was modelled with a mass-spring-damper system, and the skin of the finger used a Kelvin-Voigt model (Figure 1.11). The parameters of the finger were analysed by comparing the model of the device in the two conditions and verifying how the load affected the resonance frequency of the plate.

A study made in 2017 compared FEM simulated contact with experimental tests with human fingers in order to model friction reduction by intermittent contact [24]. The FEM model included the viscoelastic properties of the skin considering different layers, such as the *stratum corneum*, dermis and subcutaneous tissues. The main outputs were the change in friction for variation on: vibration frequency of the plate, Young's modulus of the SC, intrinsic coefficient of friction, applied normal force and velocity of the finger when moving over the plate.

The results of [24] indicate that the effect of the normal force does not affect the friction of the contact. However, it was also noted that the increase of normal force results in an increase of contact area, rising the lateral force to the point a slip on the contact is initiated, which may influence on the friction. Simulations also considered the SC in dry and moist conditions, by changing to Young's modulus values. The values were found in the literature. In the dry state, the SC is less plasticised by moisture, thus stiffer than in the moist state. Then, the effect of phase shift between vibration and skin is even more proportional with the vibrational amplitude when the skin is dry.

In this context, the study, also focused on haptics, presented in [23] proposed using LFU to determine mechanical parameters of the skin. As the biomechanics of the finger can influence the model of friction forces during tactile surface exploration, this research aimed to measure the acoustical force of the finger's skin. With this strategy, it would be possible to personalise the vibration (and thus the tactile rendering) according to the user's skin mechanics.

The device used for this study operated with an LFU of approximately 25 kHz. It used the voltage difference between the no-load condition and in contact with skin, relating it to the acoustical force from the interaction. Figure 1.22 presents the skin acoustical force behaviour over the increasing vibration amplitude. The force is studied in two components, one related to the viscosity of skin (in red), and the other related to elasticity (in blue). The main output from this study was a correlation found between the acoustical forces of skin and the friction coefficient.

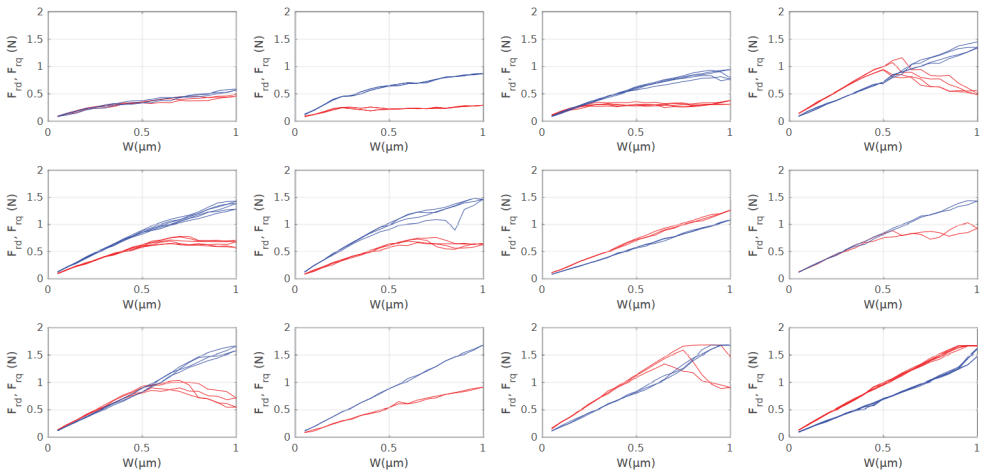

Figure 1.22: Observed values of acoustical force as a function of the vibration amplitude for 12 participants [23]

When the skin is interacting with an LFU device, a factor taken in consideration is the intermittent contact (Figure 1.23). This phenomenon, noted in experimental results [24], is related to contact friction reduction, and occurs due to the fast vibration of the device, which is faster than the behaviour of the skin. The deformation is calculated based on the velocity measurement. On the experiments, three peak-to-peak vibrational amplitudes of 0.420, 1.35 and 2.5 μm were tested (on the figure, the data for the plate is presented in dashed lines), with a normal force between the finger pad and the plate of 0.25 N. In the figure, the green vertical dashed line indicates the concomitance of the peak of the acceleration with the beginning of contact between the finger pad and the plate once the intermittent contact is established. It is noticeable, then, that for lower amplitude vibrations, the intermittent contact phenomenon is not present.

Another example of the acoustical mechanics of finger's skin and its relationship with friction is presented in a recent study from Huloux et al. [25]. In this case, the authors focused on the contact area of the skin and its influence on the interaction with a tactile device. Figure 1.24 presents the contact conditions and images for different amplitudes and normal forces. On the bottom, the bode diagram of the admittance of the plate in contact with skin versus no-load condition is illustrated.

From the figure, one can notice that low normal forces result in lower contact area, as the increase in normal forces brings the two surfaces (skin and plate) together, increasing the num-

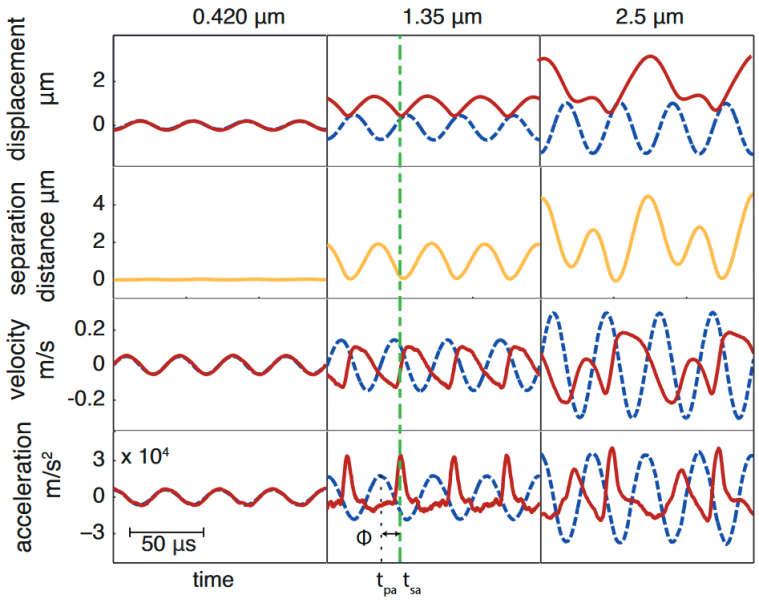

Figure 1.23: Displacement, separation distance, velocity, and acceleration of the skin interaction with an ultrasonic vibrating plate [24]

ber of asperities in contact. The admittance plots depict the vibration attenuation of the plate due to the contact. From the plots, it can also be noticed that, due to the higher levitation forces – induced by high amplitude vibrations, the asperities of skin are pushed away from the plate, reducing the contact area [25].

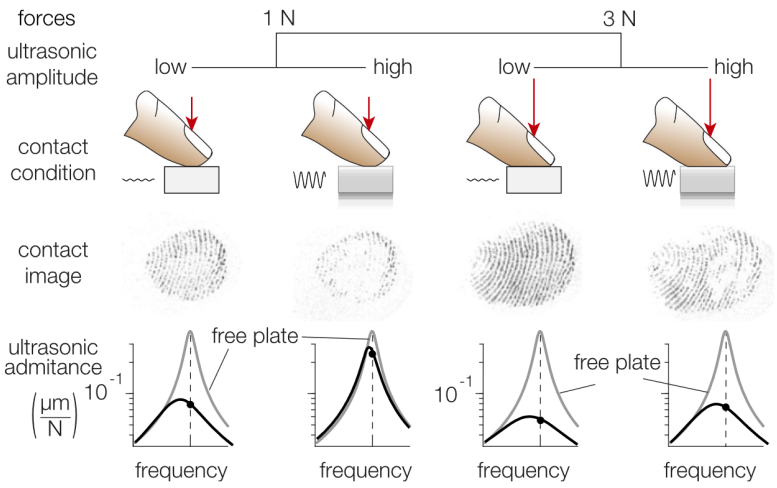

Figure 1.24: Comparison of real contact area optically estimated and of the plate impedance over two normal forces (1 and 3 N) and two ultrasonic vibration amplitudes.[25]

The main outputs of the study from Huloux et al. [25] are: a correlation between the applied force and with the levitation force, found with a curve fitting procedure, also used to the modulus of the skin mechanical impedance expressed as a function of the contact force, which can be seen on Figure 1.25. Here, the mechanical impedance was measured with the plate vibrating at 29194 Hz.

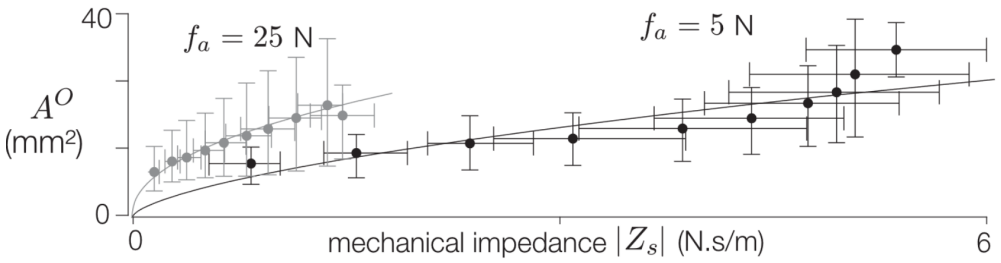

Figure 1.25: Behaviour of the skin mechanical impedance Z_s and optically observed contact area A_O over different normal forces f_a applied.[25]

The studies mentioned above use LFU to understand the mechanics of skin for haptics, thus, they focus exclusively on the skin of the fingertip. Furthermore, they all require a sliding movement of the skin to acquire the dynamics of the friction between skin and the devices.

In our research project, investigations of this technique in other parts of the body (notably non-glabrous) were done. Thus, the considerations of the real contact area are less relevant, as the non-glabrous skin is way less wrinkled than glabrous skin, notably the skin on the fingertips.

1.6 Chapter Conclusions

In this chapter, the CW, especially PU are explained, with the detail of aetiology, consequences for the healthcare system and the patients and the current diagnostic tools. The techniques of ultrasound generation using PE are listed, highlighting the LFU and its applications on CW context.

Then, the mechanical properties of the skin are described, as it is the clue analysed by the device proposed on this project. Mechanical skin models, and the structure of skin layers, focusing on the SC are presented.

Different approaches of skin studies are described in this chapter (summarised in Table 1.4), including non-mechanical and mechanical methodologies.

Table 1.4: Summary of skin tests

	Non-mechanincal	Mechanical	
		Quasi-static	Dynamic
in-vitro	AFM [89]	Uniaxial tensile [107]	
	DMRBE microscopy [106]	Biaxial tensile [18]	
in-vivo	Sebutapes® [99]	Indentation [19]	LFU at 25 kHz [117, 23]
	TEWL [103]	Torsion [20, 111]	
	SCH [103]	Suction [22]	LFU at 34 kHz [119]
	OCT [104, 105]	Tensile [21]	

The study proposed in this project focuses on dynamic mechanical tests using LFU at 60 kHz, further associating them to TEWL and SCH, thus, to the skin integrity. Index linking skin damping and PU was explored by using a device based on a Langevin Transducer.

Among the advantages found in the use of LFU on the early diagnosis of PU, we can cite that it is easy to implement, it reaches the outmost layers (where PU mostly starts), due to the tiny vibration amplitude, and it is a non-invasive and gentle stimulation, which is essential when assessing an already fragile tissue.

Some challenges are found on the development of this device:

1. a vibration imposed and robust to the skin force g_r;
2. a reliable measurement of this force;
3. relating the acoustical mechanical impedance measured to skin characteristics and integrity.

In the next chapter, the architecture of the developed device is presented. The design is detailed, presenting each step taken to build and improve the device and deliver a proper diagnostic tool.

Chapter 2

Low-Frequency Ultrasound Diagnostic Tool Design

Piezoelectric (PE) devices can work either as actuators or sensors, i.e. the electromechanical effect is reversible, and the use depends on what is the input and the output of the system. When used as actuators, the goal is to impose an effect on the environment (a contact surface or a fluid, for instance), using electric signals to yield vibration. In this case, the reaction effect from the environment on the vibration generated exists but is not always relevant for the application. However, when used as a sensor, the PE device uses the reaction force from the environment to produce an electrical signal, which reflects the effects of the interaction.

This project's goal is the use of a PE based LFU device as a sensor and actuator simultaneously. The device chosen for the matter is the LT, commonly used for actuator applications in other fields, such as industrial cleaners [121], underwater sonar [122], cell blasters [123] or droplet generation [124].

Here, the goal of the LT application is to analyse skin integrity through the reaction force to ultrasonic vibration. It is expected that skin mechanical properties change due to the vicious cycle of cell and tissue damage in PU, involving tissue distortion, deformation (strain and stress), inflammatory process and oedema [2]. Knowing that LFU can be used as a sensor to measure the reaction acoustical force of the skin [23], an approach to link the skin mechanics with PU

using the LT is envisaged.

The use of LFU in sensing applications requires a system architecture that is able to generate and control the vibration and obtain data from the interaction between the skin and the device. In this chapter, details involving the construction of the LFU diagnostic tool, named Skin Acoustical Mechanical Impedance Sensor (SAMIS), are presented.

2.1 Langevin transducer, operating principle and modelling

Ultrasound vibration is mainly generated by 3 different sources: liquid-driven source (effectively liquid whistles), magneto strictive source (size reduction of metals under a magnetic field) and using the reverse piezoelectric effect [125], the latter being the most common method.

The PE technology was firstly used for ultrasound submarine detection, then it was expanded for microphones, pick-ups, accelerometers, phonographs, signal filters, frequency stabilizers, bender element actuators and flaw detection in solids. Then, in the end of 1930s, its use in healthcare started [126]. Nowadays, ultrasound transducers are widely used for treatment, such as those for cancer treatment and neurosurgery, as well as for non-invasive diagnosis by imaging.

Created in 1922 by Paul Langevin, the Langevin Transducer was first designed as a submarine sonar, to detect objects under the water by ultrasound reflexion [56]. This device is also commonly used for micro-droplet generation for liquid atomization [127], as smooth impact drive mechanism for camera lens modules [128], cleaning and washing of surfaces [121] and friction reduction (for haptics application) [129].

The LT, in most cases, consists of two PE ceramic discs, with opposite longitudinal polarization, sandwiched with metal bodies, and transducer parts are entirely mechanically assembled in series, as presented in Figure 2.1.

To optimise the electromechanical conversion, the ceramics are longitudinally positioned with opposite polarisation, as the longitudinal deformations follow the direction of the polarisation. Due to this layout, it is possible for the metal bodies, often in aluminium, to enhance forward acoustic energy transmission and to attain lower acoustic impedance in comparison with that of PE layers [130].

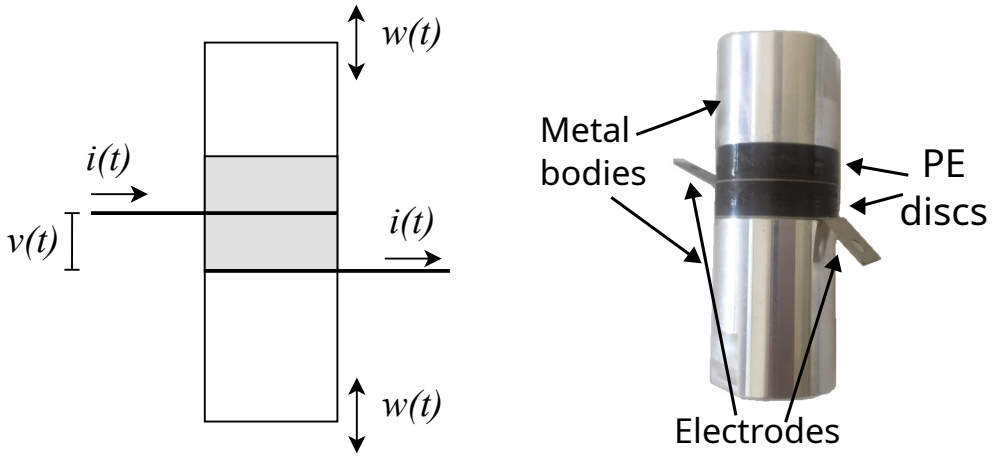

Figure 2.1: Langevin transducer's parts

The operating principle of this actuator is based on the exploitation of the inverse piezoelectric effect. Therefore, the two piezoelectric ceramics deform in phase, contracting in a longitudinal mode whenever an electric field is applied between the electrodes. This longitudinal effect can therefore be used in turn for electromechanical energy conversion. The vibrations created in the ceramics are transmitted to the two metal bodies.

Considering all properties of the piezoelectric ceramics, analogies between electrical and mechanical systems are used, to represent this device in terms of an electrical system. Different models have been proposed for this representation, such as Mason model [26], Krimholtz-Leedom-Matthaei (KLM) [131], and Butterworth-Van Dyke (BVD) model [132].

The Mason model, presented in Figure 2.2, consists of an equivalent circuit model, where the electrical and mechanical properties are coupled only through an ideal transformer of transformation factor N.

In the electrical representations of a PE material, the mechanical part of the system consists of D, K and M, namely the motional resistance, motional capacitance and motional inductance. Each of these components represent the elastic loss, elastic compliance, and the mass inertia, respectively. The capacitance C_0 is the intrinsic-damped capacitance of the transducer, before any mechanical deformation, and c_k is the coefficient of coupling. In Figure 2.2, the external reaction force $g_r(t)$, previously mentioned in the Kelvin Voigt model as the skin force, is also presented.

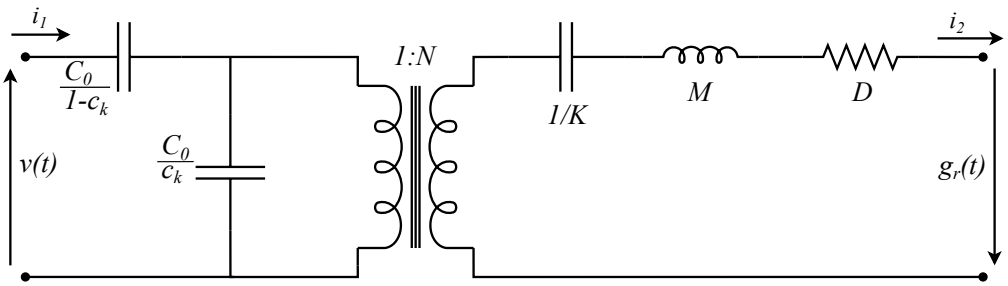

Figure 2.2: Mason's electromechanical representation of a piezoelectric crystal, employing an ideal transformer. Adapted from [26]

The approach presented in [27] used a simplified Mason's electrical equivalent to identify the parameters M, D and K of a PE device they developed. For that, they considered series (ω_s) and parallel (ω_p) resonance pulsations, defined by:

$$\omega_s = \sqrt{\frac{K}{M}} \tag{2.1}$$

$$\omega_p = \sqrt{\frac{K + C_0}{(M + KC_0)}} \tag{2.2}$$

The admittance of the motional branch M, D and K, in the Nyquist plane, is a circle with radius $1/2D$ and centre in the point ($1/2D$, 0), as shown in Figure 2.3. This method is also explored for an LT in [133].

Although the Mason's model is very interesting, in this thesis, we used a BVD model to represent the electrical equivalent model of the LT, depicted in Figure 2.4, and identified the parameters of the system using a mechanical equivalent, as it is presented in the section 2.3. A simplified schematic is offered, where the force is the analogue of voltage, the mechanical displacement of the electrical charge, and the velocity of the electrical current. In the Figure 2.4, $v(t)$ is the supply voltage, $i(t)$ is the supply current and $i_m(t)$ is the motional current.

The Mason's model is the most well-known in PE transducers literature, nonetheless, the BVD equivalent is simpler, its components are constant, while in Mason's they are modelled as transcendental functions, such as in conventional electronic systems. Nonetheless, the BVD can describe the impedance curve only in narrowband frequencies near the resonance of the transducer [134].

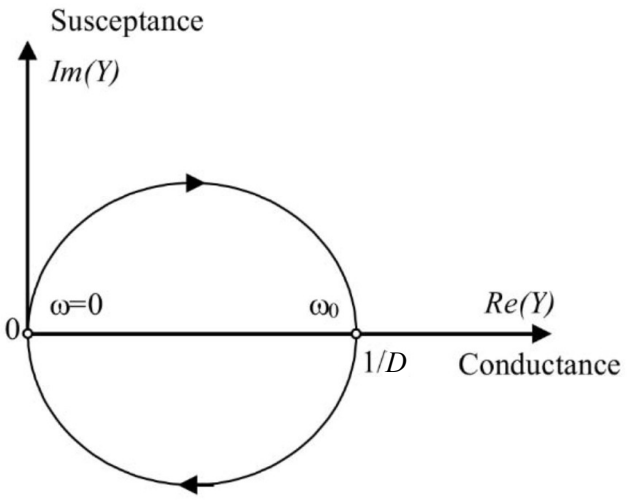

Figure 2.3: Dynamic admittance in the Nyquist plane [27]

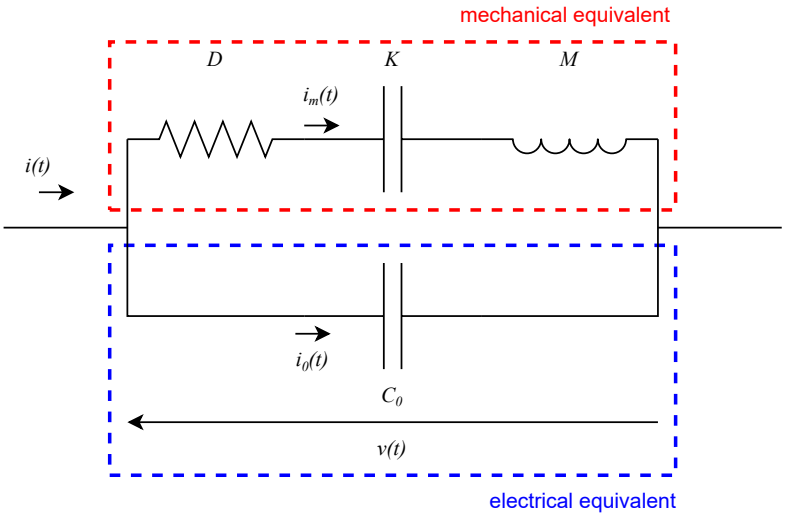

Figure 2.4: BVD schematic of a Langevin Transducer's electromechanical components

The equation describing this system, considering the velocity as an electrical current and a no-load operation, is then as in (2.3):

$$M\ddot{w} + D\dot{w} + Kw = g_e \tag{2.3}$$

Where w is the amplitude of vibration, and $g_e = Nv(t)$ is the electrical force that drives the LT, with the transformation factor N, an intrinsic coefficient of the PE ceramics that indicates the

electromechanical conversion of the transducer.

From the equation presented above, it is obvious that the vibration amplitude highly depends on the voltage across the electrodes. However, it also depends on the working frequency.

The frequency where the LT vibrates with the highest amplitude, for the same input voltage, is known as the resonance frequency (f_0). This frequency is established by the length of the transducer [135]. When vibrating at the resonance frequency, the electromechanical conversion of the device is enhanced, and the relation between the resonance frequency and the coefficients from equation (2.3) is $f_0 = \frac{1}{2\pi}\sqrt{\frac{K}{M}}$. The LT's f_0, however, due to non-linearities of PE materials under different combinations of electric and mechanical fields, may vary depending on the field applied [136].

These non-linearities appear under strong or weak electric fields in different manners: high electric fields typically relate to hysteresis behaviour, while lower fields can lead to heat generation, mechanical break down or instability when operating in the resonant mode, caused by the jump phenomena [137].

To find the resonance frequency and characterise non-linearities on the LT, one can execute a frequency sweep with the same input voltage. It is also possible to analyse the non-linearity of f_0 under different fields, running several sweeps. In [28], for instance, tests present an LT vibrating between 23 and 28 kHz, under different excitation voltages and the velocity amplitude is measured using a spectrum analyser.

From the curves depicted in Figure 2.5, a shift on the resonance frequency is clear, with an asymmetric peak phenomenon. As the excitation field increases, the jump phenomenon is observed, as a result of the device preventing an unstable vibration through amplitude and phase jumps. These resonance shifts are associated to a softening behaviour of the PE [28].

Tests with the device implemented on this project are presented in section 2.3. On the next section, details on how the architecture of the device was constructed are presented. This system is essential to operate the actuator and further identify and control it.

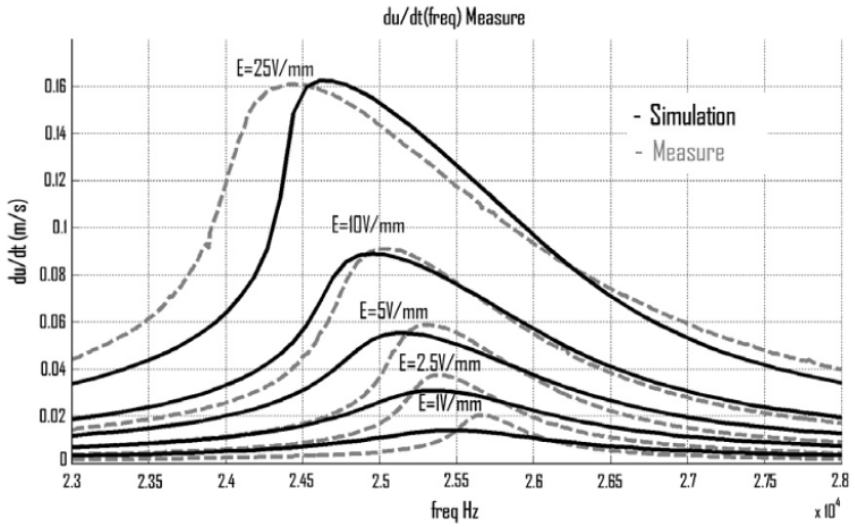

Figure 2.5: Frequency sweep under different electric fields fro an LT [28]

2.2 Architecture of the Device

The global architecture, depicted in Figure 2.6, consists of three subsystems: the ultrasound generation, a normal force control and sensors. The communication between this system and the user depends on a host PC, using serial ports and MATLAB as software.

Between the computer and the ultrasound generation, there is a microcontroller, consisting of a Digital Signal Processor (DSP) chip, STM32F4 from STMicroelectronics. The input voltage for the power supply is controlled by this chip, which is also used to acquire the measured data from the sensors' subsystem, attached to the LT.

The communication between the normal force sensor and the computer is also through serial ports and MATLAB, but with a data acquisition adapter, from Meßsysteme®. In the next subsections, these subsystems are detailed.

2.2.1 Low-frequency ultrasound generation

The circuit designed for the LFU generation is composed of a power supply and a voltage amplifier. The former consists of an AC/DC converter, connected to the network, with an AC input of 220 V and DC output of 43 V. The latter is an amplifier LM675 from Texas Instruments, with 0.4158 of gain, maximum output of 43 V peak to peak (constrained by the power supply)

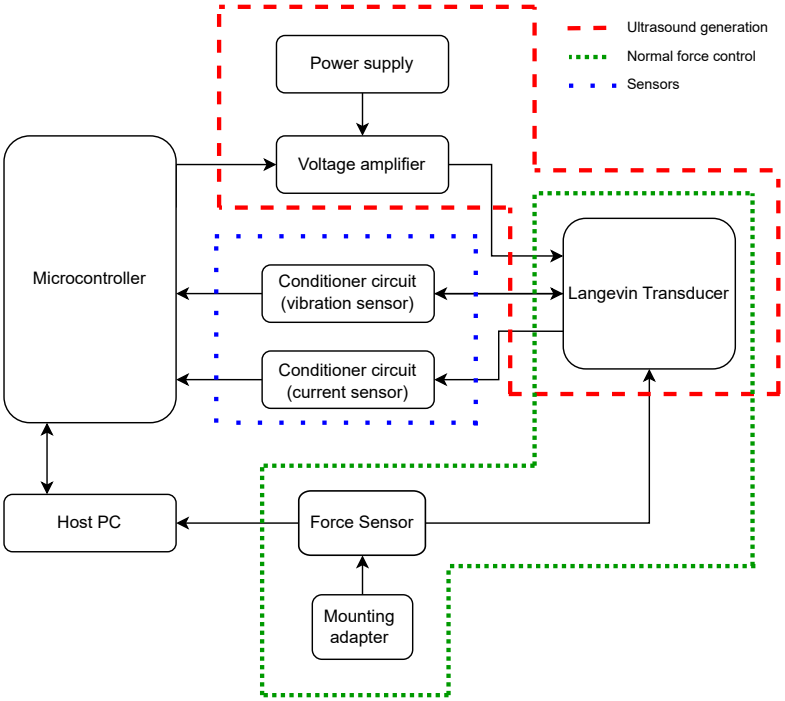

Figure 2.6: Global architecture of SAMIS

and 3 A (constrained by the factory). The current and voltage thresholds are fixed for the security of the user and the patient as well as to protect the LT electrodes and ceramics, which have a maximum tolerance of 25 W. The amplifier has wide power bandwidth of 70 kHz and a gain bandwidth of 5.5 MHz [138].

The DSP provides the control and measurement of the voltage supply to the LT by a DAC connection with a resolution of 12 bits. The voltage is applied to the LT with a 22Ω stabilizer resistance in series with a current sensor consisting of a transformer (4:23 windings) and another 22Ω resistance to create a conversion for the current sensor gain ($G_c = \frac{4}{23}22 \cong 4V/A$). This circuit schematic and its electric representation are presented in Figure 2.7. In the schematic, the LT is considered, as in the BDV model, as a capacitor, of C_0=22μF.

2.2.2 Conditioners and Sensors

The sensors' subsystem is composed of two sensors: the 4:23 transformer shown in Figure 2.7, that operates as the current sensor, and the deformation sensor, consisting of a PE piece glued

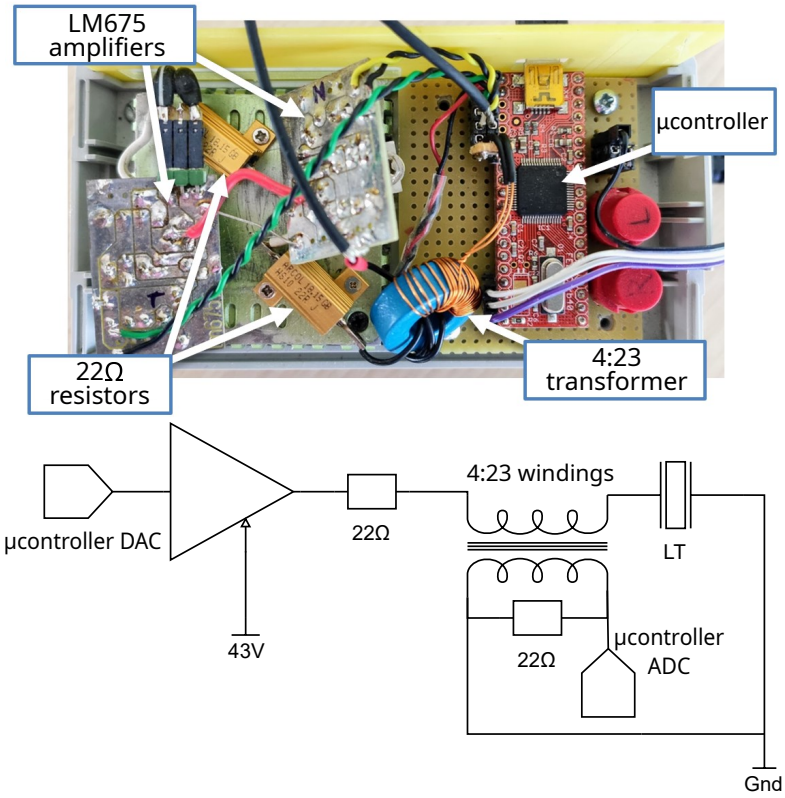

Figure 2.7: Circuit of LFU input voltage supply

on the LT.

The piece of PE ceramic attached to the LT is connected to the DSP. The deformation sensor is ideally attached to the node of the device, as depicted in Figure 2.8. In vibrating devices, the node is where the displacement is zero. The node of an LT is in the central part of the ceramic, between the two PE discs, because it is a longitudinal mode that is exploited. In the sites close to the node, the deformation in the structure is maximum, and the displacement is minimum, while in the edges of the metal bodies there is no deformation and a maximal displacement. Due to this property, vibration amplitude produced by the LT can be measured.

A 22 nF capacitor is connected in parallel to the strain sensor, to adapt its gain as depicted in the Figure 2.8.

To identify the gain of the vibration sensor and convert the displacement in metres, experimental laser interferometry tests were performed to track the vibration, when a sinusoidal

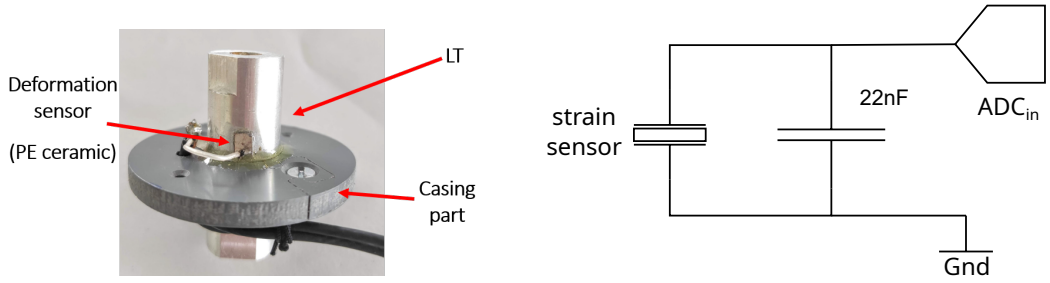

Figure 2.8: LT with a close look in the PE sensor and conditioner circuit for the strain sensor

voltage (reasonably at constant amplitude and frequency) was applied to the LT, with the set-up presented in Figure 2.9.

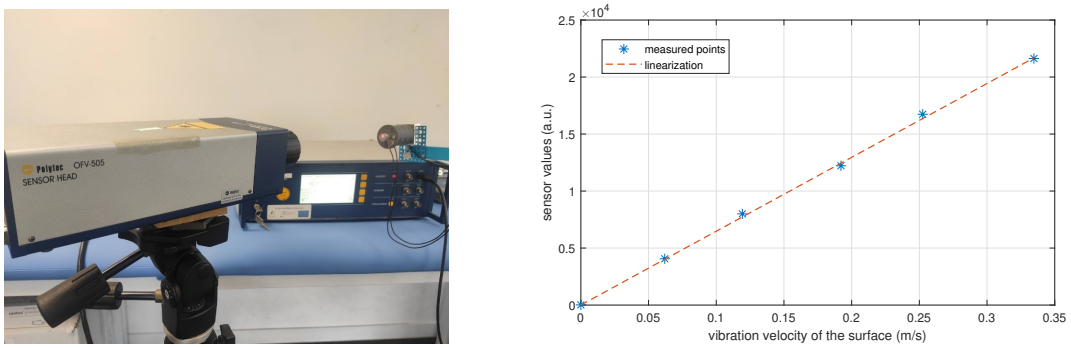

Figure 2.9: Measurement of the displacement with a laser interferometer of the vibrating surface of an LT

The laser outputs a voltage that is proportional to the vibration velocity of the device. This output is measured with an oscilloscope that also measures the input in the LT. The sensitivity of the laser interferometer is 125 mm/s/V, taking in consideration the peak-to-peak voltages of the laser interferometer and the LT from the raw data measurement provided by the DSP ADC in. The mean of 40 samples for each voltage input (v=[0, 2.08, 4.16, 6.24, 8.32, 10.40, 12.47], shown in Figure 2.9) were used to find the deformation sensor sensibility, G_s, that is calculated using the voltage and sensitivity of the laser. For the experiments with the LT used, this gain was calculated $G_s = 0.0648$ s/m. This output is measured and compared with measurements of LT input voltage to set the gain of the device.

2.2.3 Normal force control

To control the experimental conditions during the tests, we decided to measure the normal force at which the LT is indented on the skin. Then, a normal force control was included on the set-up, relying on two parts: the mounting adapter and the normal force sensor.

Mounting Adapter

Due to the way the LT vibrates and how it irradiates the waves, the best way to hold it is at the node. A common LT has only one node, between the two piezoelectric discs. Both extremities of the device must be free to vibrate, so the holding structure of the device must have a free space for these displacements.

A three-part casing was developed taking these specifications into account using FreeCAD, a free software for 3D designing, as presented in Figure 2.10.

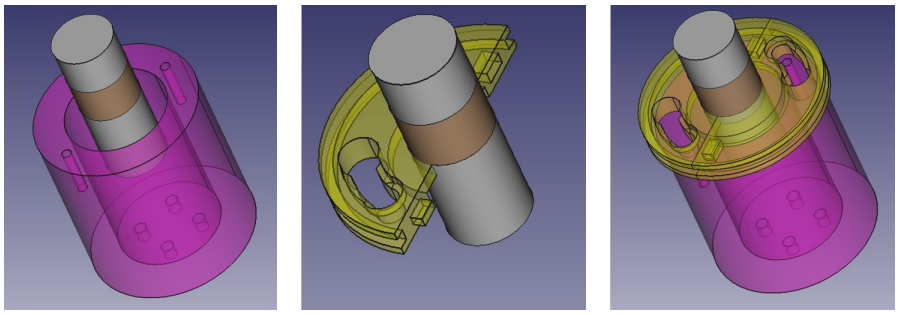

Figure 2.10: Casing parts: bottom, always attached to normal force sensor, half of the central part, always attached to the LT, and assembled case

The bottom part (in pink, Figure 2.10) is designed to fit different LT probes to vibrate freely on both extremities, since other LT with different frequencies were studied (detailed in chapter 3). It was also necessary to put holes for the screws to assemble the other 2 parts of the casing. In the bottom of this piece, 4 holes were made to attach the casing to the normal force sensor.

The holding structure of the case, placed at the vibration node, was designed with 2 mirrored parts that are assembled together. The 2-parts holder is glued to the LT to prevent any sliding of the device.

Taking the 60 kHz LT, we ran a frequency sweep to evaluate the shifting of the resonance frequency of the device before and after the casing, shown in Figure 2.11. The input voltage

for this experiment was $v(t)$ =1 V peak to peak. From the curves, it seems that the resonance frequency f_0 shifted to the right (f_0 was 60892 Hz before, and 61102 Hz after, at the time of the tests), with the addition of the casing. The parameters' identification and control of the device were designed for the cased characteristics. The quality factor, a parameter that characterises the energy consumed by the PE body to overcome internal friction during the resonance, is also slightly affected, as it can be noted by the reduction of the vibration behaviour, once the device is cased.

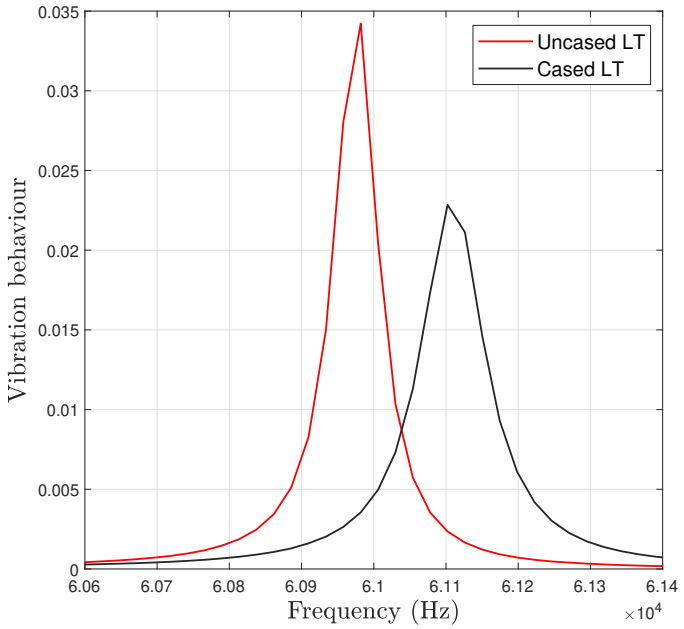

Figure 2.11: Results of a frequency sweep before and after casing the LT

To hold the device and set the contact normal force, the case was installed on a camera tripod with a holder arm to position the case. In Figure 2.12, (A) indicates the placement of the device in the extremity of the arm. The indentation is made by setting up and down the rod (C) of the tripod. The movement of the rod causes horizontal tilting in the holder arm, so the length of the arm is 530 mm, to reduce the tangential angle of the contact, since the longer the arm is, the smaller the tilt is. In (B), a spring with a tiny spring constant was added to keep the indentation force constant. The height of the tripod is set according to the bed and can be adjusted in (D).

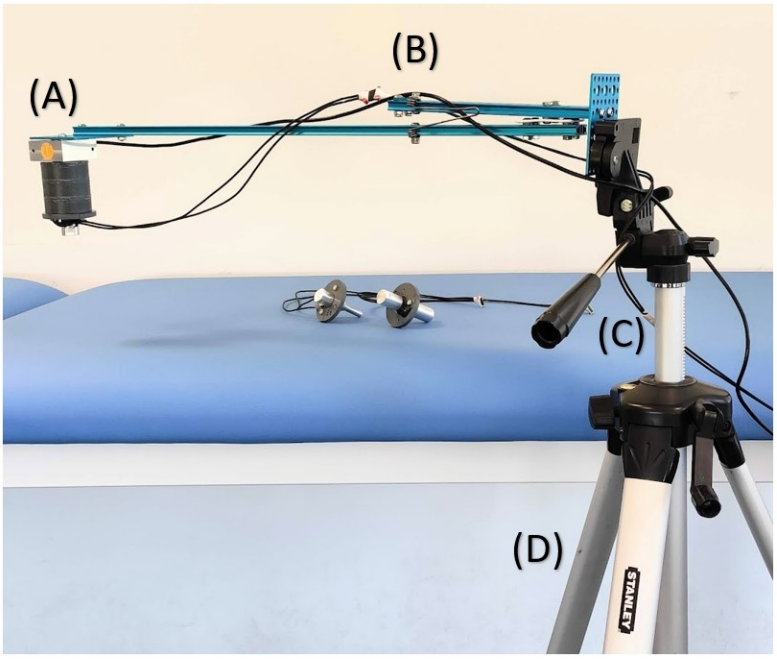

Figure 2.12: Mounting structure: (A) LT and force sensor placement (B) holding arm, with a spring (C) tripod rod – to control the indentation force (D) tripod

Normal force sensor

The normal force sensor used to measure the indentation is a 3-axis sensor K3D40, from Meßsysteme® (Figure 2.13). It measures the indentation force applied from the device over a surface. An amplifier GSV-4USB SubD37 is used as an interface between the sensor and the PC, with MATLAB software.

The sensor is attached between the LT case and the holding structure. A 3-axis (x, y, z) force sensor was chosen so that it will be possible to make measurements with the device in any position. The change of position will affect the force values for a no-load condition; on the other hand, it is possible to measure the force in all three axes and reset the no-load values by performing the calibration.

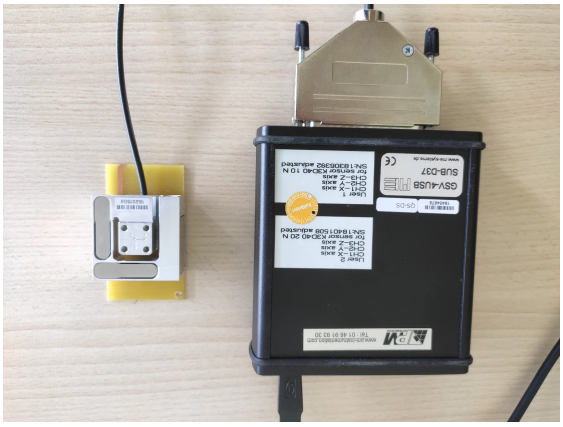

Figure 2.13: GSV adapter and 3-axis force sensor

2.3 Identification and Control of the System

2.3.1 Electromechanical Model of the Langevin Transducer

Section 2.1 has presented the electrical equivalent scheme of this transducer's behaviour. Here, the mechanical equivalent is presented, as it is used to assess the mechanical interaction with contacted surfaces. The model considers the mechanics of the device as an equivalent mass-spring-damper, with vibration $w(t)$. In this model, depicted in Figure 2.14, K, D and M are the elastic, damping and mass coefficients and $g_r(t)$ represents the contact force, a charge applied to the device. When it operates in a no-load condition, $g_r(t) = 0$.

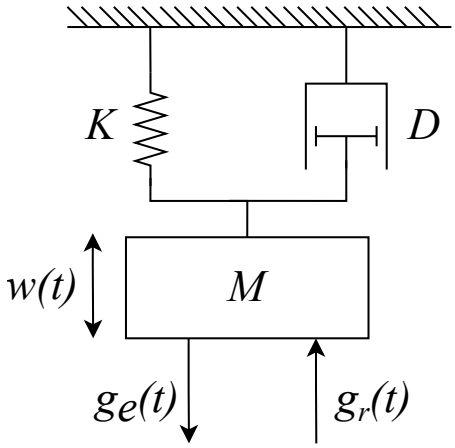

Figure 2.14: Equivalent mass-spring-damper model of the Langevin Transducer

The equation ruling the mechanical model is similar as (2.3), but can be represented in (2.4), considering $v(t)$ as the input voltage and including the external force $g_r(t)$.

$$M\ddot{w} + D\dot{w} + Kw = Nv - g_r \tag{2.4}$$

The displacement $w(t)$ characterises the instantaneous value of the vibration. The device described in this document has a tiny displacement and its frequency is high. In this context, the rotating reference frame representation is used, to facilitate the representation and, further, the control of this vibration [139].

In this representation, the LFU sinusoidal vibrations are considered as constant variables when in steady state. For that, they are represented in a frame that turns in the same frequency as the system. Fig. 2.15 illustrates the vibration $W(t)$ in the (d, q) frame, defined as (2.5), with $\omega = 2\pi f$:

$$w(t) = \underline{W(t)}e^{j\omega t} = (W_d + jW_q)e^{j\omega t} \tag{2.5}$$

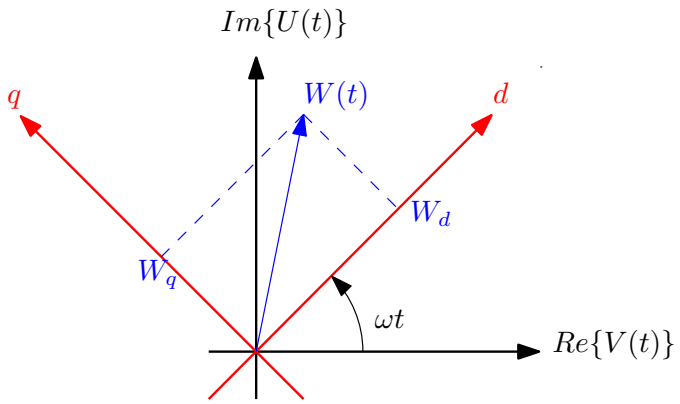

Figure 2.15: Vibration displacement $W(t)$ represented in the rotating reference frame, rotating in a frequency ω

The other sinusoidal variables of the system are also represented in the (d, q) frame. By convention, d-axis is aligned with $e^{j\omega t}$. Moreover, we introduce $u(t)$, the vibration velocity, as

$u(t) = \dot{w}(t)$. Then, velocity, voltage, and force can be notated as in (2.6):

$$\begin{aligned} u(t) &= \underline{U} e^{j\omega t} = (U_d + jU_q)e^{j\omega t} \\ v(t) &= \underline{V} e^{j\omega t} = (V_d + jV_q)e^{j\omega t} \\ g_r(t) &= \underline{G_r} e^{j\omega t} = (G_{rd} + jG_{rq})e^{j\omega t} \end{aligned} \tag{2.6}$$

The velocity in this representation is denoted in (2.7):

$$\dot{u}(t) = \left((\dot{W}_d + j\dot{W}_q) + j\omega(W_d + jW_q)\right) e^{j\omega t} \tag{2.7}$$

Considering the vibration acceleration and amplitude in terms of the vibration velocity:

$$\begin{aligned} \underline{\ddot{w}} &= j\omega(U_d + jU_q)e^{j\omega t} \\ \underline{w} &= \frac{U_d + jU_q}{j\omega} e^{j\omega t} \end{aligned} \tag{2.8}$$

Then, the equation (2.4) can be expressed in space vector [139, 140], and in terms of vibration velocity, by the 2 equations in (2.9):

$$\begin{aligned} \left(M + \frac{K}{\omega^2}\right)\dot{U}_d + DU_d + \left(\frac{K}{\omega} - M\omega\right)U_q &= NV_d - G_{rd} \\ \left(M + \frac{K}{\omega^2}\right)\dot{U}_q + DU_q - \left(\frac{K}{\omega} - M\omega\right)U_d &= NV_q - G_{rq} \end{aligned} \tag{2.9}$$

Taking a small variation of frequency, around the resonance frequency $\delta\omega = \omega - \sqrt{K/M}$, the equations in (2.10) are the representation in the rotating reference frame of equation (2.4) taking equation (2.9) in consideration.

$$\begin{aligned} 2M\dot{U}_d + DU_d - 2M\delta\omega U_q &= G_{ed} - G_{rd} \\ 2M\dot{U}_q + DU_q + 2M\delta\omega U_d &= G_{eq} - G_{rq} \end{aligned} \tag{2.10}$$

Once these considerations on the variables of the system were taken, the identification of the system's parameters were carried out, and the control was designed.

2.3.2 Identification of the parameters

The first parameter to be identified was the resonance frequency, $f_0 = \omega_0/2\pi$, through the measurement of the vibration on a constant input voltage and varying the operation frequency. The tests were taken in three LT, as it is presented in 3.2.1. However, in this section only the identification of the main device (nominally 60 kHz) is detailed.

The test is taken by sweeping the frequency around the nominal value of f_0, for several vibrating amplitudes. For this main device, the range of the sweep was from 60900 Hz to 61500 Hz (Figure 2.16). The tests were made for a variety of voltage inputs V_d and $V_q = 0$, investigating the non-linearity of the probe used, with results noted in Table 2.1. The data was obtained at constant and operating temperature to skip its influence on resonance frequency.

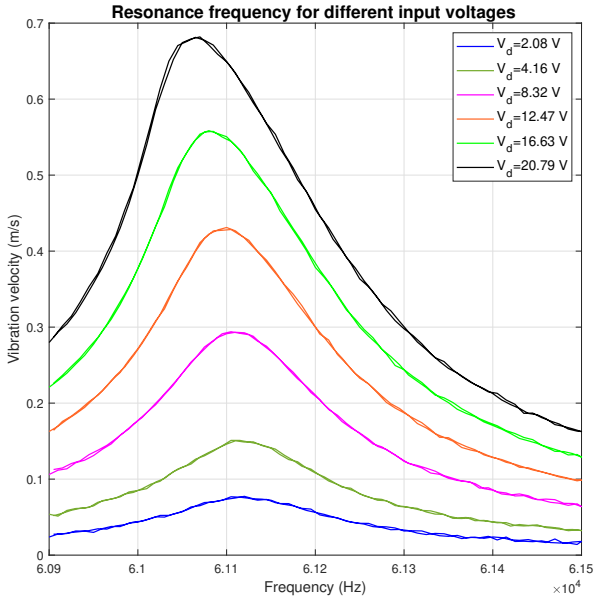

Figure 2.16: Frequency sweep for different amplitudes

Table 2.1: Resonance frequency for a variation on the input voltage

V_d (V)	2.0789	4.1578	8.3156	12.4734	16.6312	20.7889
f_0 (Hz)	61120	61115	61105	61100	61080	61065

As expected from literature (for instance, the results presented in Figure 2.5) and confirmed by experiments, f_0 shifts a little according to the input voltage. To identify the parameters of the device, we used $V_d = 12.47$ and $V_q = 0$ V.

The identification of the parameters of the LT is carried out in steady state, where $\dot{U}_d = \dot{U}_q = 0$, and at no-load conditions, i.e. $G_{rd} = G_{rq} = 0$. Furthermore, voltage was aligned, once again, with the axis d, leading to $V_q = 0$. The equations 2.9 gives then:

$$\begin{aligned} \frac{K - M\omega^2}{\omega} U_q + DU_d &= NV_d \\ -\frac{K - M\omega^2}{\omega} U_d + DU_q &= 0 \end{aligned} \tag{2.11}$$

From equation 2.11 we can substitute the term $\frac{K-M\omega^2}{\omega}$. Then, in the equation 2.12, the parameters M, K and ω disappear, excluding the non-linear behaviour of the model. Then, we ran a frequency sweep at $V_d = 12.47$ V, leading to a variation on U_d and U_q that describes a circle, following the equation (2.12).

$$U_q^2 + \left(U_d - \frac{NV_d}{2D}\right)^2 = \left(\frac{NV_d}{2D}\right)^2 \tag{2.12}$$

From the equation, the centre of the circle is located at $\left(\frac{NV_d}{2D}, 0\right)$. When U_d is maximum and $U_q = 0$, the working frequency is at the resonance.

On the electrical side of the vibration, the current, in the rotating reference frame, $i(t) = \underline{I}e^{j\omega t} = (I_d + jI_q)e^{j\omega t}$, derives from the capacitive behaviour of the LT and the direct PE effect by $i(t) = C_0\dot{v} + Nu(t)$. Then, it can be described by 2.13:

$$\begin{aligned} I_d &= NU_d + C_0\dot{V}_d - C_0\omega V_q \\ I_q &= NU_q + C_0\dot{V}_q + C_0\omega V_d \end{aligned} \tag{2.13}$$

Introducing (2.13) into (2.12) another equation of a circle is generated, in the current domain:

$$(I_q - C_0\omega V_d)^2 + \left(I_d - \frac{N^2V_d}{2D}\right)^2 = \left(\frac{N^2V_d}{2D}\right)^2 \tag{2.14}$$

Therefore, considering that the vibrating frequency f is at the vicinity of f_0, the vector $\underline{I}$

follows a circle which diameter is now N^2V_d/D. Therefore, the electromechanical parameter N can be identified by dividing the diameters of the 2 circles.

Figure 2.17 presents the circles described by the velocity and by the current, the former rotated in a way that the centre is located in $\left(\frac{NV}{2D}, 0\right)$. In this configuration, the resonance frequency operation is found in the point where U_d is maximum and $U_q = 0$.

Approximation circles were drawn for the velocity and current circles (dashed pink curve in the figure), to find their diameters. For the velocity, the diameter was 0.4359 m/s and for the current, 0.24 A. Hence, the conversion factor found was N=0.55 N/V.

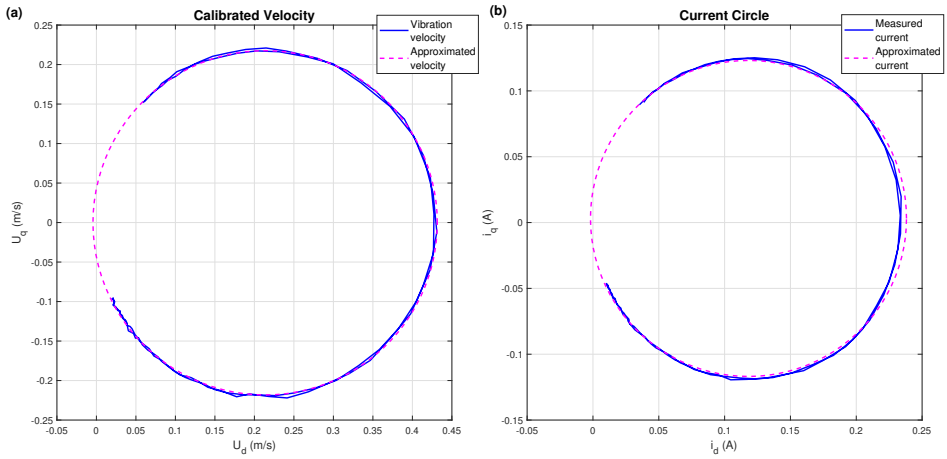

Figure 2.17: Behaviour of the (a) velocity and (b) current, in the rotating reference frame for frequency variation, with a constant voltage V_d=12.47 V and V_q=0

With the value of N and the data from Figure 2.17, the damping coefficient was found $D = 15.74$ Ns/m. To calculate M, we consider the bandwidth of the LT. At the pulsations ω_{p1} and ω_{p2}, indicated in Figure 2.18, the vibration velocities are $U_d = U_q = \frac{NV_d}{2D}$ and $U_d = -U_q = \frac{NV_d}{2D}$ respectively. Developing the first equation in (2.11) for the points where $\omega = \omega_{p1}$:

$$\frac{K - M\omega_{p1}^2}{\omega_{p1}} \left(\frac{NV_d}{2D}\right) + D\left(\frac{NV_d}{2D}\right) = NV_d \tag{2.15}$$

$$K - M\omega_{p1}^2 = D\omega_{p1} \tag{2.16}$$

and for $\omega = \omega_{p2}$ and $U_q = -\frac{NV_d}{2D}$:

$$\frac{K - M\omega_{p2}^2}{\omega_{p2}} \left(-\frac{NV_d}{2D}\right) + D\left(\frac{NV_d}{2D}\right) = NV_d \tag{2.17}$$

$$-K + M\omega_{p2}^2 = D\omega_{p2} \tag{2.18}$$

Adding equations (2.16) and (2.18)

$$M(\omega_{p2}^2 - \omega_{p1}^2) = D(\omega_{p1} + \omega_{p2}) \tag{2.19}$$

$$M(\omega_{p2} - \omega_{p1})(\omega_{p1} + \omega_{p2}) = D(\omega_{p1} + \omega_{p2}) \tag{2.20}$$

Then,

$$M = \frac{D}{\omega_{p2} - \omega_{p1}} \tag{2.21}$$

To assure this value is independent of the vibration amplitude demanded, the same calculation was made for different input voltages, presented in Figure 2.18. For all 6 circles, the value of M is estimated as M=0.0147 kg. When vibrating at the resonance frequency,

$$\omega_0 = \sqrt{\frac{M}{K}} \tag{2.22}$$

Then, K is estimated as K=2.1689 nN/m.

Having the model's parameters defined, we can propose a closed loop control of the vibration velocity.

2.3.3 Controller Design

The optimal operation of the LT depends on the reliability of its vibration and frequency. As aforementioned, the LT suffers a reduction of its resonance frequency if the temperature or excitation field of operation rise, and shifts over a perturbation such as the application of a load

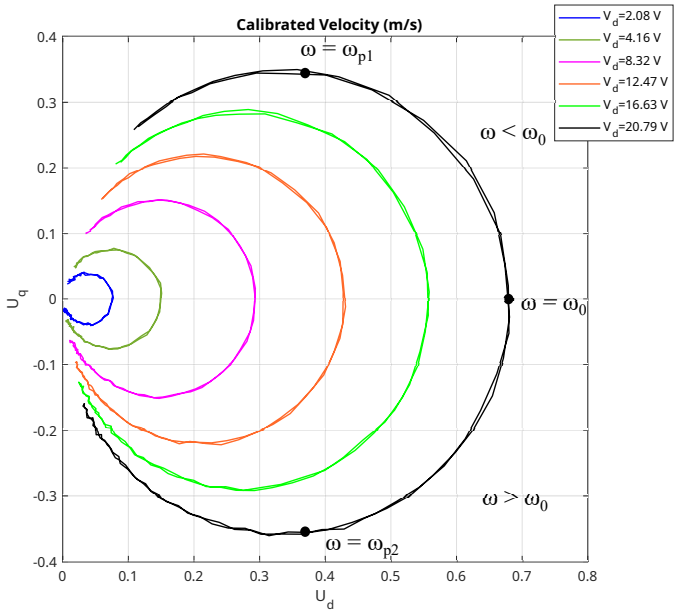

Figure 2.18: Behaviour of the velocity, in the rotating reference frame for frequency variation, for a variety of voltage inputs V_d and $V_q = 0$

[135]. Hence, it is fundamental to control the vibration of the device, even when it is operating out of the resonance frequency (yet in the vicinity of f_0), or when it is in contact with a surface.

The Energetic Macroscopic Representation (EMR) is a causal representation of systems, of the SAMIS can be found in Figure 2.19. With the EMR, so, it is possible to describe the relations between causes and effects of a system, allowing the analysis of energetic flow in the system [139]. In the schematic on the figure, ES is the electric power source of the LT and MS is the mechanical source, connected to the system. The piezoelectric effect through the parameter N is represented by the orange circles, the coupling between axes d and q through $\delta\omega$ are represented by the overlapped squares and the kinetic energy stored in the vibrating mass of LT, as an accumulation element, is represented by the crossed rectangle.

For the design of the controller, the analysis is made in a no-load condition, thus, it is simpler to track the resonance frequency. The methodology lies on the verification of the vibration point where $U_q = 0$, as noted in the Figure 2.17, presented in the previous section.

The vector controller method is the best suit for the system in question, since it vibrates in a high frequency. Indeed, once represented in the (d, q) frame, in steady-state, U_d and U_q are

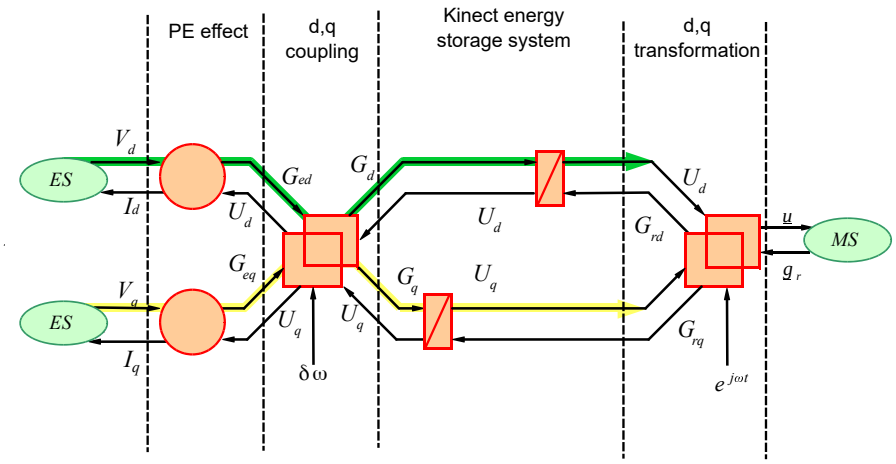

Figure 2.19: Energetic macroscopic representation of a Langevin transducer

constant and easier to control than a vibrating variable.

The causal schematic of the system shown in Figure 2.19, with the addition of the controller, is depicted in Figure 2.20.

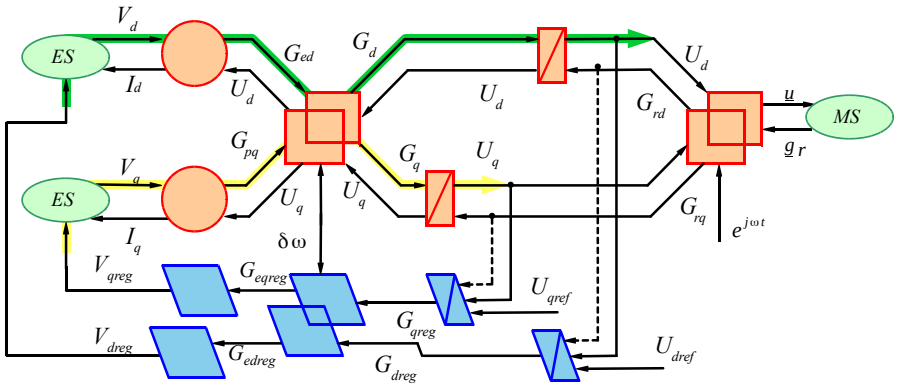

Figure 2.20: EMR of the system (orange) with the controller structure (blue) and the tuning paths (in green and yellow)

Assuming the system works no-load and at the resonance frequency, i.e. G_d, G_q and $\delta\omega = 0$, the transfer function of the equations in (2.10) become:

$$\begin{aligned}(2Ms + D)U_d &= NV_d \\ (2Ms + D)U_q &= NV_q\end{aligned} \tag{2.23}$$

In open loop, a step response of the velocity was demanded, after the resonance was

tracked, when the device works at this point, and the results are depicted in Figure 2.21. The open loop step shows a first order response, validating the model proposed in the equations (2.23).

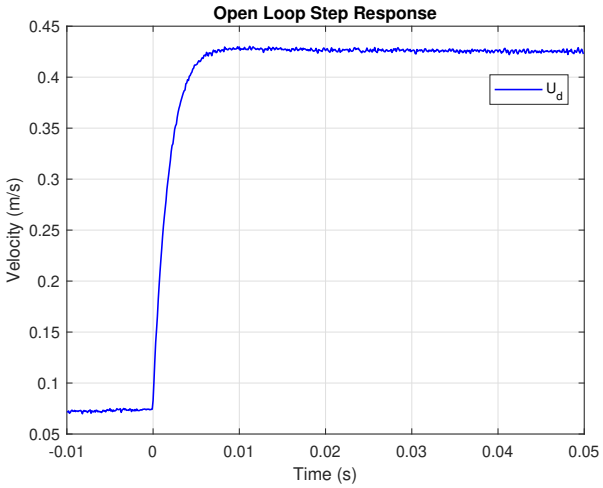

Figure 2.21: Open loop step response, also for an initial $V_d = 2.08V$ and final $V_d = 12.47V$ and $V_q = 0$, at resonance.

Then, the first order transfer function in q described alternatively in (2.24):

$$\frac{U_q}{G_q} = \frac{1}{2Ms + D} \tag{2.24}$$

The equation in (2.24) describes the open loop dynamic behaviour of the system to be controlled. It follows a first order type differential equation, allowing the use of a PI controller. The design for the d axis is also applied for the q axis. The open loop transfer function is the same for both d and q axes, as illustrated in Fig. 2.22.

The specifications, such as a response time and the overshoot, were set as no overshoot and $t_{5\%} = 3ms$. Then, the equation with the open loop transfer function of the plant and controller is depicted on (2.25).

$$OLTF = \left(K_P + \frac{K_I}{s}\right) \frac{1}{2Ms + D} \tag{2.25}$$

A compensation of the dominant pole is applied, then the relationship between the controller

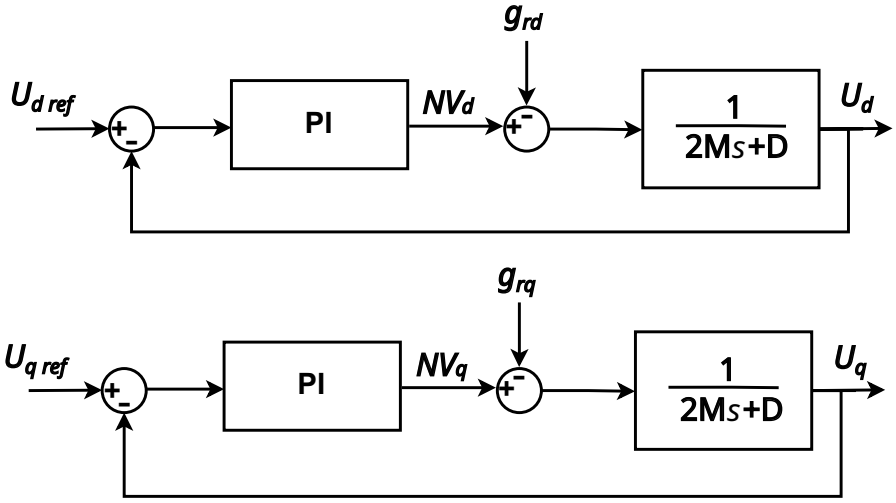

Figure 2.22: Block diagram: system in (d, q) reference frame and vectorial controllers

and plant parameters is $K_P/K_I = 2M/D$. Therefore, the open-loop function becomes K_I/Ds and the closed-loop transfer function (CLTF) of the system is:

$$CLTF = \frac{\frac{K_I}{Ds}}{1 + \frac{K_I}{Ds}} \tag{2.26}$$

For $t_{(5\%)} = 3$ms, the coefficients denoted in (2.25) resulted in $K_I = \frac{3D}{t_{(5\%)}}$ and $K_P = 3\frac{2M}{t_{(5\%)}}$.

Although having the Proportional and Integral Controller (PI) coefficients, the implementation of this controller in a DSP requires a conversion of the variables, since the microcontroller demand integers, and we work with voltages and velocities that, in the SI, are non-integers. Therefore, the conversion of voltage stipulated was $G_{cv} = 10000$ and for the velocity, $G_{cu} = 1000$. Then, when the vibration velocity required is 0.1 m/s, the device receives 100 a.u.

The values of K_P and K_I also demand a conversion. For that, the controller is discretized using the Tustin transform [139]. This transform, that takes in account the sampling time $T_s = 10\mu$s, has as controller coefficients G_a and G_b, that expressed in terms of K_P and K_I, give:

$$\begin{aligned} G_a &= \frac{G_{cv}}{G_{cu}} \frac{1}{N} \left(K_P + \left(K_I * \frac{T_s}{2} \right) \right) \\ G_b &= \frac{G_{cv}}{G_{cu}} \frac{1}{N} \left(K_P - \left(K_I * \frac{T_s}{2} \right) \right) \end{aligned} \tag{2.27}$$

Once controlled, the closed loop step presented in Figure 2.23 was performed experimen-

tally and in a simulation.

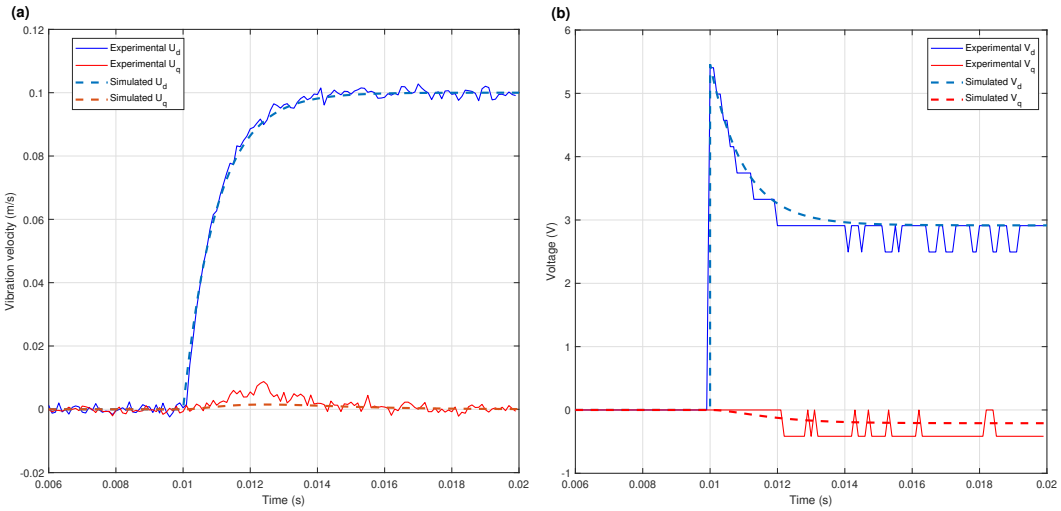

Figure 2.23: Experimental and simulated results of a closed loop step response: (a) velocity (b) voltage

As the velocity control is guaranteed, the measurements with the device are assured, using the methodology explained in the following chapter.

2.4 Chapter Conclusions

In this chapter, the LT was exposed, with the mechanical and electrical particularities clarified. The electrical and electromechanical models of this device were presented, pondering the non-linearities of the PE and the vibration behaviour of the device under different conditions.

The architecture of the device was then described, including the subsystems that were dissociated for better understanding of the construction and functions of the SAMIS. The first, the low-frequency ultrasound generation subsystem, was necessary for the excitation of the LT. The second, conditioners and sensors, are important to ensure the identification and control, and the proper functioning of the device. Lastly, we explained the normal force control, a subsystem that was designed for the practicality and reliability of the SAMIS as a medical tool.

The functioning of the probe depends on a reliable, controlled vibration. Then, the identification of the model and design of the controller were presented in this chapter. The mass-

spring-damper model was used, as it is well known in literature. The rotating reference frame, a convenient method to represent and control a PE structure, was shown and used for the identification of the device's parameters. Finally, a controller was designed using the vector controller method, and since the system follows a first order equation, PI was the perfect fit for that.

As for the challenges exposed for this thesis, in this chapter we solved the challenge 1: a vibration imposed and robust to the skin force g_r.

In the next chapter, we present the methodology of measurement, only possible once the steps presented in this chapter were concluded. The attempts made to build a protocol for the further tests are presented, along with the reliability tests the SAMIS was submitted to.

Chapter 3

Acoustical Mechanical Impedance of Skin

Once the device is identified and controlled, the methodology of measurement can be applied and experiments can be done. Before experimenting on participants, phantom skin is used to validate the methodology. Furthermore, tests are needed to set which protocols will be used for the experimentation, as they need to be as controlled as possible.

In this chapter, the methodology is presented, as well as preliminary tests to build the protocol. Particularly, the analysis of the system functioning with matching layers is made, probes with different resonance frequencies are tested, and the indentation force to be applied is chosen after some tests. Statistical analysis are made with the measurements of the SAMIS, to validate their repeatability and reproducibility. The results on the performance of the device are depicted in the chapter.

3.1 Measurement Method

As explained in chapter 1, the skin can be described as a viscoelastic material. It can be represented as an elastic load, especially when submitted to vibrations of $\leqslant$100 Hz. Then, for frequencies ¿100 Hz, it can be interpreted as a viscous material [141]. With a resonance at

about 300 Hz, there is the transition from elastic to inertial regime with damping [142].

The contact force g_r (Figure 2.14) applied by the skin over the LT create additional damping and stiffness to the system (LT+skin). When the vibration is controlled, the left part of equations in (3.1), for no-load and loaded (in-contact) operations, are equal for a given vibration.

$$\begin{cases} M\ddot{w} + D\dot{w} + Kw = Nv_{nl} \\ M\ddot{w} + D\dot{w} + Kw = Nv_{ic} - g_r \end{cases} \tag{3.1}$$

Then, the measurement of g_r requires a no-load test before testing the skin, and can be calculated using the voltage measured in contact (ic), v_{ic} and in no-load (nl) condition, v_{nl} as in equation (3.2):

$$g_r = N(v_{ic} - v_{nl}) \tag{3.2}$$

As a result, the voltage required for the loaded operation maintains the vibration of the device the same, compensating the effect of the skin, when added to the system. By measuring the difference between the voltage required in loaded and no-loaded operations, it is therefore possible to observe the interaction force g_r produced by the skin.

The measurement of the reaction force g_r is achieved at several vibration velocity values. By that way, it is possible to identify the increase of the force due to an increase of the vibration velocity. The vibration, force, and voltage of the system are represented in the rotating reference frame. In this representation, U_d is set as the phase reference. Then, the tests involved a vibration with a velocity reference $U_{refq} = 0$ and U_{refd} being a ramp that ranges from 0 to 0.1 m/s. The choice of a varying vibration velocity, with a tiny maximum, is proposed to avoid the intermittent contact. Indeed, in [23], the skin forces are measured for increasing vibrations from 0 to 0.5 μm. However, the curves often had a saturation point (see Figure 1.22, in chapter 1). The authors related this saturation to intermittent contact.

In our tests, we limited the vibration amplitude to 0.27 μm, to keep the probe in contact with the skin. Then, it is safer to say that the reaction forces are due to the behaviour of the skin. Moreover, in this condition, the force increases linearly with the vibration of the device. Then, observing the reaction force $g_r(t)$ as a linear function of the vibrating velocity $u(t)$, we can derive

the mechanical impedance as the slope of the curve.

Once the acoustical force is calculated, it is possible to find the Z_s of the material measured, that is defined as the ratio of force of the velocity, or the structure resistance when subjected to a vibration [9]. This relationship is described by 3.3:

$$Z_s = \frac{g_r(t)}{u(t)} = \frac{N(v_{ic}(t) - v_{nl}(t))}{u(t)} \tag{3.3}$$

Considering the Kelvin-Voigt model presented in Figure 1.11 with an additional mass, connected in series, we have the skin model of the Figure 3.1:

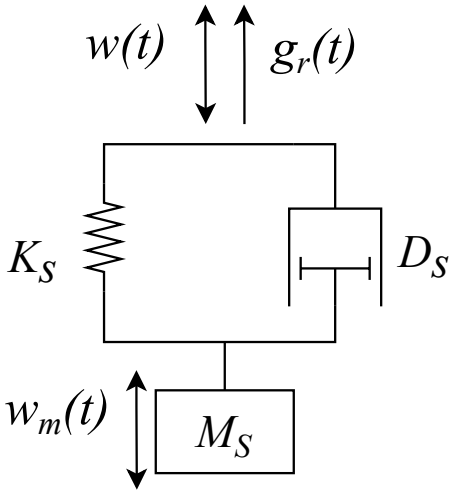

Figure 3.1: Mechanical skin model considering an MDK system

Then,

$$g_r(t) = D_s(\dot{w}(t) - \dot{w_m}(t)) + K_s(w(t) - w_m(t)) = M_s\ddot{w_m}(t) \tag{3.4}$$

where the m index stands for displacement over the mass, while $w(t)$ is the displacement of the spring and damper separately. Therefore, in the frequency domain:

$$g_r(s) = M_s s^2 w_m = D_s s\left(w - \frac{g_r}{M_s s^2}\right) + K_s\left(w - \frac{g_r}{M_s s^2}\right) \tag{3.5}$$

$$g_r\left(1 + \frac{K_s}{M_s s^2} + \frac{D_s s}{M_s s^2}\right) = (K_s + D_s s)w \tag{3.6}$$

When considering the velocity $u = \dot{w}$:

$$g_r \left(\frac{M_s s^2 + D_s s + K_s}{M_s s^2} \right) = \left(\frac{K_s + D_s s}{s} \right) u \tag{3.7}$$

Considering the equation (3.3),

$$Z_s = \frac{g_r}{u} = \frac{M_s s^2}{M_s s^2 + D_s s + K_s} \left(D_s + \frac{K_s}{s} \right) \tag{3.8}$$

As $s = j\omega$, then:

$$Z_s = \frac{-M_s \omega^2}{(K_s - M_s \omega^2)^2 + (D_s \omega)^2} ((K_s - M_s \omega^2) - j D_s \omega) \left(D_s + \frac{K_s}{j\omega} \right) \tag{3.9}$$

The representation of Z_s on the rotating reference frame has two components. The real one is related to the d axis, while the imaginary is related to the q axis. Taking the real part from equation (3.9):

$$\Re(Z_s) = \frac{M_s \omega^2}{(K_s - M_s \omega^2) + (D_s \omega)^2} (M_s \omega^2 D_s) \tag{3.10}$$

From the equations shown above, the real part of skin impedance is related mostly to its damping, mass and frequency. Indeed, the elastic component of the skin is negligible for the frequencies we work with. Due to issues on the interpretation of the imaginary component, and some experimental results that are difficult to interpret (negative values, for instance), we chose to disregard the imaginary, as it is shown on the tests following mentioned.

Then, for the next experiments presented, only the real component is taken in consideration. This component is here named Acoustical Mechanical Impedance (AMI), as in (3.11), due to the hypothesis that the mechanical behaviour of skin varies when submitted to acoustical forces [142].

$$AMI = \Re(Z_s) \tag{3.11}$$

As an example, Figure 3.2 presents, then, for an ordinary test, how AMI is extracted from a force-velocity curve.

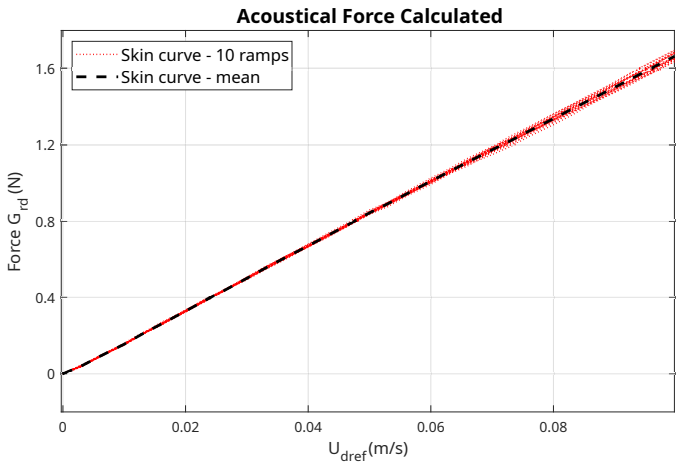

Figure 3.2: Acoustical mechanical force behaviour for a vibration increase: forearm skin of a healthy participant

On the figure, the curve drawn generated from a test with one healthy participant is shown. For this test, the velocity varied from 0 to 0.1 m/s, with 10 loops (0 to 0.1 m/s and 0.1 to 0 m/s). As it can be seen, the curves of the loops are linear, and with a low scattering ($<$5%). This scattering may happen due to a slight movement from the skin, or the delay effects of the skin comparing to the frequency o vibration of the device, characterised by the intermittent contact. As it is tiny, we do not consider it. Then, the AMI can be interpreted as the linear coefficient of the mean calculated from the 10 loops. On the example presented on the figure, $AMI = 24$ Ns/m.

Preliminary tests were made to evaluate the performance of the device, using rubber phantom skin. The experiments were performed with 3 samples of rubbers of Smooth-On namely Dragon Skin® 10 NV, Dragon Skin 20 and Dragon Skin 30. In [119], the same rubber was used to mimic a finger, focusing on the comparison of friction reduction between the rubber and a human finger, since both have similar stiffness. Figure 3.3 shows the shape of the samples.

Some mechanical properties such as hardness, tensile strength and Young's modulus are shown in Table 3.1. The first two were given by the manufacturer, while the latter was calculated using the equation (3.12). The tensile strength is the stress (of stretching or pulling) that can be applied to a material before it breaks. The hardness is the material's resistance to deformation by mechanical indentation. It is given in Shore A scale (S) and the relation between it and the

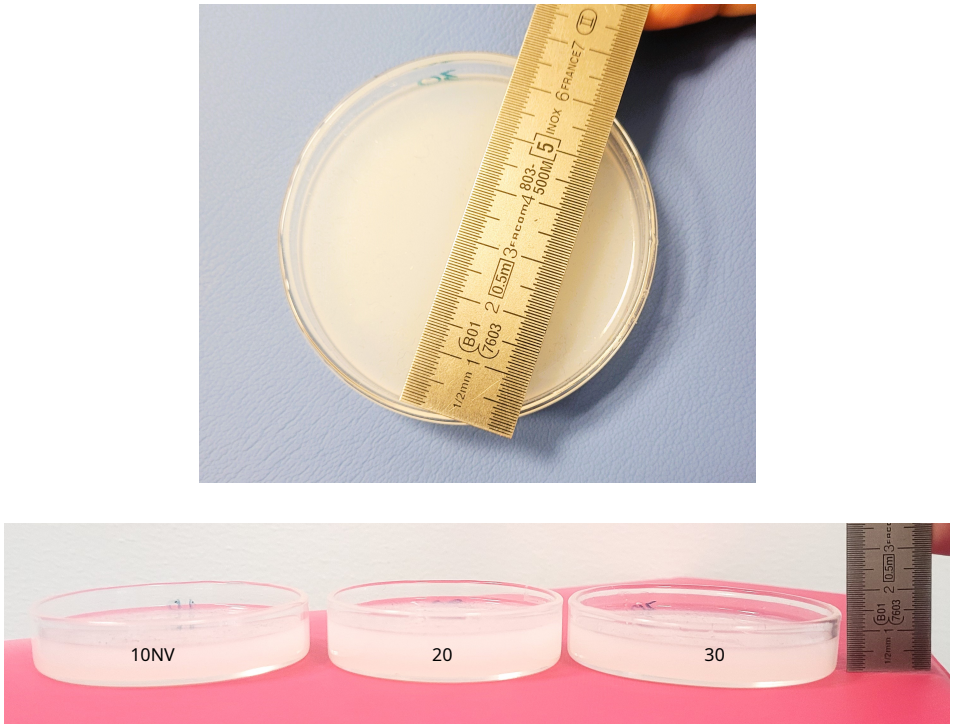

Figure 3.3: Samples of Dragon Skin®10 NV, Dragon Skin 20 and Dragon Skin 30, designed for the preliminary tests

Young's modulus (Y) in MPa is defined by [143] and depicted in equation (3.12).

$$Y = \frac{0.0981(56 + 7.62336S)}{0.137505(254 - 2.54S)} \tag{3.12}$$

Table 3.1: Dragon skin rubbers mechanical features

	DS 10NV	DS 20	DS 30
Hardness (Shore A)	10	20	30
Young's Modulus (MPa)	0.413	0.732	1.14
Tensile strength (MPa)	2.76	3.8	3.45

In [144], previous results for the phantoms were presented, when the device was not cased. These results are not relevant here because the device was not cased yet, and its parameters changed after the casing. Figure 3.4 presents the behaviour of the acoustic force components

G_{rd} and G_{rq} of the phantom samples for the vibration demanded, using the cased device.

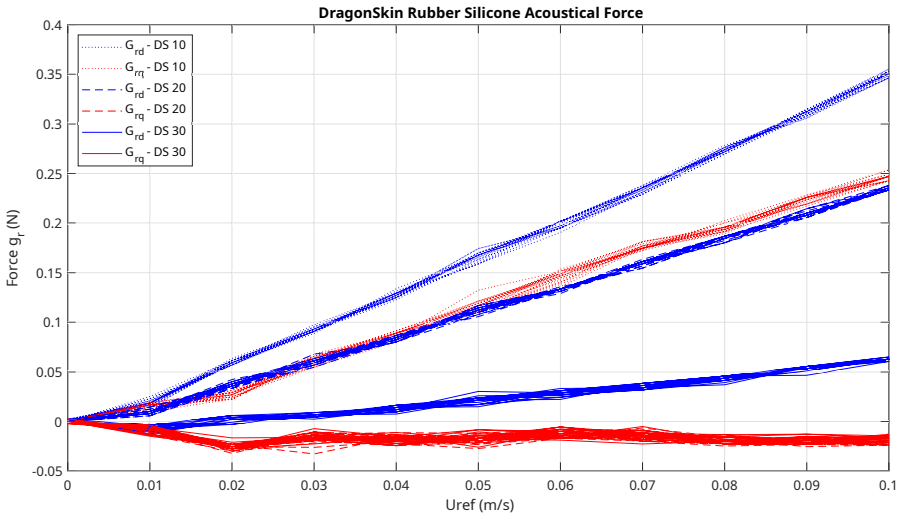

Figure 3.4: Acoustical force (g_r) of the 3 Dragon Skin elastomers as a function of the reference velocity U_{ref}: in red the d force component and in blue the q component

The imaginary component of the force g_r found experimentally was considered inconsistent, presenting sometimes negative values (for instance, for the DS 20 and 30, shown in Figure 3.4). We believe they are related to the non-linearities of the LT, such as the fluctuations on the resonance frequency, that appears when the device is on loaded condition [135].

The AMI values for the phantom skin samples, extracted from the Figure 3.4, are hence:

Table 3.2: Dragon skin rubbers AMI

	DS 10 NV	DS 20	DS 30
AMI (Ns/m)	3.5753	2.4419	0.7018

Using the values of Young's modulus (Y), presented in Table 3.1 against the values of AMI, for these three samples, we have the equation (3.13). This model, however, was only validated for these three dragon skin models.

$$Y = -0.2514 \cdot AMI + 1.3248 \tag{3.13}$$

Comparing the results of force from the human test ($AMI = 24$ Nm/s) and the rubber phan-

toms depict on Table 3.13, it is clear that the human finger has a higher AMI than the rubber. This result matches with the one presented in [119], where it is found that the damping of the skin is higher than for the Dragon Skin ®.

3.2 Building the Protocol for Skin Tests

As mentioned in chapter 1, skin mechanics can be characterised through different types of test and, depending on the configuration of the tests, the results might vary. However, for the same tests, it is required that the variables are as controlled as possible, so a low variation is expected. Then, in this section, the conditions chosen for the tests with the SAMIS are presented, as well as the methodology used for the election of the conditions (frequency of the probe, indentation applied and matching layer).

3.2.1 Frequency of the probe

The basal studies for this project, using LFU for skin characterisation, are described in [120, 145], where they use a 34 kHz vibrating plate and [23], where they also use a vibrating plate, but with a vibration of 25 kHz. In all the cases aforementioned, the goal of the vibration generation is the tactile feedback from the plate on the skin.

For the application of the LFU skin characterisation in this project, a probe was required rather than a plate, then, the LT was a better option. Once it was decided the use of an LT for the probe, one question arises about the specifications of the device: at which frequency the device should vibrate. Among the commercial models of LT, devices with similar frequencies than those previously studied (34 and 25 kHz) exist, but the surface of these LT were too large for the assessment of the areas we proposed to study – the smallest probe of 27 kHz had a diameter of 25 mm, while the probes chosen have 15 mm [146]. Indeed, for our measurements, we expect a full contact of the probe and the skin, which is difficult using large probes on certain areas of the skin.

Due to their size and easy use, small LTs were selected for the task. From Fuji ceramics, three probes were found (FBL60152SS, FBL60152SS and FBL60152SS), with nominal reso-

nance frequencies of 40 kHz, 50 kHz and 60 kHz. Their shape is different, as depict on Figure 3.5. However, as we decided to use the rear face of all LTs, the surface of contact is the same for all of these devices. There is evidence that the mechanical behaviour measured varies depending on the indentation probe size. In [110], for instance, after micro-indentation tests on the skin, it was found that the measured elastic modulus decreases with the increase in the radius of the used probe.

The choice of using different probes is to analyse the skin behaviour under these frequency conditions, since the skin itself has an intrinsic acoustic characteristic.

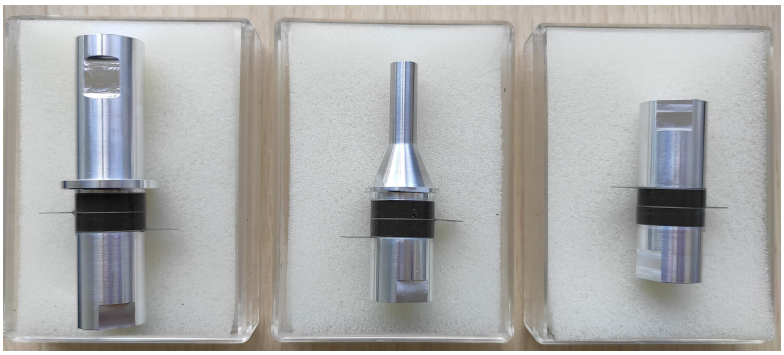

Figure 3.5: Probes tested for the device

At the moment of identification and control of the probes, different values of the system's parameters were found, and a controller was designed for each LT. These parameters were calculated using the methodology presented in 2.3 and are shown in Table 3.3.

Table 3.3: System and controller parameters for the three LT probes

Nominal f_0	Measured f_0	M (kg)	D (Ns/m)	N (N/V)	K_P	K_I
60 kHz	61065 Hz	0.0147	15.74	0.55	29.47	15740
50 kHz	49640 Hz	0.0039	5.725	0.458	7.8	5725
40 kHz	40010 Hz	0.0013	1.842	0.307	2.6	1842

On the code of the DSP, these values were made exchangeable, so the same set-up could be used. Experiments were made to compare the values of AMI measured by each probe. At the moment of the tests, it was also observed the AMI results for the palm of the hand and the

forearm, for comparison. The cohort for this experiment consisted of 8 participants, (6 male, 2 female), with an age range of 22 to 37 and Body Mass Index (BMI) between 20.2 and 30. Results for this test are presented in Figure 3.6.

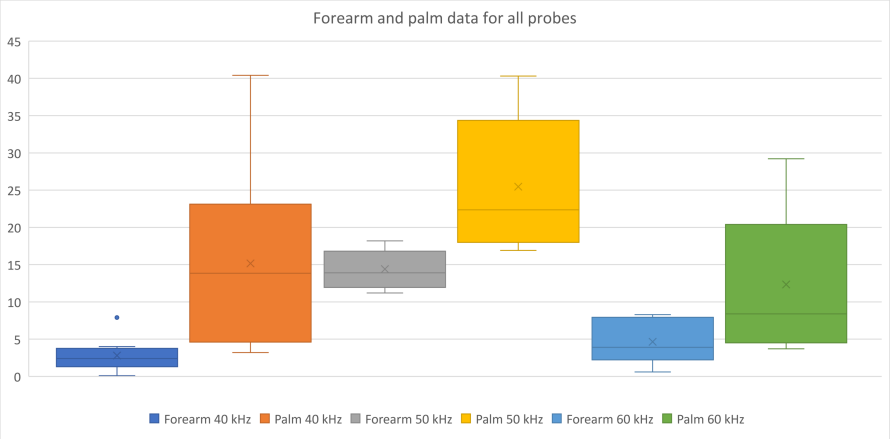

Figure 3.6: Results of AMI on the forearm and palm of the hand using the LT probes of 40 kHz, 50 kHz and 60 kHz

The results show that the AMI varies depending on the frequency, as noted in equation (3.10), even if we see a common tendency towards a higher dispersion for the palm than for the forearm. The investigation of this frequency dependence has not been deepened in this thesis; indeed, our goal is to discriminate the evolution of the skin behaviour according to its health situation, as it seemed time-demanding and the results of skin in different conditions was a priority for this thesis. Therefore, the 60 kHz probe, as it was the first one to be identified and used in our tests, was chosen for the continuity of the study.

3.2.2 Indentation force applied

To assure the reliability of the tests, the same conditions need to be established for the protocol. The normal force surveillance is one of them. The indentation force applied before an ultrasound stimulation can change the behaviour of the interaction, as it was presented in Figure 1.25.

The results presented on the figure, however, relate with indentations as high as 25 N, due to the nature of the study. In this scenario, the participant actively applies the skin force. In a diagnostic device, the force is imposed to the skin and not the other way around; and as it may

be imposed to a damaged skin, high forces should be avoided.

To evaluate how the indentation force influences the resonance frequency of the probe, we made some experiments, using the SAMIS and the Dragon Skin® 10NV (results depicted on Figure 3.7). The tests included a no-load operation, then loading with 0.2, 0.5, 1.0 and 1.5 N, and have shown that the highest is the normal force, the more the resonance frequency shifts from the no-load frequency value, as it can be noted from the values in Table 3.4. Between 0 N and 0.5 N, however, the difference was sufficiently large to be detected, yet low enough for the patient's comfort.

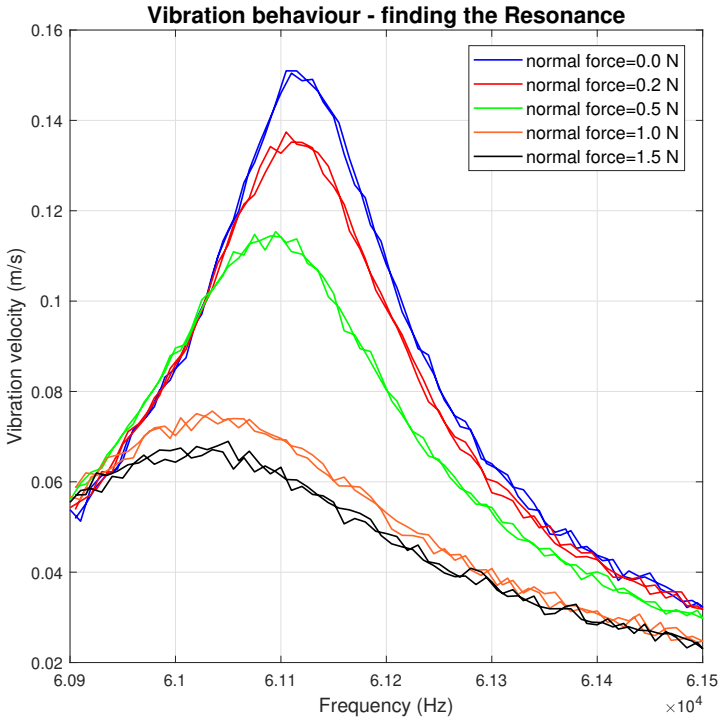

Figure 3.7: Vibration velocity of the LT during a frequency sweep test for different normal forces

Table 3.4: Resonance frequency for a variation on the normal force applied

normal force (N)	0.0	0.2	0.5	1.0	1.5
f_0 (Hz)	61115	61105	61095	61035	61050

Then, to set the normal force applied on the tests, trials on real skin, using 0.2, 0.3, 0.4 and 0.5 N were taken. It was noticed that the acoustical force g_r, and thus the AMI, changed with the indentation force imposed, but in a linear proportion. Figure 3.8 presents the set-up prepared at the moment of the tests. The rod of the tripod was lowered until the aimed contact force was attained, operating as an indentation controller.

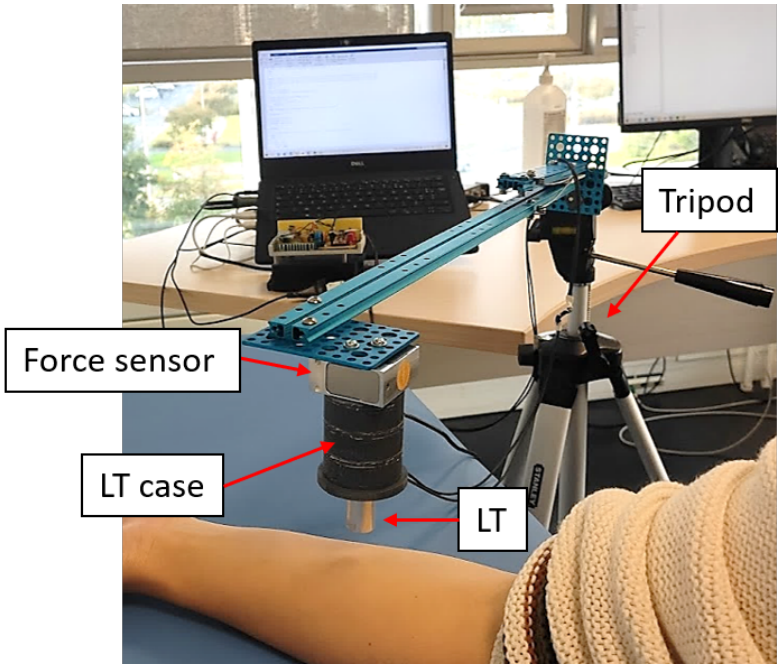

Figure 3.8: Set-up of the tests with the SAMIS

Figure 3.9 depicts this linear relationship found on the tests, with a linear coefficient of approximately 10. The indentation tests were made with the forearm of one participant (male, 30 years old and BMI of 21).

It should be emphasized that according to the model proposed in [23], the indentation force should not affect the results of the acoustical force g_r. But this behaviour has not been assessed in practice, as the authors did not change the normal force during their experiments.

In our experiments, we have a variation, but a lack of evidence to support the model for different indentation forces.

We make the hypothesis that the normal force changes the AMI because of the variation of the damping D_s. Indeed, the effective contact area is the surface of the skin that is actually in

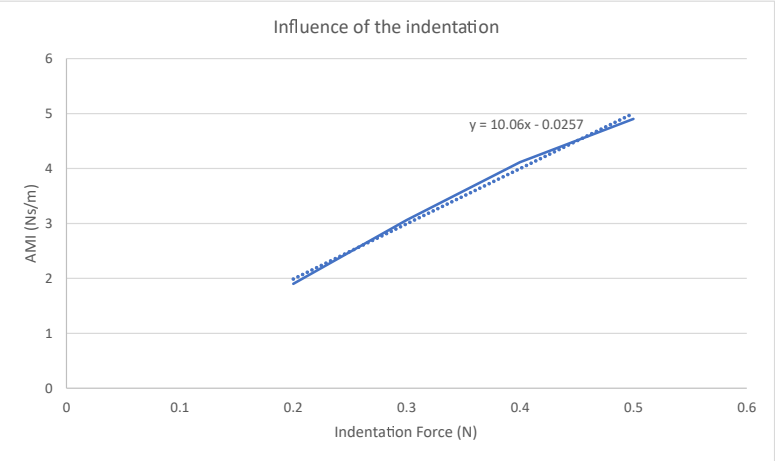

Figure 3.9: Relationship of indentation force and AMI for 0.2, 0.3, 0.4 and 0.5 N, in one participant's forearm.

contact with the probe. Due to the material's roughness and stiffness, the area of contact is not equal to the surface of the probe, but sightly smaller. The more normal force is applied, the biggest is the contact area [25]. A larger contact area results in more damping, as it implies more vibrating skin; thus, it increases the values of AMI. The equations (3.14), where A_e is the contact area, F_n is the normal force, and m and n are exponents, summarises the relationships:

$$\begin{aligned} D_s &\propto A_e^n \\ A_e &\propto F_n^m \end{aligned} \tag{3.14}$$

Experimentally, we found a linear relationship, because the normal forces applied in our tests were small. More tests can be performed to study the evolution of D_s with F_n; but in this thesis, we made the choice to not consider this variation, by using a constant $F_n = 0.2$ N in all trials.

The study proposed here requires a low deformation of the skin, to avoid these changes and still be able to fully contact it, since it may interfere to the skin integrity and its assessment. Therefore, it was chosen 0.2 N as indentation force for the next tests presented.

3.2.3 Matching layers

Often, in ultrasound medical devices applications, propagating media are used between the device and the skin. For the establishment of the SAMIS measurement protocol, some tests

were made to evaluate the media necessity and which coupling it was worth using.

The coupling of waves between PE devices and a media is challenging due to the mismatch in the acoustic properties [147]. Due to the high interdisciplinarity of the choice of a matching layer (knowledge on acoustics, vibration, electrical, electronics, signal processing, imaging, anatomy, physiology, materials, for instance) the literature studies have been mostly empirical.

For the tests of matching layers with the SAMIS, three materials were chosen: liquid water, hand cream and a sheet of Polycaprolactone (PLC), the latter being glued to the probe. In Figure 3.10, the values of AMI are presented with the presence of these matching layers.

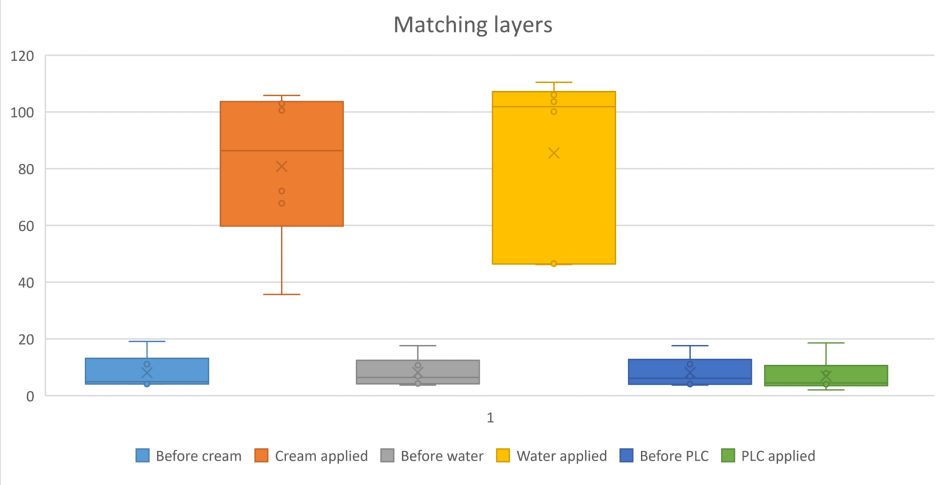

Figure 3.10: Results of AMI before and after the application of matching layers, for 6 participants' forearms

From the figure, it is demonstrated that the presence of a liquid or cream coupling highly affects the results. There is evidence that the water, as well as the moisturizer, affects the mechanics of skin [148, 14], being a bias for the measurements we want to take. These acoustic matching fluids increase the coupling largely, having results on the coupling rather than the skin itself. For the PLC, values are similar before and after the addition of the coupling, which is quite positive and kept for further tests, as it remains a barrier between the skin and the metallic part of the probe, preventing any electric shocks.

3.3 Characterising SCH, TEWL and AMI on healthy skin

For the skin characterisation and to evaluate the repeatability of the measurements, experiments were performed on healthy volunteers, on the volar forearm (as this site is easy to assess). To compare the results of SAMIS with conventional measurements, and possibly establish a correlation with the data collected, 2 other commercial probes were selected, dedicated to humidity and TEWL measurements.

The first probe chosen was the Corneometer® CM825, an instrument for measuring the hydration of the *Stratum Corneum* Hydration (SCH). This probe is produced by Courage + Khazaka electronic and can be found in [29].

The corneometer is a well known probe, able to assess skin moisture in a wide variety of physiological, pathological and experimental conditions. Therefore, it is commonly used in research investigations on skin health, such as the severity of psoriasis [149], to find symptoms of atopic dermatitis [150], to study the progress of moisturizing treatments [151], or even for the evaluation of skin moisture in newborn infants, as a way to characterise and enhance the development of the infants' skin [152].

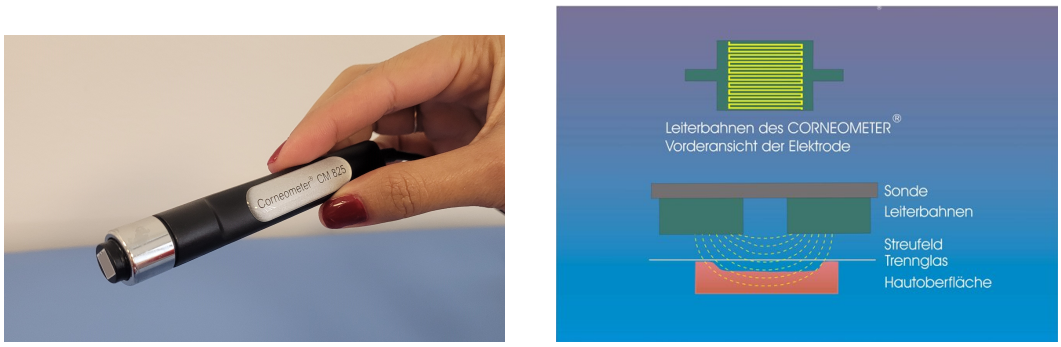

Figure 3.11: Corneometer® CM825 probe and its measurement principle [29]

The measures of the corneometer are based on the study of the dielectric properties of the skin, the SC. A schematic of the contact between the probe and the skin is presented in Figure 3.11. In the schematic, the dashed lines represent the scatter electrical field, that enter the SC structure. The dielectric behaviour of this layer varies according to its hydration, which is measured by the probe [29].

The second probe used was the Tewameter® TM Hex, also produced by Courage + Khazaka electronic. The device contains 30 pairs of sensors (relative humidity and temperature) that are disposed inside an open chamber (Figure 3.12), allowing the measurement in both sites of the probe. Thus, the creation of a microclimate during the takes is avoided, and the measurements consider the relative humidity of skin and environment, as this difference is the actual drive of TEWL [30].

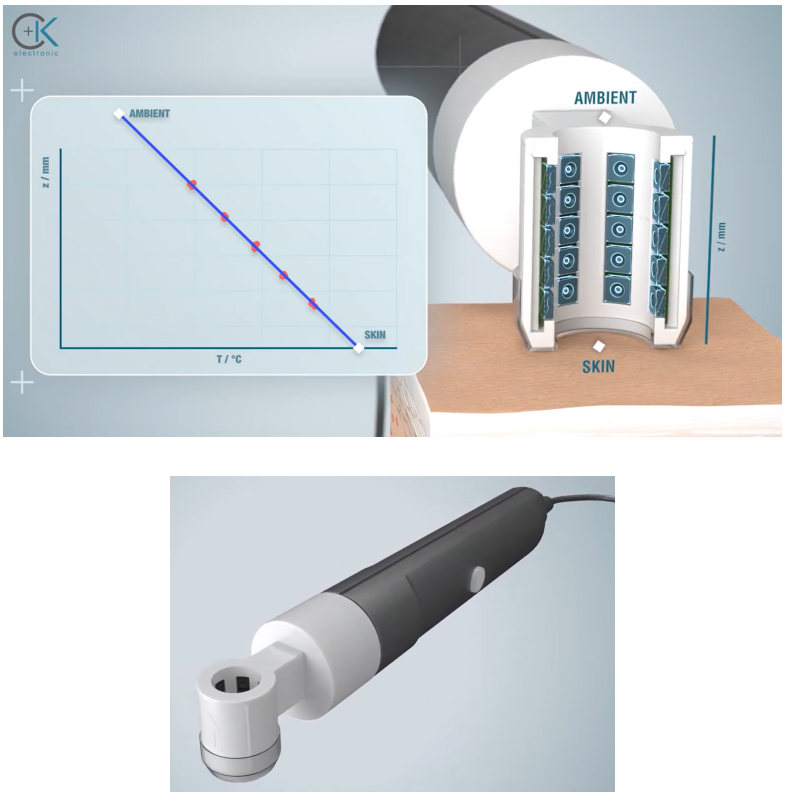

Figure 3.12: Above, tewameter sensors and principle of functioning. Below, the probe. [30]

The TEWL is calculated as a rate of transported water m, in grams over time t, as presented in (3.15). On the equation, A is the surface of the chamber (in m^2), $C = 0.0877$ g/m(h(mmHg)) is a diffusion constant, p is the vapour pressure of the atmosphere, (in mmHg) and x is the distance from skin surface to point of measurement, in meters. Then, the unit of TEWL is g/h/m^2.

$$\frac{dm}{dt} = -C \cdot A \cdot \frac{dp}{dx} \tag{3.15}$$

As presented in chapter 1, some studies were performed to link PU to SCH and TEWL [103]. Although powerful tools, the corneometer and tewameter are not able to detect PU objectively. The wound may change many of the skin properties, including moisture and TEWL, but these features alone are not decisive on the diagnosis of an early stage PU.

Thus, tests with SAMIS, corneometer and tewameter were proposed, to evaluate 3 different properties of the skin. The procedure for the tests had the approval of the University of Lille ethics committee and the ethics report entered the register of the data protection officer n. 2020-169.

Before recruiting the participants, some exclusion factors were established, to avoid bias on the results:

- Use of a drug treatment that may affect the skin somehow for the last 3 months;
- Participants on radio or chemotherapy for the last 3 months;
- Subjects with an amputation close to the studied area;
- Vascular surgery, angioplasty, or thrombolysis procedures for the last 6 weeks;
- People who regularly have rash / psoriasis;
- Previous skin replacement;
- Any other sort of skin problems on the sites tested.

The signature from the participant was collected, to prove that they agree to join the tests. The data anonymisation system follows the instructions from DPO (Data protection department) of the University, where the participants were classified by numbers. To prevent the association between the participant number and their name, the data from each participant and the list of names was saved separately and, once the study was finished, the list was destroyed, assuring the anonymisation of the study. The protocol timetable for a simple test is presented in Figure 3.13.

The cohort of these tests consists of 12 participants, 5 females and 7 males, with an age range of 26 to 67 years old and BMI between 20.2 and 27.7 kg/m^2. The collection of these data (age, gender and BMI) was interesting for further correlation with the AMI results, as it has been

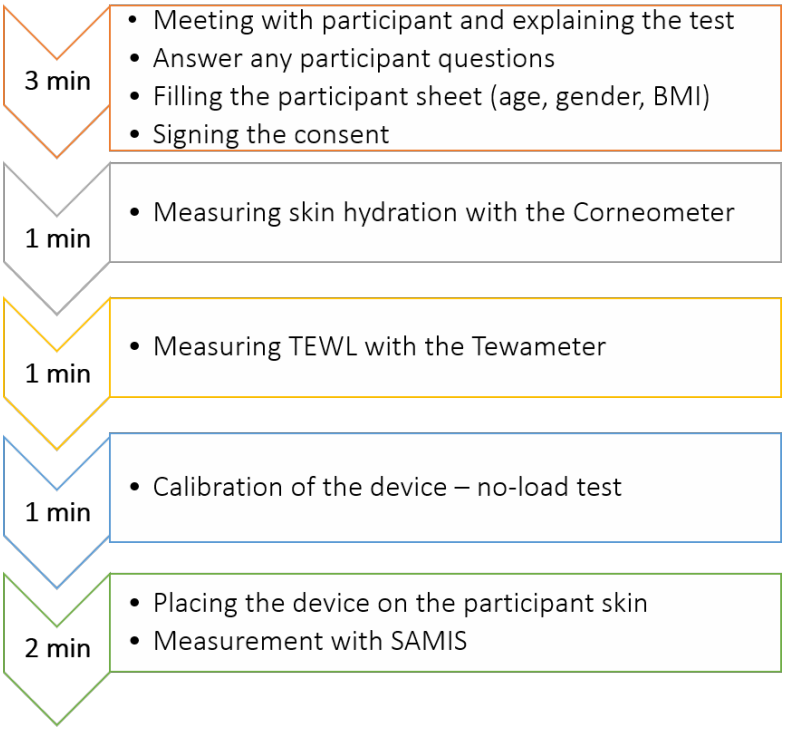

Figure 3.13: Timeline for a simple trial

proved they might vary depending on it [142] and because obesity and age have been directly linked to PU as comorbidity factors [153]. However, with small groups and with low variety of age and BMI, it was difficult, in this project, to cluster groups. Furthermore, the variation of BMI impacts more generally the hypodermis, whereas our measurements consider the outmost layer of skin. Table 3.5 presents the full participants' information sheet.

The set-up and positioning of the test are the same as presented in Figure 3.8. Each participant had the forearm cleaned with a hydro-alcoholic gel and waited about 2 minutes for it to dry out (meanwhile, we filled the information sheet and explained the test).

The tests were made in 2 sessions, one in the morning (between 9:00 and 12:00) and the other, in the afternoon, 4 hours later than the first session. For each session, one test was made with the corneometer, one with the tewameter and two, with the SAMIS. The tests with the corneometer involved 3 sequential takes, and the mean value was used the whole time. The 2 results of AMI in the morning are compared to each other, as well as the 2 in the afternoon.

Shapiro-Wilk and Kolmogorov-Smirnov normality tests were made with the results of SAMIS,

Table 3.5: Cohort of participants for the repeatability test

Participant	Gender	Age	BMI
1	F	27	20.2
2	F	37	21.9
3	F	32	22.4
4	M	33	21.0
5	M	27	27.7
6	M	30	20.7
7	F	29	24.4
8	M	48	25.0
9	M	58	24.8
10	M	67	24.7
11	F	26	21.8
12	M	28	21.6

indicating that, for the population tested, the results have a normal distribution. The results for these tests are presented in Table 3.6.

The Shapiro–Wilk test is used to verify the null hypothesis that a sample came from a normally distributed population. The value W, when close to 1, indicates that the distribution is close to normal. The null-hypothesis of this test is that the variable in this population is normally distributed. Thus, if the $p - value$ is less than the chosen alpha level, then 0.5, in our test, it means the null hypothesis is rejected and there is evidence that the data tested are not normally distributed [154].

The second test used, to strengthen the null-hypothesis of a normal distributed AMI, is the Kolmogorov–Smirnov, a non-parametric test of the equality of continuous one-dimensional probability distributions. In this test, a sample is compared with a reference probability distribution, i.e., it quantifies a distance between the empirical distribution function of the sample and the cumulative distribution function of the reference distribution. This distance, namely KS, is used to calculate the p-value, computed from the maximum distance between the cumulative frequency distributions [155].

Table 3.6: Normality tests executed for AMI results

Shapiro-Wilk Test	Morning	Afternoon
W	0.9068	0.9284
p-value	0.1939	0.3640
Normal (alpha=0.05)	Yes	Yes
Kolmogorov-Smirnov Test		
KS distance	0.2005	0.1831
p-value	$>$0.1000	$>$0.1000
Normal (alpha=0.05)	Yes	Yes

Then, for the AMI collected in the morning and afternoon, paired t-tests were executed, to evaluate if there is a statistically significant difference between the 2 trials. The normality test was needed because this statistical evaluation requires a normal distributed variable for exactness.

A statistical hypothesis test, the t-test, is used to verify if a variable sample follows a Student's t-distribution under the null hypothesis. When running a paired t-test, the goal is to analyse the difference between pairs. Then, it computes the average difference, the 95% CI of that difference, and a p-value, by testing the null hypothesis that the mean difference is indeed zero [156].

For both cases (morning and afternoon), p-value $>$ 0.05, indicating that the measurements were statistically equal. In the table, results of a t-test comparing the mean of the values in the morning and the mean of the afternoon show a p-value$<$0.05, meaning that there is a high difference between tests. This change is not shocking: that can be due to a higher temperature found in the afternoon or the effect of sweat during the 4 hours gap between the takes. The values of R^2 quantifies the degree of any linear correlation.

An analogy of this behaviour is what happens in a weight scale: when a person weights herself twice in the morning, low or no variation on the results is expected. However, measuring with a large time gap, it is absolutely normal to see some variation between the values, as during the day this person may spend and consume energy.

Table 3.7: t-test results for morning and afternoon tests

Repeated measures t-test summary	Morning	Afternoon	Morning vs Afternoon
p-value	0.1486	0.2932	0.0098
Statistically significant (p-value $<$ 0.05)?	No	No	Yes
R^2	0.1799	0.0997	0.4692

The results of the morning and afternoon tests are presented in Figure 3.14. From the figure, it is clear that not much difference is seen from the results, when comparing the tests separately.

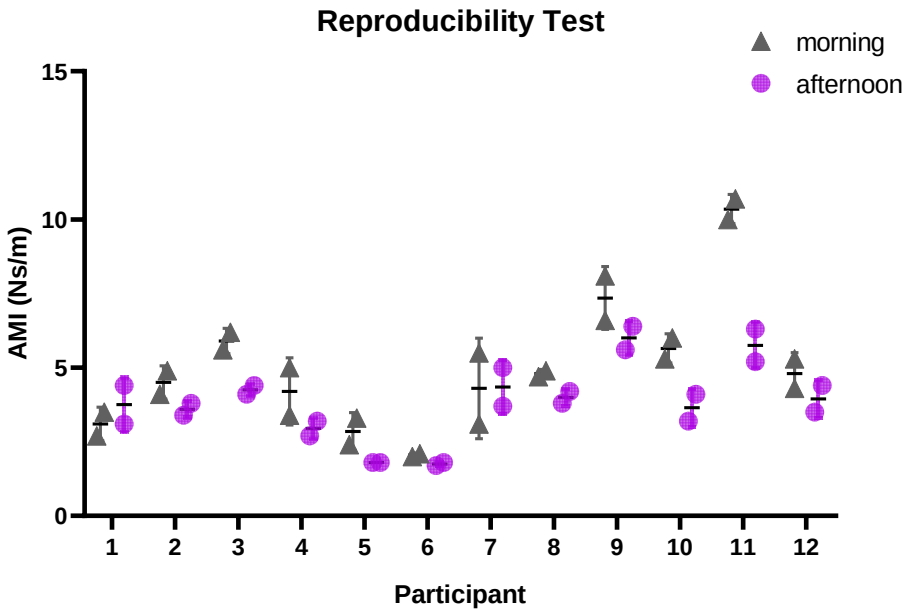

Figure 3.14: Absolute values of AMI for all the trials, for 13 participants

Once the data of AMI was analysed alone and seemed strongly repeatable, we could run a correlation test between the mean of each test and the SCH, measured by the corneometer. Figure 3.15 presents a linear correlation graph, with the R values for each case.

This relationship is measured by the Pearson correlation coefficient (R), a well-established measure of the strength and direction of the linear relationship between two quantitative variables [157]. The R value can range from -1 to 1, where 0 means there is no correlation and R$>$0.5 means there is a strong and positive correlation. Therefore, from the relation described

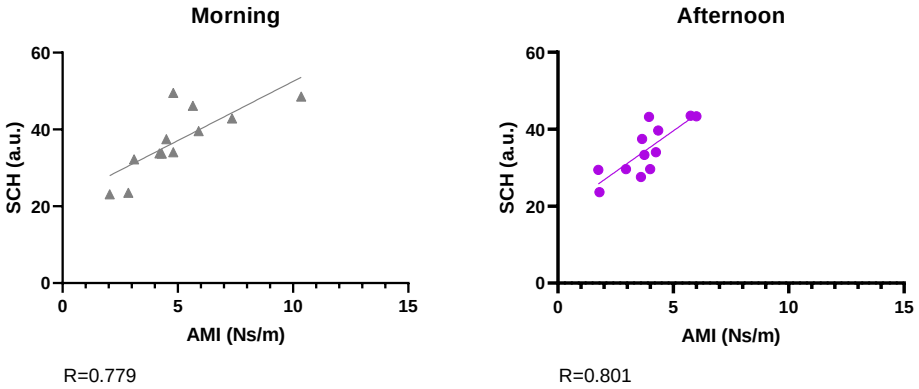

Figure 3.15: Correlation of SCH and AMI for the morning and afternoon tests, with linear trend lines

in the Figure 3.15, a strong linear relationship was found between AMI and SCH, which is in accordance with results from current literature.

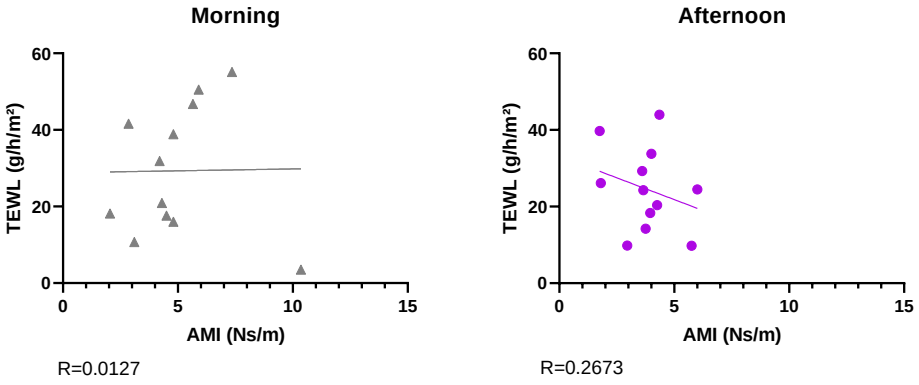

Figure 3.16: Correlation of TEWL and AMI for the morning and afternoon tests, with linear trend lines

Evaluating the correlation between AMI and TEWL, presented in Figure 3.16, low values of R were found, indicating a weak linear relationship between these parameters.

3.4 Chapter Conclusions

In this chapter, the methodology of measurements using the SAMIS was presented, including the no-load and loaded measurements. The first tests, using phantom skin, were presented to validate the measurement.

The efforts to establish a consistent protocol to be used for all the next tests are presented. Attempts to use other LT probes, including the characterisation of each, results with them, in a test comparing 2 skin sites are exposed. As the 60 kHz LT was implemented since the beginning of our tests, we chose to keep the next steps using it.

Another important factor for the reliability of the experiments using the SAMIS is the use of the same normal force. Literature show that the LT resonance frequency slightly changes when a load is applied to it, then, the force of indentation has to be chosen with criteria. In this chapter, the experiments for that are presented, and the force chosen was 0.2 N.

The last experiment to establish the protocol was the addition of a matching layer between the SAMIS and the skin. It was noticed that liquid and creamy mediums completely interfered with the results. Then, a sheet of PLC was used; it is a hydrophobic material, and it can cover the metal body of the device, preventing the skin to be tested to suffer from possible static electricity shocks.

Once the protocol was decided, tests to characterise healthy skin were presented. The first approach of the tests aimed to evaluate the repeatability and reproducibility of the SAMIS measures, ensuring a reliability of the device. From 2 normality and 1 t-test, the results of AMI seemed coherent.

Then, to build a data set on healthy skin, and evaluate the impact of SCH and TEWL on AMI values, the experiments included the measurement of all 3 parameters. The results show a strong linear correlation of AMI and SCH, which is in accordance to literature. The barrier function of skin was not particularly correlated to the AMI.

As for the challenges exposed for this thesis, in this chapter we solved the challenge 2: a reliable measurement of this force.

In the next chapter, tests on skin in different conditions and sites are proposed to strengthen the hypothesis of the skin parameters relationship and the reliability of the SAMIS to measure

and identify the variation of these conditions.

Chapter 4

Skin Characterisation with Low-Frequency Ultrasound

In this chapter, tests using the SAMIS to identify skin in different conditions are presented. The tests also involve the measurements of SCH with a corneometer, to continue the investigation on the correlation of these measurements.

Since the protocol to test real patients requires a CE marked device, and our prototype is in its first version, the experiments were all made on healthy volunteers. To validate the probe, we tested the device on several conditions of the skin, and even in healthy skin, some experiments were dedicated to study damaged skin; for that, protocols to simulate skin damage were performed. The results obtained with the SAMIS were compared to results from Corneometer® and Tewameter®, giving a reliable reference measurements of these conditions. This step is fundamental to assure the security of the device for, in a future work, PU at-risk patients assessment.

The first case study presented is made to evaluate if the device is capable of distinguishing the skin in different spots. The skin thickness and tissue arrangement have great impact on its mechanical properties. With the first case study, we demonstrate how the AMI is influenced by the location of the measurement.

In the second, the results of a test on the same site, but with parameters changed, are presented. In this study, 3 changes are proposed: moisturising skin with water, removing of

some SC layers with a razor and creating a microclimate with the application of a plaster for 4 hours. The aim is to evaluate the impact of these treatments on the AMI, as they can change skin conditions.

On the third case study of the chapter, tests involving healthy skin, before and after insults, are presented. The evaluation of the TEWL, measured with a tewameter, is also presented. With this test, the skin was submitted to a continuous load, intermittent load and tape-stripping, to simulate the pressure and inflammation on the skin and evaluate its state right after the insults and after its recovery (30 minutes later).

For each of these case studies, we present the protocol, cohort, results, and discussion of the results.

4.1 Case Study: Distinguishing Skin in Two Sites

Several studies have proved that the mechanical properties of skin change along the body, depending on the type of skin (glabrous and non-glabrous), the site assessed (abdominal, facial, sacral, for instance), the thickness or the amount of blood on the area [158, 159].

In [31], *in-vivo* tensile tests over the back of a human are presented, and the results of the stress-strain curves (Figure 4.1) are greatly different according to the site and direction of tests.

In [160], several regions of the body are considered: distal, middle, and proximal forearm, abdomen, and anterior or posterior thigh and calf. The elastic modulus from these areas varied from 6.6 kPa, on the abdomen, to 61.0 kPa on the anterior tight.

However, a study from [9] evaluated the MI of the palm of the hand in 10 different locations, using a vibrator with sine-wave signals for stimulation delivered by an increasing frequency from 20-10000 Hz. For the 10 locations, there was a low variation on the skin parameters (they used the Kelvin-Voigt model with the addition of a mass), since the sites studied are very close and have similar structures and thickness.

The case study presented in this section is designed to evaluate the measurements of the device when applied on mechanically different structures of the same skin. The forearm, a hairy and non-glabrous skin, has different mechanical parameters than the palm of the hand.

In Chapter 3, the same type of experiment, was presented to assess the performance of the

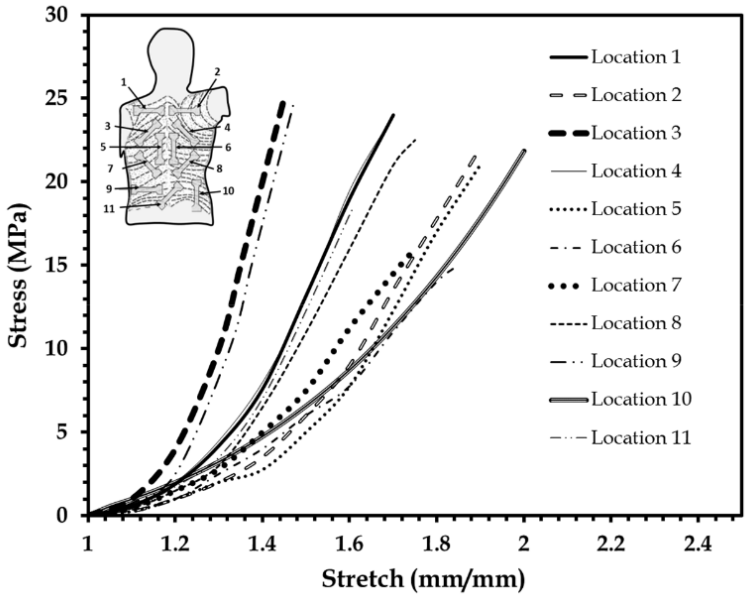

Figure 4.1: Stress-strain (here named stretch) curves on the back of a human, presented on [31]

SAMIS in distinguishing skin in 2 sites. Here, the test is retaken, with a wider cohort, allowing a better statistical analysis and crossing this data with SCH, measured during the trials.

The steps and goals of these tests are:

- Recruit healthy participants and test the skin in 2 sites (forearm and palm of the hand);
- Crossing data from measurements of SAMIS and SCH;
- Evaluate the difference between the 2 sites and compare, as well as compare the difference found with the 2 devices.

4.1.1 Protocol

These experiments were performed in about 10 minutes for each participant. First, the participant signed the consent. Then, the skin was cleaned, with hydro-alcoholic gel, in both sites to be measured.

The sites studied are presented in Figure 4.2. The location chosen in the volar forearm was about 50 mm from the anterior elbow, and in the palm, the thenar eminence. These areas are

easy to assess and flat enough to contact the whole surface of the probe. In all cases, the left arm was used, as a matter of positioning comfort of the participant during the takes.

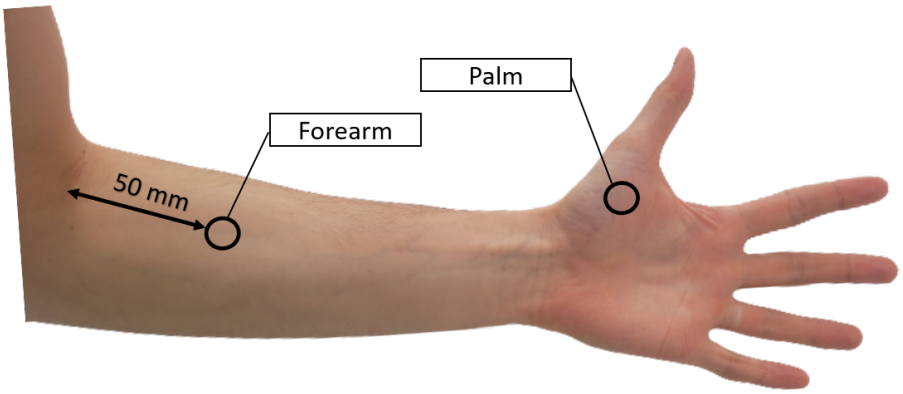

Figure 4.2: Sites tests for the palm – forearm test

Once the sites were identified and marked with a pen on the participant, the corneometer was used to measure the SCH right above the mark, while a no-load test was running for the SAMIS. Then, the AMI was measured on the same spots.

4.1.2 Cohort of participants

For these tests, 20 participants were recruited, 10 males and 10 females. The age range was 23 to 58 years old (31.6 average) and the BMI was between 18.61 and 38.87 kg/m^2 (23.34 average).

The procedure for the tests were included in the ethics report entered in the register of the data protection officer n. 2020-169, the same report used for the repeatability test.

The full list detailing the participants' code, gender, age and BMI is found in A.1.

4.1.3 Results and discussion

The values of AMI for the palm and forearm are presented in Figure 4.3. From the figure, the variation of results between palm and forearm is clear. The averages shown on the blocks are

6.44 Ns/m for the palm and 2.14 Ns/m for the forearm, and albeit for some participants the AMI was low on the palm, in all cases, when verified individually, the AMI of the palm was higher than the measure of the forearm.

Each participant had a result inherent to their skin properties. The overall variation coefficient was of 62.84% for the palm and 30.05% on the forearm.

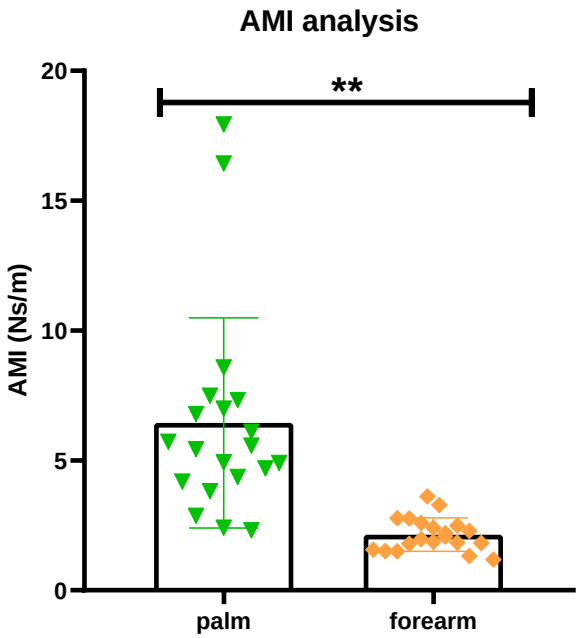

Figure 4.3: Results for AMI on the palm and forearm

When the data of SCH was analysed, a similar variation was expected between the results on the two sites, as the palm often sweats more than the forearm. However, what was found is that for some participants, the SCH was higher in the forearm than in the palm. The averages shown on the blocks depicted in Figure 4.4 are 33.84 a.u. for the palm and 33.45 a.u. for the forearm.

These results indicate that, although SCH is an important factor of the skin mechanics, other parameters influence on the result of AMI.

To reinforce the evaluation of the ability of the device to distinguish these two sites, a t-Test

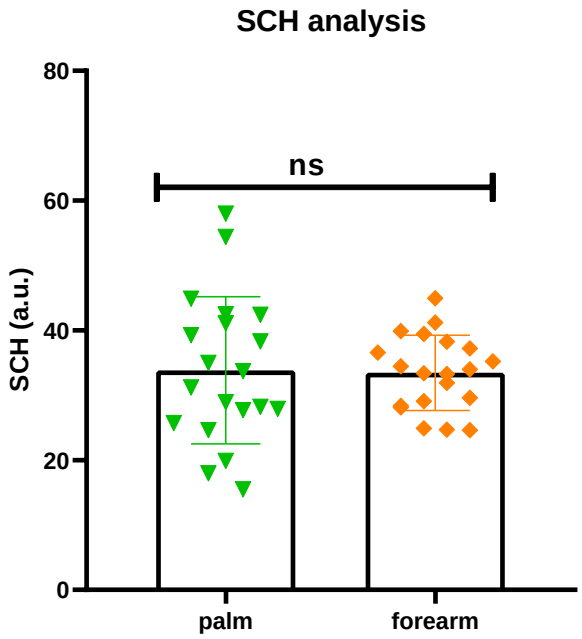

Figure 4.4: Results for SCH on the palm and forearm

was run for both AMI and SCH results. Table 4.1 presents the outcomes from this statistical test.

Table 4.1: t-Test found in the Palm – Forearm

Paired t-Test	SCH	AMI
p-value	0.8817	0.0002
p-value summary	ns	***
Significantly different (P $<$0.05)?	No	Yes

The p-value for the AMI is lower than 0.05, which demonstrates that there is a statistically significant difference between the values measured on both sites. For the same test ran on the SCH values, the p-value was 0.8817, suggesting that the values of the palm and forearm are highly similar.

4.1.4 Study conclusion

This study was proposed to evaluate the performance of the measurements. The results show that the SAMIS is able to discriminate the skin in different sites, despite the similarity found with the SCH measurements.

4.2 Case Study: what is the effect of Water, Razors, and Plasters on the skin?

In literature, the mechanical properties of SC are often related to the water content and number of layers [14, 16, 91, 92, 151, 152, 159]. The change of these parameters, along with the microclimate that might be created when skin is covered, are interesting when assessing PU risk in a patient [37, 52, 2].

In [90], an indentation test was performed in dry and wet skin, where the wet state was the skin moisturized with water. For the indentation test, the authors executed loading cycles to evaluate the results after the moisture-induced changes. The results indicate that the skin presents a “softening” effect, when moisturized. These changes, although substantial (up to 50%), are reversible. A second study where hydration was induced on the skin is presented in [36]. The goal was to evaluate the impact of moisture on the thickness of the SC, as well as the roughness of the tissue, after 1 hour of water absorption. The results show that the thickness can increase up to 95%, once hydrated, and the roughness, up to 58%.

In [32], a wet and dry test was performed for the skin on the back of the hand. In their experiments, the skin was subjected to low amplitude, in-plane vibrations with a constant $w(t) = 0.06$ mm and frequency ranging from 0 to 1024 kHz. The wet condition was achieved by soaking the hand of the participant for 5 minutes in water. The results of damping length found for this experiment are presented in Figure 4.5.

From the results of Potts et al. [32], the dynamic shear viscosity decreases with the increase of frequency and stabilises after about 700 Hz. The results also suggest that a moisturised skin decreases the stiffness of the SC.

As for the effect of shaving on skin, most studies are focused on the cosmetic approach, and

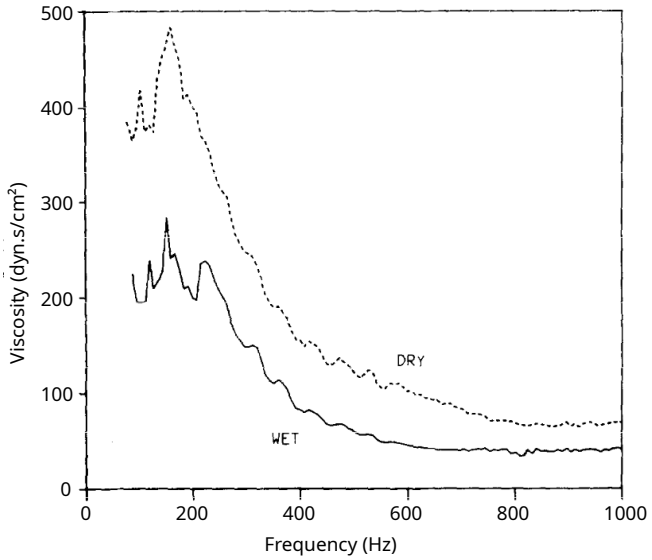

Figure 4.5: Dynamic shear viscosity against frequency for skin from the back of the hand. Adapted from [32].

on the facial and neck areas. When a razor is applied against the skin, it causes a mechanical stimulus. This interaction has a mechanical impact on the skin, such as the removal of the hair, along with surface corneocytes, and depending on the blade, an increase of blood flux, as it was measured in [161]. Furthermore, blade shaving can trigger the skin nerve endings via keratinocytes, which might result in an irritation of the area. These irritations and the subsequent inflammatory reactions induced with shaving can be caused by trauma due to superficial skin abrasion, or by interaction with the hair shaft, that transmits signals to the peri-follicular skin compartment [162].

The microclimate, defined by the temperature and moisture conditions on a local scale of the skin, is an important aspect when investigating PU, as it can be one risk factor. The patients' dressings, use of nappies, ambient condition and individual's fluids (sweat, urine, for instance), can generate a microclimate, that is especially dangerous in bony prominences. It was shown that the thermodynamic conditions over the skin tissue have a great influence on the incidence of PU, [37]. As the excessive moisture undermine skin stiffness and strength, potentially weakening the tissue, it is worth to investigate a possible effect of it, using the SAMIS.

In this context, this study, named Water, Razor and Pad test (WRaP), was proposed to

evaluate the impact of the variation of skin parameters on AMI and SCH measurements. The objectives of the experiments are:

- Recruit healthy participants and test the skin in 4 sites: control, moisturizing with water, passing a razor and dressing the skin with a medical plaster for 4 hours
- Verifying the measurements values for baseline, and comparing with the results after treatment
- Crossing data from measurements of SAMIS and measurements from the Corneometer®

4.2.1 Protocol

For this study, 3 treatments were applied on the skin: water application, shaving with a razor and covering the area with a plaster.

Considering the treatments and control, 4 sites on the forearm were assessed, as depicted in Figure 4.6. The sites for treatments and control were chosen randomly, i.e. for each subject, the control, watering, plaster application and razor sites were varied.

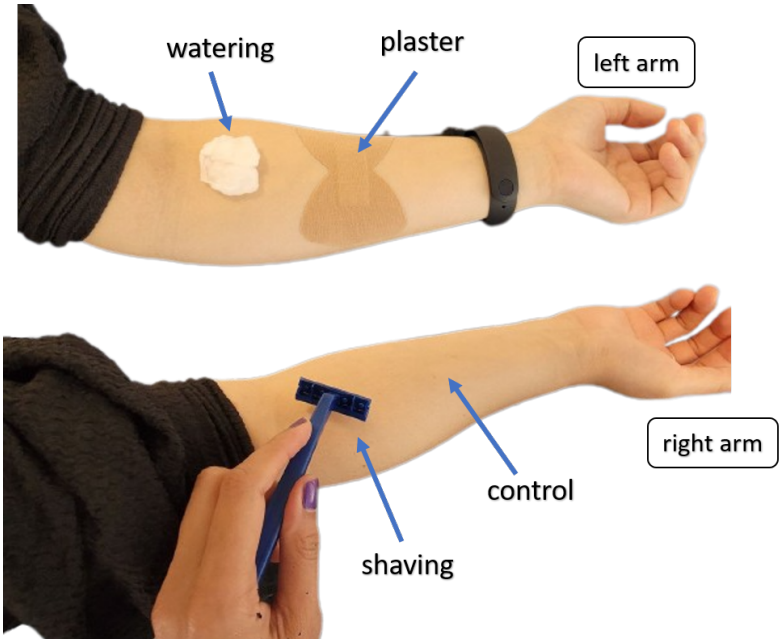

Figure 4.6: Treatment and control sites in one participant

Prior to the tests, all sites were cleaned with a wipe and hydro-alcoholic gel. For the water treatment, it was applied for a short duration (5 to 10 seconds) using a cotton piece. Then, with a clean wipe, the area was dried, and the test was taken right after. The razor test consisted of the shaving of the site by passing the razor 5 times.

The timeline of the test comprised 2 sessions, as detailed in Figure 4.7. In the first one, the baseline data were collected for all sites, and only water and shaving treatments were assessed. Then, after 4 hours, the control was measured and the plaster was removed, so we could assess the uncovered area.

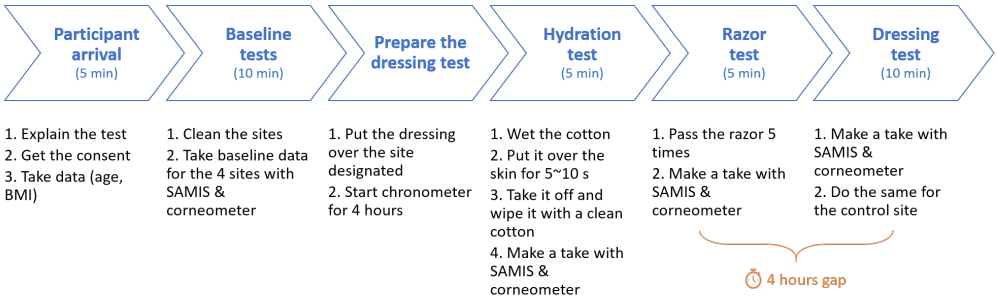

Figure 4.7: Timeline of the WRaP tests

4.2.2 Cohort of participants

For these tests, 20 participants were recruited, 11 males and 9 females. The age range was 24 to 42 years old (30.4 average) and the BMI was between 17.94 and 38.87 kg/m^2 (23.02 average).

The procedure for the tests were included in the ethics report entered in the register of the data protection officer n. 2020-169, the same report used for the previously presented tests.

The full list detailing the participants' code, gender, age and BMI is found in A.2.

4.2.3 Results and discussion

The results of AMI found with this test are depicted in Figure 4.8.

From the results, it is clear that the means of the control, razor, and plaster are highly similar, when comparing baseline measurements and treated ones. To evaluate the statistical variation

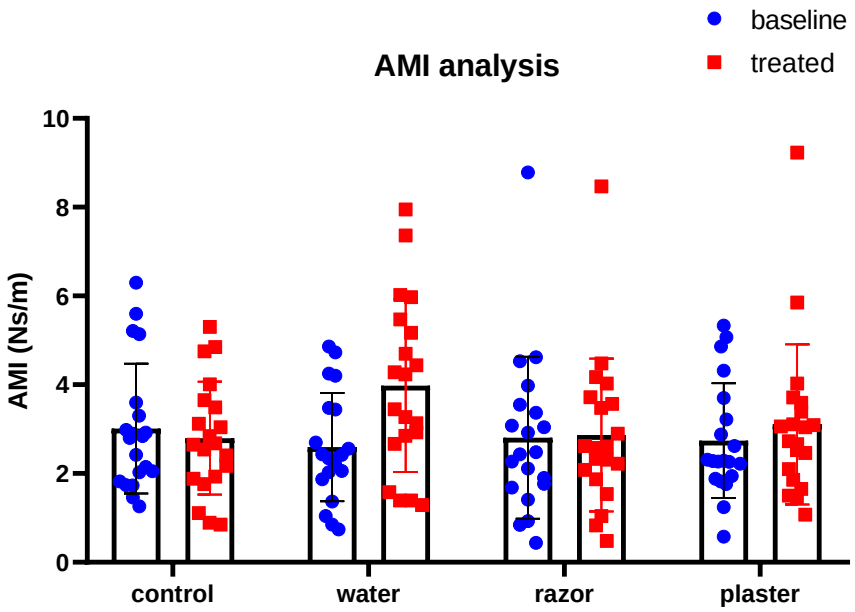

Figure 4.8: Results for AMI on the forearm for the different treatments

of the values found, we ran t-Tests. The results of AMI for the 4 sites showed that only the application of water was detected by the device. Table 4.2 summarises the result of the t-Tests for each treatment.

Table 4.2: t-Test found in the WRaP test – AMI

Paired t-Test	Control	Water	Razor	Plaster
p-value	0.4204	0.0007	0.7653	0.2782
p-value summary	ns	***	ns	ns
Significantly different (P <0.05)?	No	Yes	No	No

The control, as expected, had similar means from before and after the 4 hours gap. It reinforces the reproducibility of the SAMIS measurements. The results for the razor treatment, however, were also quite similar. A possible cause for this is that the shaving was not rough enough to remove skin layers, but only the hair (when present). The microclimate created by the plaster went unnoticed, which can also be a result of a light treatment. The time for the microclimate was 4 hours for the test, while in real plaster uses, the removal is done daily,

then, every 24 hours [163]. This short time may create a microclimate that may not affect the mechanics of skin.

For the same tests, the results of SCH are presented on the Figure 4.9.

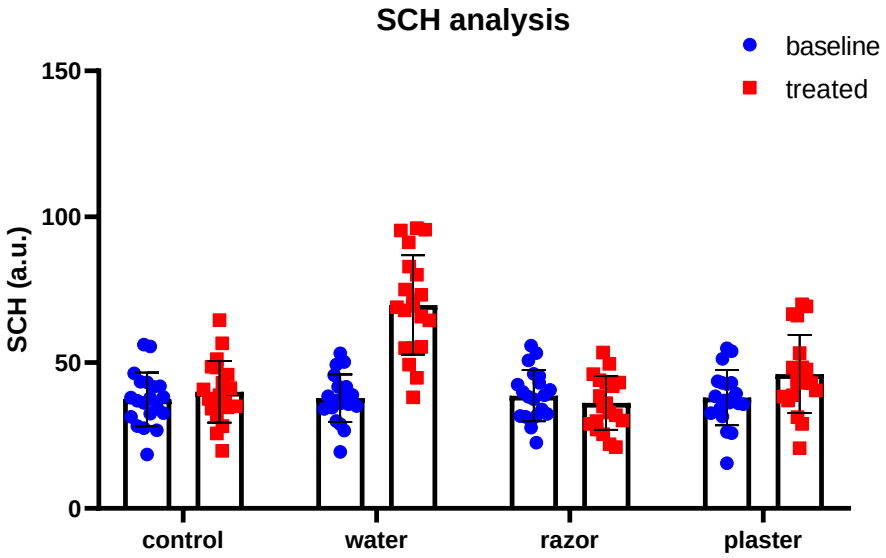

Figure 4.9: Results for SCH on the forearm for the different treatments

The results of SCH t-test, presented in Table 4.3, show high p-values for control, watering, and plaster application. Although the p-value was close to 0.05, the same behaviour, the 4 hours gap between the control tests can explain the different results, as the participants possibly had activities and sweat in between the takes. The comparison of results for the plaster also had a statistically significant difference, due to the sweat from the microclimate created. As these measurements are focused on hydration, the high difference between before and after moisturising of the skin was obviously expected. For the results of the razor test, it passed unnoticed again, but for this one, we had no expectations.

The summary of averages from the 4 sites and for both SCH and AMI tests can be found in Table 4.4. From these results, the lack, or presence of changes on the skin mechanics and hydration can be seen clearly.

Table 4.3: t-Test found in the WRaP test – SCH

Paired t-Test	Control	Water	Razor	Plaster
p-value	0.0433	$<$0.0001	0.0950	$<$0.0001
p-value summary	***	***	ns	***
Significantly different (P $<$0.05)?	Yes	Yes	No	Yes

Table 4.4: Averages found in the WRaP test

	Control		Water		Razor		Plaster	
	BL	T	BL	T	BL	Treated	BL	T
SCH	37.38	39.98	37.80	69.75	38.65	36.15	37.97	46.08
AMI	3.013	2.796	2.595	3.977	2.807	2.866	2.743	3.106

4.2.4 Study conclusion

In this section, treatments were proposed to be detected by both SAMIS and corneometer. Despite the fact that the application of the water was fast, lasting only some seconds, it was the most recognizable of the treatments. It suggests that the SC has a fast capacity of absorbing moisture, and it reinforces the fact that it changes skin mechanics. The effect of shaving the area went unseen for both measurements, indicating that it may not have insulted skin. Maybe because of the location chosen, the forearm, although an easy assessed site, was not affected by the razor. Whereas most studies on shaving focus on sensitive parts of the skin (face and neck), where inflammation effects are more susceptible. As for the 4 hour generated microclimate generated with the plaster use, the SCH measures showed that moisture was created, but in a small amount, that did not change the AMI on the site.

4.3 Case Study: skin insulting with mechanical loading and tape-stripping

Insulting healthy skin is a typical manner to simulate damaged skin. For that purpose, mechanical or chemical treatments can be imposed to the skin, and the study of the parameters before and after these treatments are an indication of the skin behaviour under damage.

Because the main cause of PU is pressure over bony prominences, some studies on loading skin and evaluating its state after the insult can be found, such as the research made in [33], where rat models were tested *in-vivo*. On the study, magnets pressed skin for 1 to 3 hours, to provoke PU (Figure 4.10). Then, tests were performed to evaluate the device they propose for PU detection. The device consists of a multiplexed electrode array, in a flexible and rigid version, aimed to map tissue electrical impedance.

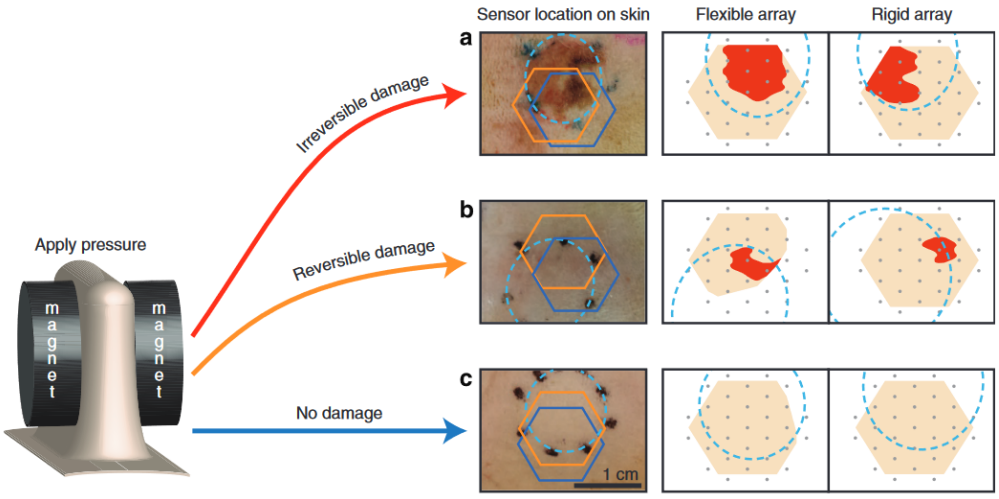

Figure 4.10: Magnets load, used to create a PU model on rats *in-vivo*. (a) Irreversible PU resulting from the loading, detected by both eye and devices assessment (b) Reversible PU with no visible trace, but detected by the devices (c) No damage detected. In the photos, dashed light blue circles indicate where the pressure was applied to the skin, orange, and dark blue hexagons indicate the location of the flexible and rigid arrays on the wound, respectively, and grey dots represent the electrodes [33]

Although this approach is very interesting, this type of test cannot be performed on human volunteers; since PU is a wound that is difficult to heal, we could not do such an insult that could impact for a long time the skin integrity of our participants or, even, provoke irreversible damage.

Therefore, a common insult to the skin to stimulate and test inflammation is tape-stripping. The inflammation caused by this insult is temporary and easier to recover than a real PU. In [34], a 20 tape-stripping insult was performed on skin and measured every 5 strips. Using an UTM-2 tribology device, the elastic modulus of the skin and its friction coefficient were measured, and with a tewameter, the TEWL values were collected. Their results show a variation in all three parameters for each step of data collection (Figure 4.11). The reduction on the elastic modulus suggests a removal of the SC to a point where there is no SC layer left, and the parts of the skin assessed are the soft under layers. This removal also results in an increase of the TEWL and friction coefficient, as the barrier functions of skin are damaged without the outmost layers, increasing the water content of the surface and varying the friction interaction.

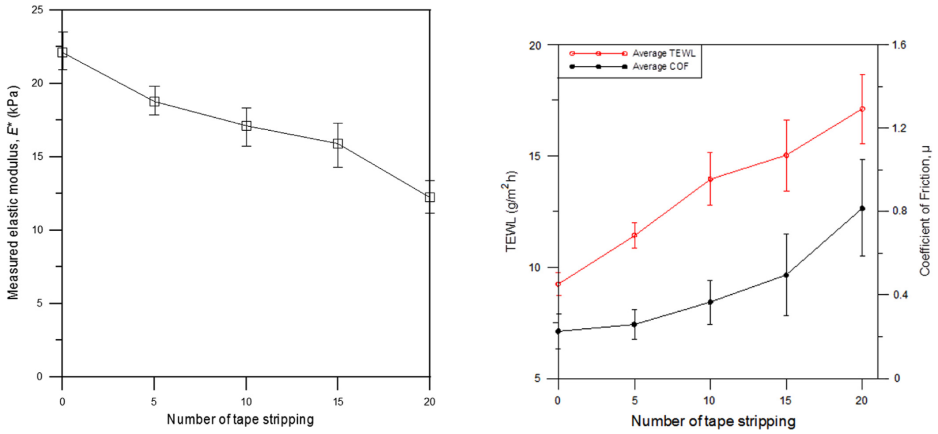

Figure 4.11: Variation of measured elastic modulus, average TEWL value and average friction coefficient with number of tape-stripping [34]

The study presented in this section was led in collaboration with the University of Southampton, UK, a partner from STINTS project. Their team have previous experiences with both mechanical loading and tape-stripping insulting. In [99], in order to simulate damage to skin mimicking a PU, they applied these insults and, in addition, over hydration and chemical irritation, to evaluate the skin state by TEWL, Sub-epidermal Moisture (SEM) and blood flow response, assessed with the tewameter, SEM scanner and laser Doppler imaging, respectively. From this study, the mechanical loading was not detected by any of the measurements, while the tape-stripping, over hydration, and chemical irritation, highly affected the TEWL values.

In our collaboration, the main steps and objectives were:

- Recruit healthy participants and test the skin in 2 zones (forearm and lower back) and compare the results given by the SAMIS, the Tewameter® and the Corneometer®
- Insult skin and check the measurements values for baseline and right after the insults
- Crossing data of measurements from SAMIS with TEWL and SCH

4.3.1 Protocol

The tests were made in 2 different body sites: the forearm and the back. The measurements included the SCH using the Corneometer®, the TEWL, using the Tewameter®, both devices from Courage + Khazaka, and finally the AMI, from the SAMIS.

The protocol for the forearm tests, summarised on Figure 4.12, included 2 insults: intermittent loading, using a metal cylinder of 1.5 kg and an 3D printed hollowed disk as interface between the cylinder and the skin, and tape-stripping, using 20 bands of Sellotape®. The set-up for the forearm measurements was the same as in Figure 3.8.

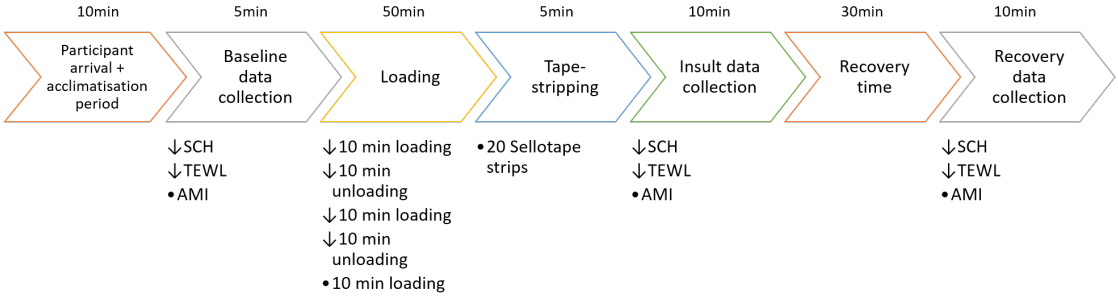

Figure 4.12: Protocol for the insults testing

First, with the arrival of the participant, the consent letter was signed, all the 3 sites (insulting and control) were cleaned, and we had a 5-minutes wait, so the participant was accustomed to the room temperature. Then, the baseline measurements started on the 3 sites, and the order of measurement was: SCH, TEWL, and AMI. Thereafter, the loading cylinder was placed and the timer started. After 3 loading and 2 unloading cycles (set-up as in Figure 4.13), the measurements of insult on the loading site were taken. The tape-stripping insult was made, followed by the insult data collection on the site and on the control. A timer for 30 minutes

of recovery was set, and after that, the recovery measurements took place. This step is an interesting regard on how skin reacts during a recovery time.

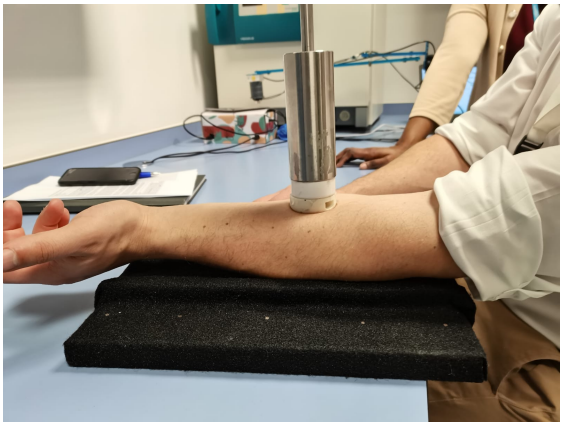

Figure 4.13: Set-up for the forearm intermittent loading – the black support for the arm was also used during the measurements

On the lower back, one insult was added to the protocol: a continuous loading, using an identical cylinder as the one used for intermittent loading (Figure 4.14), applied during 45 minutes. This insult was not included on the forearm because in this site, it is difficult for the participants to bear such a long period with this load.

For the lower back assessment, the participant was lied in prone position (Figure 4.14), so we could assess the sites. The protocol followed the description in Figure 4.12, but with the addition of the continuous loading, happening at the same time as the intermittent loading. In Figure 4.15, the visible effect of the 3 insults is highlighted for 1 participant. It is noticeable that the shape of the loading insult is a ring; the measurements were made where the contact with the skin was made, i.e. over the ring.

4.3.2 Cohort of participants

These tests had 16 volunteers, 8 were tested on the forearm and 14 on the lower back. From these, 6 had results on both sites.

The forearm cohort was composed by 5 females and 3 males, with an age range of 27 to 41 years old (34 average) and BMI ranging from 17.1 to 29.1 kg/m^2 (23.5 average).



Figure 4.14: Loads used for the loading insult and set-up for SAMIS measurements

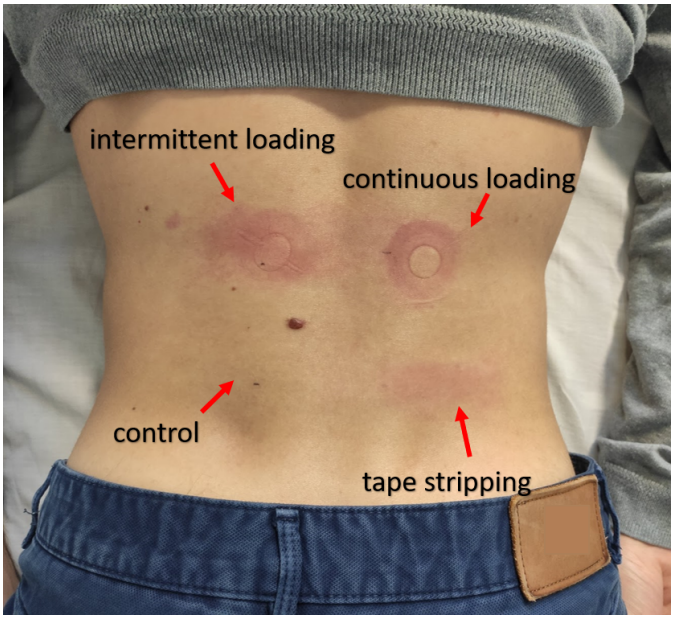

Figure 4.15: Insults to the lower back, delineating the inflammation marks

For the lower back, the cohort was composed by 6 females and 8 males, with an age range of 18 to 41 years old (32 average) and BMI ranging from 20.8 to 34.8 kg/m^2 (24.9 average).

The procedure for the tests were included in the ethics report of the University of Southampton, with the ethics No.: 9349.A6.

4.3.3 Results and discussion

Forearm

To express the impact of each insult on the parameters measured, we ran one-way Analysis of Variance (ANOVA) with the baseline, insult, and recovery results. This test is the equivalent of the t-test presented before, but convenient for 3-data sample situation. The parameters measured had different p-values, but for control and intermittent loading, all results reveal no statistical variation (p-value $>$ 0.05). The tape-stripping, however, was detected by all 3 measures, as it is summarised in Table 4.5.

Table 4.5: One-way ANOVA forearm

p-value	AMI	SCH	TEWL
Control	0.3426	0.0896	0.7420
Intermittent loading	0.3136	0.7507	0.3789
Tape-stripping	0.0077	$<$0.0001	0.0022

Using the data from the control, in the baseline take, correlation factors were used to relate the AMI to SCH, and TEWL. The results are depicted in Figure 4.16.

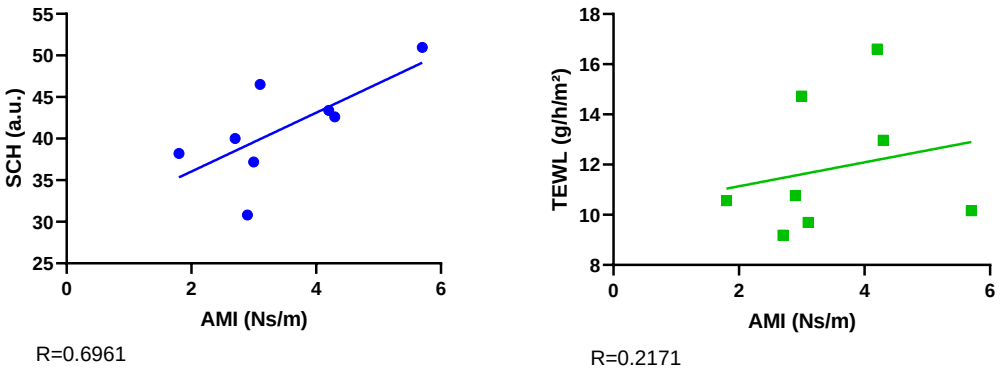

Figure 4.16: Correlation plots and respective R values, on the forearm

As well as the results presented in chapter 3, a good correlation (> 0.5) was found for the SCH results and the AMI, while the R value of correlation with the TEWL values revolves 0.2171.

A box-plot of the results of SCH is depicted in Figure 4.17. From the figure, the variation of results on tape-stripping is visible. This variation on the tape-stripping was expected, as we remove and insult the outmost layers of skin, the region measured by the corneometer.

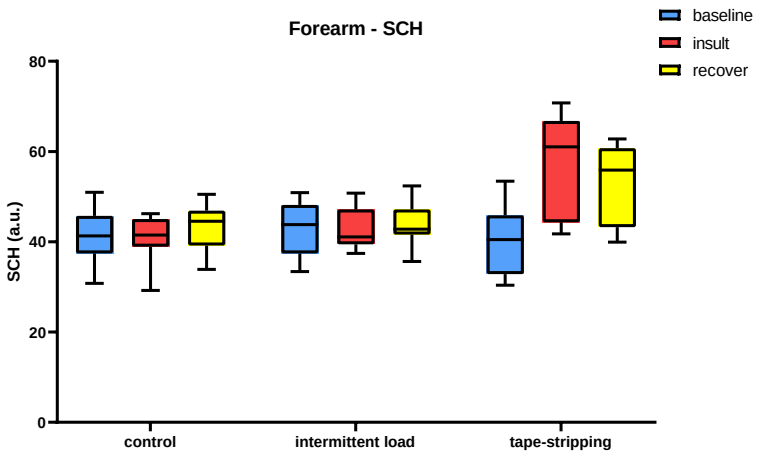

Figure 4.17: Box plot of SCH results for the control and 2 insults on the forearm, before the insults, right after insulting and after a 30-minutes recovery time

Figure 4.18 shows the values of TEWL for each insult. The values of tape-stripping change largely, as this insult affects directly the SC, the layer of the skin directly responsible for the barrier function, as presented in Figure 4.11.

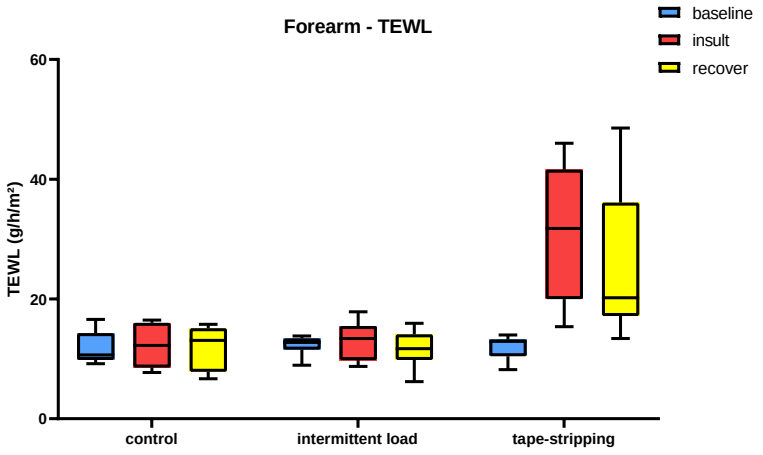

Figure 4.18: Box plot of TEWL results for the control and 2 insults on the forearm, before the insults, right after insulting and after a 30-minutes recovery time

The results of AMI for the control and 2 insults on the forearm are shown in Figure 4.19. Such as the TEWL, the effect of tape-stripping is critical. One explanation is that our device reaches only the outmost layers, affected by the tape-stripping insult.

A curious consideration on the AMI variation is the behaviour of the measure on the tape-stripping case: the values increase due to the insult. The removal of SC layers would uncover the softer tissues, and, supposing we would measure the tissues under the SC, a decrease could be expected, as shown in Figure 4.11. However, the inflammation of skin result in vasodilation of the blood vessels within the dermis, which might affect the measurements [161], due to the high blood flow on the measured site. Another hypothesis is that this behaviour is a result of the nature of our measurements, that are more related to the viscosity than the elasticity of the tissue, as it was shown in equation (3.10).

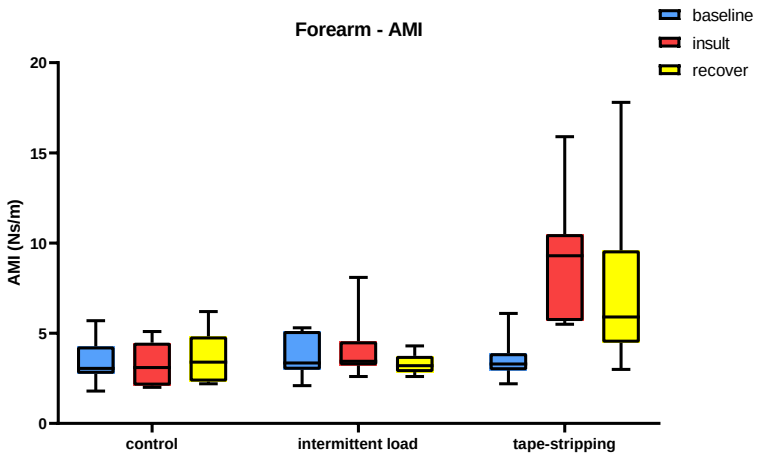

Figure 4.19: Box plot of AMI results for the control and 2 insults on the forearm, before the insults, right after insulting and after a 30-minutes recovery time

The intermittent loading performed did not induce a visible variation in the results of any measurements. This can be a result of a short duration of the insult, that does not cause any inflammation on the skin or, if it does, it is more noticeable on the underlaying tissues, that are out of reach for the tools used to measure the skin.

Lower back

As it was made for the forearm results, one-way ANOVAs were made with the baseline, insult, and recovery results for all 4 insults. Once again, the p-values for tape-stripping showed statistical variation for the 3 parameters measured. As for the control and intermittent loading, the p-value remained lower than 0.05, revealing no statistical variation. The continuous loading, however, seemed detected by the TEWL. This effect can be a result of heat generation due to the smothering of the skin for a long time on the site measured.

Table 4.6: One-way ANOVA lower back

p-value	AMI	SCH	TEWL
Control	0.1981	0.6661	0.6985
Continuous loading	0.0973	0.2638	0.0006
Intermittent loading	0.5222	0.5944	0.171
Tape-stripping	$<$0.0001	0.0032	$<$0.0001

Linear regressions were made to correlate the AMI to the SCH and TEWL. In Figure 4.20, the correlations for the lower back are presented, with the R values. In this site, we found weaker relationships for both parameters, when comparing to the forearm. The skin in this site is quite thicker than on the forearm, which can explain a change in this behaviour. Yet, no strong hypothesis was found for this change.

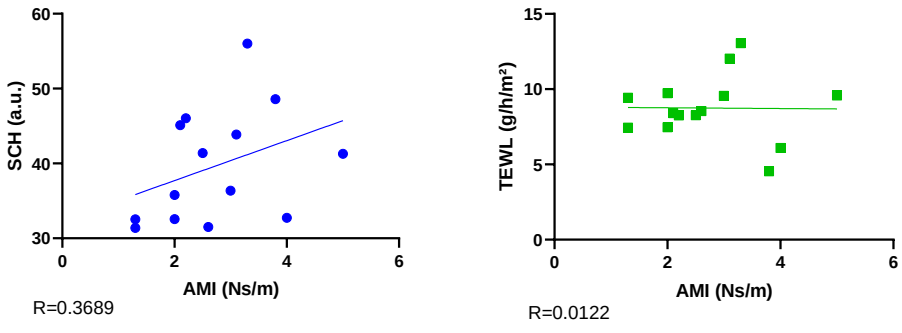

Figure 4.20: Correlation plots and respective R values, on the lower back

As presented for the forearm results, a box-plot of the results of SCH was made, depicted in Figure 4.21. Although smaller than the forearm, a variation of results on tape-stripping is visible. The results of continuous loading, the additional insult, show a variation as low as the control and intermittent loading.

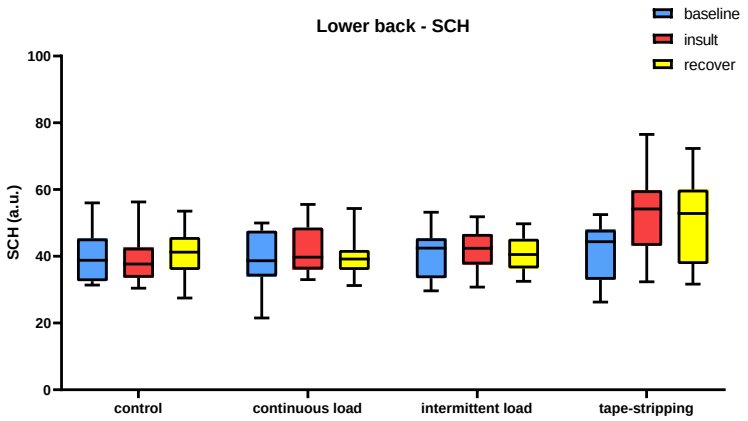

Figure 4.21: Box plot of SCH results for the control and 3 insults on the lower back, before the insults, right after insulting and after a 30-minutes recovery time

In the Figure 4.22, we present the values of TEWL for each insult. The inter-participant variation for control, intermittent and continuous loading is quite low in this site, with standard deviations ranging from 1.77 to 7.86 g/h/m^2, while in tape-stripping it revolves around 18.94 g/h/m^2, showing that each participant responded very differently to this latter insult.

Regarding the results of AMI, presented in the Figure 4.23, the standard deviation inter-participants if very high (between 1.047 and 2.71 Ns/m). In this site, it was difficult to take the measures, as it was impossible to keep the indentation force constant during all the examination. This issue was caused by the natural movement of the upper body when the person breathes. Nonetheless, a variation of the tape-stripping results is visible.

Comparing forearm and lower back results

As mentioned in the subsection 4.3.2, 6 volunteers participated in both experiments, having their forearm and lower back assessed. Then, we took this opportunity to compare the results of AMI on both sites was made (Figure 4.24).

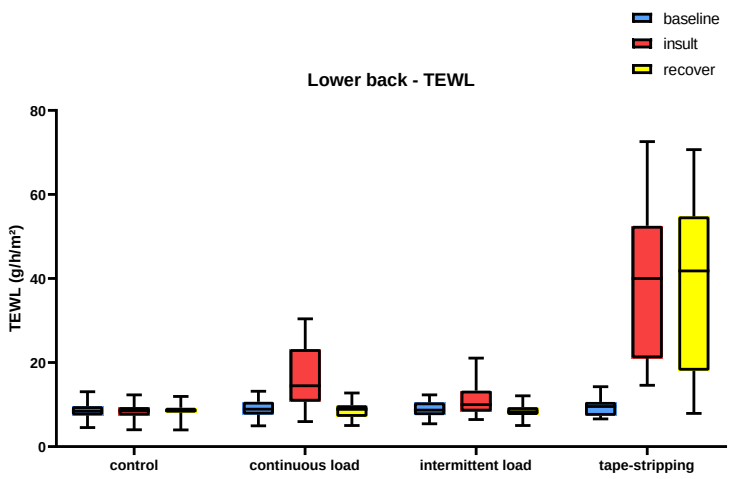

Figure 4.22: Box plot of TEWL results for the control and 3 insults on the lower back, before the insults, right after insulting and after a 30-minutes recovery time

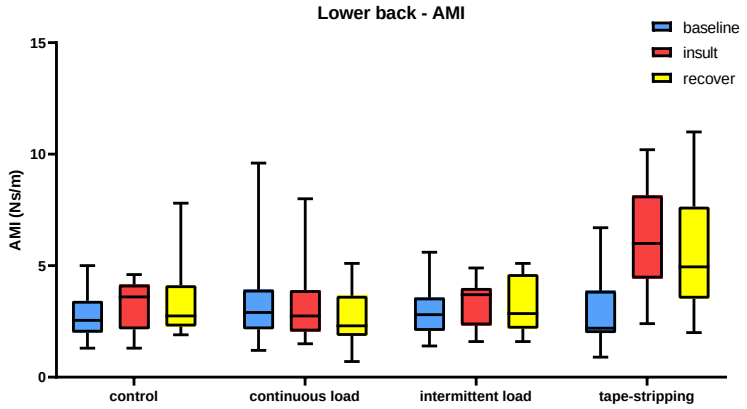

Figure 4.23: Box plot of AMI results for the control and 3 insults on the lower back, before the insults, right after insulting and after a 30-minutes recovery time

After running a t-test (p-value=0.332), it seems that, although the skin of the 2 sites are non-glabrous, SAMIS can still detect the difference between them. The number of participants is quite low, but the results are mostly positive and further tests can be proposed to confirm it. However, these results confirm the ones already obtained in chapter 3, comparing the palm and the forearm.

Another analysis proposed to compare these sites was to evaluate the levels of AMI after insult and recovery (Figure 4.25). This investigation was made only for the tape-stripping, since

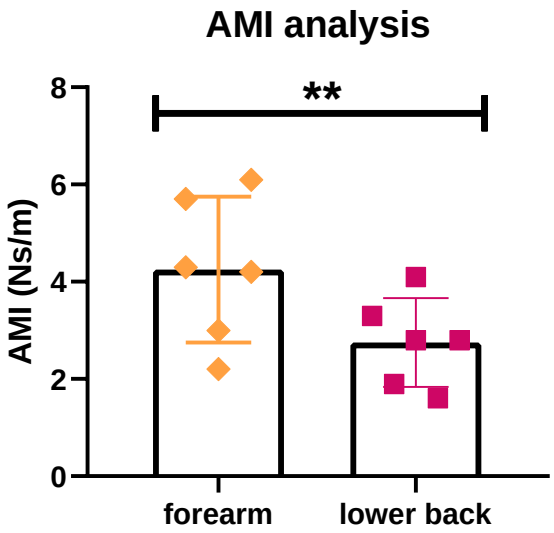

p-value = 0.332

Figure 4.24: Results comparing AMI on the forearm and lower back (baseline sites), with p-value to show that the SAMIS can distinguish the 2 sites

it was previously presented as the inflammation detected by our device.

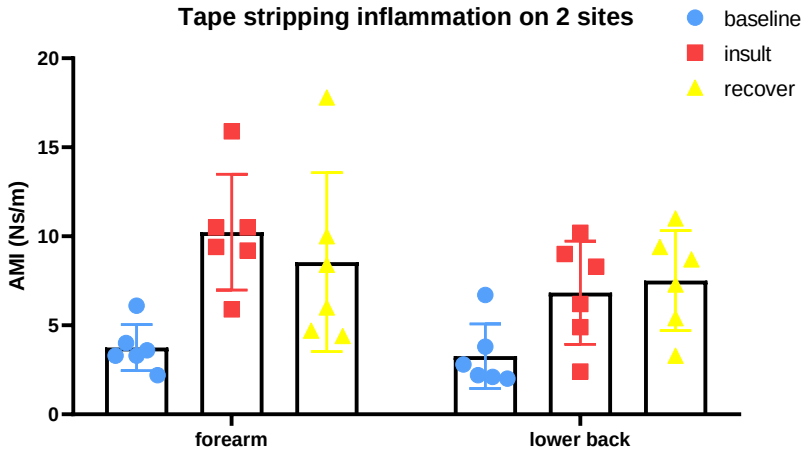

Figure 4.25: Effect of inflammation with tape-stripping on the forearm and lower back: baseline, insult and recover

Looking into the forearm results, the standard deviation from baseline to insult ranges from

2.19 to 8.42 Ns/m, while for the lower back the range is 0.14 to 4.25 Ns/m. It seems, from these results, that in the forearm, the inflammation is more latent than in the lower back. Regarding, the analysis of the recovery effect, comparing insult and recover data, the forearm shows a faster recovery than the lower back, with standard deviation ranging from 0.35 to 4.313 Ns/m, while on the lower back it goes from 0.57 to 2.12 Ns/m.

4.3.4 Study conclusion

In this section, a study performed in partnership with the University of Southampton was presented. The study consisted in insulting the skin with mechanical loading and tape-stripping, and measurements with the SAMIS, corneometer, and tewameter were proposed to detect these insults. The tests were divided in two sites: the forearm and the lower back.

For both sites, the only insult detected by the measurements proposed was the tape-stripping, maybe because it causes inflammation on the SC, the external layer that is measured by the corneometer, tewameter, and the SAMIS.

The comparison of the results of forearm and lower back has shown that the measurements are also capable of distinguishing the 2 sites by the mechanical properties.

4.4 Chapter conclusions

This chapter presents the experimental results for the tests using the SAMIS. The data collected reinforced the reliability of the device to distinguish skin mechanical parameters within the same body, on 2 sites; in particular, it was shown that the SAMIS can distinguish two skin sites while the SCH is not capable of, as it was presented in Figures 4.3 and 4.4. The same site (the forearm), was studied under a change of hydration conditions; or after submitted to insults.

Data from other devices were compared with the AMI, showing a linear relationship between AMI and SCH, and an apparent weak correlation between AMI and TEWL.

It seems, from experimental results, that the SAMIS is capable of properly measuring mechanical properties or SC. More tests can be proposed to confirm it and strengthen this hypothesis, hopefully using the device on at-risk sites on patients that are vulnerable to PU incidence.

Therefore, in this chapter, we solved the challenge 3: relating the acoustical mechanical impedance measured to skin characteristics and integrity.

Chapter 5

Conclusions and Perspectives

5.1 General Conclusions

The work presented in this thesis is part of the STINTS project, and was developed to propose a device to evaluate the skin integrity, especially in the context of PU, by means of acoustical mechanical impedance. Considering the aetiology of PU and all the changes of the skin due to these wounds, it seems fair to use the AMI as a clue for early stage PU diagnosis. Having a follow-up of skin parameters since the arrival of a patient at the ICU, or measurements on a regular basis on people with low mobility is essential to prevent skin failure. The SAMIS can be part of the healthcare staff toolbox for daily check-ups on at-risk sites.

The first chapter explained the CW, particularly PU, in detail, including the aetiology, effects on patients and the healthcare system, as well as current diagnostic methods. The methods for creating ultrasounds using PE are listed, with an emphasis on the LFU and its uses in CW context.

The mechanical characteristics of the skin were discussed, since they are the key that our study addressed. The structure of the skin layers and mechanical skin models were presented, with an emphasis on the SC. The project highlighted the dynamic mechanical testing employing LFU at 60 kHz and linked them to TEWL and SCH, ultimately relating to skin integrity. The use of LFU on the early detection of PU has several benefits, including being simple to administer,

reaching the outermost layers of the skin, where PU typically begins, and being a non-invasive and gentle stimulation, which is crucial when examining an already fragile tissue.

Chapter 2 introduced the LT and defined its mechanical and electrical details. In order to understand the non-linearities of the PE and the vibration behaviour of the device under various circumstances, the electrical and electromechanical models of this device were presented.

The device's architecture was explained, along with the subsystems that had been separated for easier comprehension of the SAMIS's design and operations. For the LT to be excited, the first component—the low-frequency ultrasonic production subsystem—was required. The second, conditioners and sensors, are crucial to guarantee the device's identification, control, and subsequent proper operation. Finally, we discussed the normal force control, a component created to improve the SAMIS's usability and dependability as a medical instrument.

A controlled vibration is essential to the probe's operation. Then, chapter 2 also presented the model identification and controller design. The mass-spring-damper model, which is well-known in literature, was employed. The parameters of the device were exhibited and determined using the rotating reference frame, a practical way to describe and control a PE structure. The system follows a first order equation; hence PI was the ideal fit when designing a controller using the vector control method. The design of the device resulted on a reliable and safe tool, still requiring some improvements to make it portable, yet assuring a robust measure.

In chapter 3, we discussed the methods for measurements with the SAMIS, including measurements with and without any load. To validate the measurement, the initial experiments utilizing phantom skin were reported.

Before implementing the prototype as it is today, many attempts were made to evaluate which LT probe was more consistent, the need of an interface between the device and the skin, and how the normal force could interfere to the results. The application of the same normal force is a crucial component for the accuracy of the SAMIS tests. Considering the experiments reported, the force used was 0.2 N.

The insertion of a matching layer between the SAMIS and the skin was the final experiment to establish the methodology. It was discovered that creamy and liquid materials severely distorted the findings. The device's metal body was then covered with a sheet of PLC, a hydrophobic substance that reduces the variability of the measurements.

After these efforts were made to conceive the current device, and once it was applicable for simple tests, we could evaluate its reliability, by testing the inter and intra-participants variations with different takes. Then, a relationship could be traced with other skin parameters, SCH and TEWL. Tests were performed to build a data set of healthy skin characteristics

Finally, in chapter 4, the experimental findings for the SAMIS tests were presented. The data gathered confirmed the accuracy of the device in differentiating skin mechanical parameters between two sites on the same body, between the same site and different hydration levels, or between the same site before and after insults.

The experimental results of the first case study show that, despite the linear relationship discovered in the SCH assessment, the SAMIS values were able to analyse the skin in several areas, while the SCH was not so accurate for this matter.

In the second case study, where treatments were suggested to be identified in this part by SAMIS and Corneometer®, the water treatment was the most recognizable, even though it was applied quickly and only lasted a few seconds. It underlines the fact that the skin mechanics change, when the SC is submitted to moisture, and suggests that it has a quick capacity for absorbing moisture. The measurements did not reveal any shaving-related effects, suggesting that the skin may not have been harmed. In this study, it was found that the razor had no effect on the forearm. For the 4-hour-generated microclimate, the SCH measurements revealed that moisture was produced, but only in a little scale, which had no effect on the AMI measured on this site.

The third case study presented was conducted in collaboration with the University of Southampton. In order to detect skin insults, measurements with the SAMIS, Corneometer®, and Tewameter® were suggested. The investigation used mechanically loading and tape-stripping to inflict insults. The forearm and lower back were the two locations for the examinations.

The tape-stripping, which induces inflammation on the SC, the exterior layer that is measured by the Corneometer®, Tewameter®, and the SAMIS, was the sole insult discovered by the measurements suggested for both sites.

The comparison of the forearm and lower back results has demonstrated that the measurements performed with the SAMIS can also distinguish between the two sites based on their mechanical characteristics.

From the results presented, the SAMIS seems to be a promising novel device worth more investigation for PU diagnosis. This work is a milestone of a device that can contribute to skin mechanics study. To reach the diagnosis stage, some perspectives are envisaged, as presented in the next section.

5.2 Perspectives

The perspectives of this research include enhancements on the device's design, such as a holding case that allows a consistent indentation force without the tripod, resulting on a handheld probe, and a smaller and integrated system, with a normal force sensor that can collect the data on the same microcontroller as the LT.

For the device's design, the effect of the frequency of the probe can also be revisited. With more time, tests with each of them could present a better characterisation of skin behaviour under different vibrating frequencies.

It would be also interesting to test a wider and more variable group of participants, so it would be possible to cluster the results by age, gender, BMI and so on. Performing these tests on the PU common sites of the participants, such as the sacrum and the heels, is another perspective, as we can collect a dataset of the healthy skin in these sites.

Another suggestion, concerning the use of SAMIS on damaged skin, to validate the device for its real objective: diagnosing early stage PU. For that, several efforts are to be made, in order to have a CE marked device, safe for healthcare use.

The use of SAMIS can be combined, for instance, with the application of a skin care (e.g. cream-based treatments but also wound management such as debridement) as a follow-up instrument to measure the evolution of a treatment. More broadly, it is a tool to qualify the skin: you could use it to see if a treatment gradually improves the quality of the skin or makes it regain the same characteristics as a healthy area while treating it.

Another goal that could be tackled with the SAMIS is the implementation of LFU mechanical stimulation therapy. As presented in chapter 1, this can be a manner to prevent and treat PU, and the small displacements of the device can produce a tender massage effect, maybe stimulating tissue angiogenesis.

Summarising it, an extent of this research could:

- To consider and study the non-linearities of the LT and its impact on our measurement
- To investigate if 0.2 N is the appropriate indentation force, or if 60 kHz is the best frequency to study the SC mechanics
- To propose an alternative model of the skin
- To remove SCH influence from the measurement of AMI
- To test it on patients at-risk of PU and indeed characterise real damaged skin AMI
- To study the effects of our LFU in a treatment of incipient PU
- To provide a portable probe

Appendix A

Appendix I

A.1 Cohort for Palm - Forearm test

Here is the full list of participants for the Palm - Forearm tests. Note: P5 has a hairy forearm.

Table A.1: Participant data for the Palm-Forearm test

P	Gender	Age	BMI
1	F	28	20.96
2	M	24	21.97
3	M	30	21.04
4	M	30	30.86
5	M	50	24.97
6	F	29	24.27
7	F	33	24.24
8	M	30	38.87
9	F	27	22.49
10	F	58	23.23
11	F	23	18.61
12	M	33	22.41
13	F	28	19.03
14	M	28	22.34
15	M	42	21.97
16	F	26	20.70
17	F	27	21.50
18	M	29	21.60
19	M	31	24.49
20	F	26	21.30

A.2 Cohort for WRaP test

Here is the full list of participants for the WRaP tests.

Table A.2: Participant data for the WRaP test

P	Gender	Age	BMI
1	M	31	23.08
2	M	24	21.97
3	F	28	20.96
4	F	29	17.94
5	M	28	22.34
6	M	30	25.01
7	M	30	38.87
8	F	29	22.23
9	F	34	19.14
10	M	33	23.46
11	F	31	23.44
12	F	30	21.26
13	M	34	22.06
14	F	33	24.24
15	M	42	21.97
16	F	26	20.70
17	F	30	23.88
18	M	29	21.60
19	M	31	21.71
20	M	26	24.49

A.3 Cohort for Soton test

Here is the full list of participants for the insulting tests. The superscripts F and B stand for the site tested, forearm and back, respectively.

Table A.3: Participant data for insulting tests

P	Gender	Age	BMI	Ethnicity
1^{FB}	M	37	25.73	asian-indian
2^{FB}	F	30	24.34	asian-indian
3^{F}	F	40	17.10	asian
4^{FB}	F	29	21.53	latin-american
5^{F}	F	33	21.97	white caucasian
6^{B}	M	32	23.24	black
7^{B}	M	37	34.77	white
8^{B}	F	31	22.58	african caucasian
9^{B}	F	35	25.80	black
10^{B}	M	40	22.23	black
11^{FB}	M	36	29.10	white
12^{B}	F	18	22.06	white
13^{B}	M	25	26.85	white
14^{B}	M	27	22.45	white caucasian
15^{FB}	M	41	27.46	white british
16^{FB}	F	27	20.83	asian

Bibliography

[1] Kentcht, “Pressure ulcer prevention,” *Kent Community Health NHS Foundation Trust*, 2022.

[2] A. Gefen, D. M. Brienza, J. Cuddigan, E. Haesler, and J. Kottner, “Our contemporary understanding of the aetiology of pressure ulcers/pressure injuries,” *International Wound Journal*, vol. 19, no. 3, pp. 692–704, 2022.

[3] A. Arnold, “Pressure Ulcers & Bedsores: Nursing Home Negligence Lawyer,” *Greenville Nursing Home Abuse & Neglect Guide*, 2016.

[4] S. E. Gardner, R. A. Frantz, S. Bergquist, and C. D. Shin, “A prospective study of the pressure ulcer scale for healing (push),” *The Journals of Gerontology Series A: Biological Sciences and Medical Sciences*, vol. 60, no. 1, pp. 93–97, 2005.

[5] N. Bergstrom, P. J. Demuth, and B. J. Braden, “A clinical trial of the braden scale for predicting pressure sore risk,” *Nursing Clinics of North America*, vol. 22, no. 2, pp. 417–428, 1987.

[6] D. Park, H. Park, J. Seo, and S. Lee, “Sonophoresis in transdermal drug deliverys,” *Ultrasonics*, vol. 54, no. 1, pp. 56–65, 2014.

[7] W. Maurel, D. Thalmann, Y. Wu, and N. M. Thalmann, *Biomechanical models for soft tissue simulation*, vol. 48. Springer, 1998.

[8] P. Agache and P. Humbert, *Measuring the Skin*. Springer Science & Business Media, July 2004. Google-Books-ID: APiLX8aBakkC.

[9] R. Lundström, "Local vibrations—Mechanical impedance of the human hand's glabrous skin," *Journal of Biomechanics*, vol. 17, pp. 137–144, Jan. 1984.

[10] Y. Yuan and R. Verma, "Measuring microelastic properties of stratum corneum," *Colloids and Surfaces B: Biointerfaces*, vol. 48, no. 1, pp. 6–12, 2006.

[11] H. M. Deda, "Ceramide Analysis in Moisturizer Research - Ceramide Analysis of the Stratum Corneum," 2020.

[12] R. H. Wildnauer, J. W. Bothwell, and A. B. Douglass, "Stratum Corneum Biomechanical Properties I. Influence of Relative Humidity on Normal and Extracted Human Stratum Corneum," *Journal of Investigative Dermatology*, vol. 56, pp. 72–78, Jan. 1971.

[13] A. Park, "Rheology of stratum corneum-i: A molecular interpretation of the stress-strain curve," *J. Soc. Cosmet. Chem.*, vol. 23, pp. 3–12, 1972.

[14] Y. S. Papir, K.-H. Hsu, and R. H. Wildnauer, "The mechanical properties of stratum corneum: I. The effect of water and ambient temperature on the tensile properties of newborn rat stratum corneum," *Biochimica et Biophysica Acta (BBA) - General Subjects*, vol. 399, pp. 170–180, July 1975.

[15] K. S. Koutroupi and J. C. Barbenel, "Mechanical and failure behaviour of the stratum corneum," *Journal of Biomechanics*, vol. 23, pp. 281–287, Jan. 1990.

[16] M. Geerligs, *Skin layer mechanics*. Phd Thesis 1 (Research TU/e / Graduation TU/e), Technische Universiteit Eindhoven, Eindhoven, 2010. ISBN: 9789074445924.

[17] P. Chaturvedi, P. R. Worsley, G. Zanelli, W. Kroon, and D. L. Bader, "Quantifying skin sensitivity caused by mechanical insults: A review," *Skin Research and Technology*, vol. 28, no. 1, pp. 187–199, 2022.

[18] W. D. Meador, G. P. Sugerman, H. M. Story, A. W. Seifert, M. R. Bersi, A. B. Tepole, and M. K. Rausch, "The regional-dependent biaxial behavior of young and aged mouse skin: A detailed histomechanical characterization, residual strain analysis, and constitutive model," *Acta biomaterialia*, vol. 101, pp. 403–413, 2020.

[19] C. Pailler-Mattei, S. Bec, and H. Zahouani, "In vivo measurements of the elastic mechanical properties of human skin by indentation tests," *Medical engineering & physics*, vol. 30, no. 5, pp. 599–606, 2008.

[20] B. Finlay, "Dynamic mechanical testing of human skin 'in vivo'," *Journal of biomechanics*, vol. 3, no. 6, pp. 557–568, 1970.

[21] H. Alexander and T. Cook, "Accounting for natural tension in the mechanical testing of human skin," *Journal of Investigative Dermatology*, vol. 69, no. 3, pp. 310–314, 1977.

[22] S. Diridollou, F. Patat, F. Gens, L. Vaillant, D. Black, J. Lagarde, Y. Gall, and M. Berson, "In vivo model of the mechanical properties of the human skin under suction," *Skin Research and technology*, vol. 6, no. 4, pp. 214–221, 2000.

[23] A. Kaci, A. Torres, F. Giraud, C. Giraud-Audine, M. Amberg, and B. Lemaire-Semail, "Fundamental acoustical finger force calculation for out-of-plane ultrasonic vibration and its correlation with friction reduction," in *2019 IEEE World Haptics Conference (WHC)*, pp. 413–418, IEEE, 2019.

[24] E. Vezzoli, Z. Vidrih, V. Giamundo, B. Lemaire-Semail, F. Giraud, T. Rodic, D. Peric, and M. Adams, "Friction reduction through ultrasonic vibration part 1: Modelling intermittent contact," *IEEE Transactions on Haptics*, vol. 10, no. 2, pp. 196–207, 2017.

[25] N. Huloux, L. Willemet, and M. Wiertlewski, "How to Measure the Area of Real Contact of Skin on Glass," *IEEE Transactions on Haptics*, vol. 14, pp. 235–241, Apr. 2021. Conference Name: IEEE Transactions on Haptics.

[26] W. Mason, "An Electromechanical Representation of a Piezoelectric Crystal Used as a Transducer," *Proceedings of the Institute of Radio Engineers*, vol. 23, pp. 1252–1263, Oct. 1935. Conference Name: Proceedings of the Institute of Radio Engineers.

[27] L. K. Sienkiewicz, *Concept, implementation and analysis of the piezoelectric resonant sensor/actuator for measuring the aging process of human skin*. PhD thesis, Toulouse, INPT, 2016.

[28] D. Guyomar, B. Ducharne, and G. Sebald, “High nonlinearities in langevin transducer: A comprehensive model,” *Ultrasonics*, vol. 51, no. 8, pp. 1006–1013, 2011.

[29] C. K. electronic GmbH, “Brochure of corneometer® CM 825,” 2022.

[30] C. K. electronic GmbH, “Brochure of tewameter® tmhex,” 2022.

[31] A. Chanda, “Biomechanical modeling of human skin tissue surrogates,” *Biomimetics*, vol. 3, no. 3, p. 18, 2018.

[32] R. O. Potts, D. A. Chrisman Jr, and E. M. Buras Jr, “The dynamic mechanical properties of human skin in vivo,” *Journal of biomechanics*, vol. 16, no. 6, pp. 365–372, 1983. Publisher: Elsevier.

[33] S. L. Swisher, M. C. Lin, A. Liao, E. J. Leeflang, Y. Khan, F. J. Pavinatto, K. Mann, A. Naujokas, D. Young, S. Roy, *et al.*, “Impedance sensing device enables early detection of pressure ulcers in vivo,” *Nature communications*, vol. 6, no. 1, p. 6575, 2015.

[34] C.-Y. Chen, C.-A. Yu, T.-F. Hong, Y.-L. Chung, and W.-L. Li, “Contact and frictional properties of stratum corneum of human skin,” *Biosurface and Biotribology*, vol. 1, no. 1, pp. 62–70, 2015.

[35] C. Suggs and C. Abrams Jr, “Mechanical impedance techniques for evaluating the dynamic characteristics of biological materials,” *Journal of Agricultural Engineering Research*, vol. 16, no. 3, pp. 307–315, 1971.

[36] A. K. Dabrowska, C. Adlhart, F. Spano, G.-M. Rotaru, S. Derler, L. Zhai, N. D. Spencer, and R. M. Rossi, “*In vivo* confirmation of hydration-induced changes in human-skin thickness, roughness and interaction with the environment,” *Biointerphases*, vol. 11, no. 3, p. 031015, 2016.

[37] A. Gefen, “How do microclimate factors affect the risk for superficial pressure ulcers: A mathematical modeling study,” *Journal of Tissue Viability*, vol. 20, no. 3, pp. 81–88, 2011.

[38] J. White, N. Ivins, A. Wilkes, G. Carolan-Rees, and K. G. Harding, “Non-contact low-frequency ultrasound therapy compared with UK standard of care for venous leg ulcers:

a single-centre, assessor-blinded, randomised controlled trial: NLFU trial," *International Wound Journal*, vol. 13, no. 5, pp. 833–842, 2016.

[39] C. VanGilder, G. D. MacFarlane, S. Meyer, *et al.*, "Results of nine international pressure ulcer prevalence surveys: 1989 to 2005," *Ostomy Wound Management*, vol. 54, no. 2, p. 40, 2008.

[40] J. S. Mervis and T. J. Phillips, "Pressure ulcers: Pathophysiology, epidemiology, risk factors, and presentation," *Journal of the American Academy of Dermatology*, vol. 81, pp. 881–890, Oct. 2019.

[41] J. Whitney, L. Phillips, R. Aslam, A. Barbul, F. Gottrup, L. Gould, M. C. Robson, G. Rodeheaver, D. Thomas, and N. Stotts, "Guidelines for the treatment of pressure ulcers," *Wound Repair and Regeneration*, vol. 14, no. 6, pp. 663–679, 2006.

[42] D. R. Thomas, "Are all pressure ulcers avoidable?," *Journal of the American Medical Directors Association*, vol. 4, no. 2, pp. S44–S48, 2003.

[43] E. McInnes, A. Jammali-Blasi, S. E. Bell-Syer, J. C. Dumville, V. Middleton, and N. Cullum, "Support surfaces for pressure ulcer prevention," *Cochrane database of systematic reviews*, no. 9, 2015.

[44] R. Houwing, M. Rozendaal, W. Wouters-Wesseling, J. Beulens, E. Buskens, and J. Haalboom, "A randomised, double-blind assessment of the effect of nutritional supplementation on the prevention of pressure ulcers in hip-fracture patients," *Clinical Nutrition*, vol. 22, no. 4, pp. 401–405, 2003.

[45] R. M. Schue and D. K. Langemo, "Prevalence, incidence, and prediction of pressure ulcers on a rehabilitation unit," *Journal of WOCN*, vol. 26, no. 3, pp. 121–129, 1999.

[46] R. BEADY Jr, "Relationship of quantitative wound bacterial counts to healing of decubiti: effect of topical gentamicin," *Antimicrobial Agents Chemother (Bethesda)*, vol. 10, pp. 147–155, 1964.

[47] F. Gottrup, "Oxygen in wound healing and infection," *World journal of surgery*, vol. 28, pp. 312–315, 2004.

[48] E. A. Ayello and J. E. Cuddigan, “Debridement: controlling the necrotic/cellular burden,” *Advances in skin & wound care*, vol. 17, no. 2, pp. 66–75, 2004.

[49] K. Breuing, E. Eriksson, P. Liu, and D. R. Miller, “Healing of partial thickness porcine skin wounds in a liquid environment,” *Journal of Surgical Research*, vol. 52, no. 1, pp. 50–58, 1992.

[50] D. P. Kane, “Surgical management of pressure ulcers,” *Pressure Ulcers in the Aging Population: A Guide for Clinicians*, pp. 99–126, 2014.

[51] N. A. Stotts, G. T. Rodeheaver, D. R. Thomas, R. A. Frantz, A. A. Bartolucci, C. Sussman, B. A. Ferrell, J. Cuddigan, and J. Maklebust, “An instrument to measure healing in pressure ulcers: development and validation of the pressure ulcer scale for healing (push),” *The Journals of Gerontology Series A: Biological Sciences and Medical Sciences*, vol. 56, no. 12, pp. M795–M799, 2001.

[52] A. Gefen, P. Alves, G. Ciprandi, F. Coyer, C. T. Milne, K. Ousey, N. Ohura, N. Waters, P. Worsley, J. Black, M. Barakat-Johnson, D. Beeckman, J. Fletcher, H. Kirkland-Kyhn, N. A. Lahmann, Z. Moore, Y. Payan, and A.-B. Schlüer, “Device-related pressure ulcers: SECURE prevention,” *Journal of Wound Care*, vol. 29, pp. S1–S52, 2020.

[53] Q. Wang, L. Kong, S. Sprigle, and V. Hayward, “Portable gage for pressure ulcer detection,” in *2006 International Conference of the IEEE Engineering in Medicine and Biology Society*, pp. 5997–6000, IEEE, 2006.

[54] G. M. Yarkony, “Pressure ulcers: A review,” *Archives of Physical Medicine and Rehabilitation*, vol. 75, no. 8, pp. 908–917, 1994.

[55] R. Kleinerman, T. B. Whang, R. L. Bard, and E. S. Marmur, “Ultrasound in dermatology: Principles and applications,” *Journal of the American Academy of Dermatology*, vol. 67, no. 3, pp. 478–487, 2012.

[56] T. Sashida and T. Kenjo, “Introduction to ultrasonic motors,” *The U.S. Department of Energy’s Office of Scientific and Technical Information*, 1993. Publisher: New York, NY (United States); Oxford Univ. Press.

[57] B. E. Polat, D. Blankschtein, and R. Langer, “Low-frequency sonophoresis: application to the transdermal delivery of macromolecules and hydrophilic drugs,” *Expert Opinion on Drug Delivery*, vol. 7, no. 12, pp. 1415–1432, 2010.

[58] S. Mitragotri and J. Kost, “Low-frequency sonophoresis,” *Advanced Drug Delivery Reviews*, vol. 56, no. 5, pp. 589–601, 2004.

[59] B. M. Madhok, K. Vowden, and P. Vowden, “New techniques for wound debridement,” *International Wound Journal*, vol. 10, no. 3, pp. 247–251, 2013. _eprint: https://onlinelibrary.wiley.com/doi/pdf/10.1111/iwj.12045.

[60] L. Cook, “Understanding methods of wound debridement,” *British journal of nursing (Mark Allen Publishing)*, vol. 23, pp. S10–2, S14, 2014.

[61] C. A. Murphy, P. Houghton, T. Brandys, G. Rose, and D. Bryant, “The effect of 22.5 khz low-frequency contact ultrasound debridement (lfcud) on lower extremity wound healing for a vascular surgery population: a randomised controlled trial,” *International Wound Journal*, vol. 15, no. 3, pp. 460–472, 2018.

[62] Y.-J. R. Chang, J. Perry, and K. Cross, “Low-frequency ultrasound debridement in chronic wound healing: A systematic review of current evidence,” *Plastic Surgery*, vol. 25, no. 1, pp. 21–26, 2017.

[63] A. L. Bell and J. Cavorsi, “Noncontact ultrasound therapy for adjunctive treatment of non-healing wounds: Retrospective analysis,” *Physical Therapy*, vol. 88, no. 12, pp. 1517–1524, 2008. Publisher: Oxford Academic.

[64] K. H. Breuing, L. Bayer, J. Neuwalder, and D. P. Orgill, “Early experience using low-frequency ultrasound in chronic wounds,” *Annals of Plastic Surgery*, vol. 55, no. 2, pp. 183–187, 2005.

[65] P. S. Cole, J. Quisberg, and M. M. Melin, “Adjuvant use of acoustic pressure wound therapy for treatment of chronic wounds: A retrospective analysis,” *Journal of Wound Ostomy & Continence Nursing*, vol. 36, no. 2, pp. 171–177, 2009.

[66] V. R. Driver, M. Yao, and C. J. Miller, “Noncontact low-frequency ultrasound therapy in the treatment of chronic wounds: A meta-analysis,” *Wound Repair and Regeneration*, vol. 19, no. 4, pp. 475–480, 2011. _eprint: https://onlinelibrary.wiley.com/doi/pdf/10.1111/j.1524-475X.2011.00701.x.

[67] S. J. Kavros, D. A. Liedl, A. J. Boon, J. L. Miller, J. A. Hobbs, and K. L. Andrews, “Expedited wound healing with noncontact, low-frequency ultrasound therapy in chronic wounds: A retrospective analysis,” *Advances in Skin & Wound Care*, vol. 21, no. 9, pp. 416–423, 2008.

[68] R. Thomas, “Acoustic pressure wound therapy in the treatment of stage II pressure ulcers,” *Ostomy/Wound Management*, vol. 54, no. 11, pp. 56–58, 2008.

[69] J. Voigt, M. Wendelken, V. Driver, and O. M. Alvarez, “Low-frequency ultrasound (20-40 kHz) as an adjunctive therapy for chronic wound healing: A systematic review of the literature and meta-analysis of eight randomized controlled trials,” *The International Journal of Lower Extremity Wounds*, vol. 10, no. 4, pp. 190–199, 2011. Publisher: SAGE Publications.

[70] T. Conner-Kerr and M. E. Oesterle, “Current perspectives on therapeutic ultrasound in the management of chronic wounds: a review of evidence,” *Chronic Wound Care Management and Research*, vol. Volume 4, pp. 89–98, 2017.

[71] P. M. Krishnasamy, “Ultrasound assisted wound care,” 2005.

[72] B. C. Wulff and T. A. Wilgus, “Mast cell activity in the healing wound: more than meets the eye?,” *Experimental Dermatology*, vol. 22, no. 8, pp. 507–510, 2013.

[73] R. Franco de Oliveira, D. A. A. Pires Oliveira, and C. P. Soares, “Effect of low-intensity pulsed ultrasound on l929 fibroblasts,” *Archives of Medical Science : AMS*, vol. 7, no. 2, pp. 224–229, 2011.

[74] J. Lai and M. R. Pittelkow, “Physiological effects of ultrasound mist on fibroblasts,” *International Journal of Dermatology*, vol. 46, no. 6, pp. 587–593, 2007. _eprint: https://onlinelibrary.wiley.com/doi/pdf/10.1111/j.1365-4632.2007.02914.x.

[75] W. J. Ennis, W. Valdes, M. Gainer, and P. Meneses, "Evaluation of clinical effectiveness of MIST ultrasound therapy for the healing of chronic wounds," *Advances in Skin & Wound Care*, vol. 19, no. 8, pp. 437–446, 2006.

[76] "UltraMIST®," July 2008.

[77] H. Yousef, M. Alhajj, and S. Sharma, "Anatomy, Skin (Integument), Epidermis," 2022.

[78] S. Luebberding, N. Krueger, and M. Kerscher, "Mechanical properties of human skin in vivo: a comparative evaluation in 300 men and women," *Skin research and technology*, vol. 20, pp. 127–135, May 2014.

[79] K. Langer, "On the anatomy and physiology of the skin. i. the cleavability of the cutis," *British Journal of Plastic Surgery*, vol. 31, p. 3, 1978.

[80] K. Langer, "On the anatomy and physiology of the skin: Ii. skin tension (with 1 figure)," *British Journal of Plastic Surgery*, vol. 31, no. 2, pp. 93–106, 1978.

[81] K. Langer, "On the anatomy and physiology of the skin. iii. the elasticity of the cutis," *British Journal of Plastic Surgery*, vol. 31, 1978.

[82] M. Ridge and V. Wright, "The directional effects of skin: A bio-engineering study of skin with particular reference to langer's lines," *Journal of Investigative Dermatology*, vol. 46, no. 4, pp. 341–346, 1966.

[83] M.-A. Y. Abyaneh, R. Griffith, L. Falto-Aizpurua, and K. Nouri, "Famous lines in history: Langer lines," *JAMA dermatology*, vol. 150, no. 10, pp. 1087–1087, 2014.

[84] C. Pailler-Mattei, L. Laquièze, R. Debret, S. Tupin, G. Aimond, P. Sommer, and H. Zahouani, "Rheological behaviour of reconstructed skin," *Journal of the mechanical behavior of biomedical materials*, vol. 37, pp. 251–263, 2014.

[85] H. Jayabal, N. Dingari, and B. Rai, "A linear viscoelastic model to understand skin mechanical behaviour and for cosmetic formulation design," *International journal of cosmetic science*, vol. 41, no. 3, pp. 292–299, 2019.

[86] B. Holt, A. Tripathi, and J. Morgan, “Viscoelastic response of human skin to low magnitude physiologically relevant shear,” *Journal of biomechanics*, vol. 41, no. 12, pp. 2689–2695, 2008.

[87] Z. Liu and K. Yeung, “The preconditioning and stress relaxation of skin tissue,” *Journal of Biomedical & Pharmaceutical Engineering*, vol. 2, no. 1, pp. 22–28, 2008.

[88] K. L. Johnson and K. L. Johnson, *Contact mechanics*. Cambridge university press, 1987.

[89] A. S. Évora, M. J. Adams, S. A. Johnson, and Z. Zhang, “Corneocytes: Relationship between structural and biomechanical properties,” *Skin Pharmacology and Physiology*, vol. 34, no. 3, pp. 146–161, 2021.

[90] M. S. Christensen, C. W. Hargens III, S. Nacht, and E. H. Gans, “Viscoelastic properties of intact human skin: instrumentation, hydration effects, and the contribution of the stratum corneum,” *Journal of Investigative Dermatology*, vol. 69, no. 3, pp. 282–286, 1977. Publisher: Elsevier.

[91] I. H. Blank, J. Moloney, A. G. Emslie, I. Simon, and C. Apt, “The Diffusion of Water Across the Stratum Corneum As a Function of Its Water Content,” *Journal of Investigative Dermatology*, vol. 82, pp. 188–194, Feb. 1984.

[92] S. M. Pasumarty, S. A. Johnson, S. A. Watson, and M. J. Adams, “Friction of the Human Finger Pad: Influence of Moisture, Occlusion and Velocity,” *Tribology Letters*, vol. 44, p. 117, Aug. 2011.

[93] T. André, V. Lévesque, V. Hayward, P. Lefèvre, and J.-L. Thonnard, “Effect of skin hydration on the dynamics of fingertip gripping contact,” *Journal of The Royal Society Interface*, vol. 8, pp. 1574–1583, Nov. 2011. Publisher: Royal Society.

[94] L. Pedersen and G. B. Jemec, “Mechanical properties and barrier function of healthy human skin,” *Acta dermato-venereologica*, vol. 86, no. 4, pp. 308–311, 2006. Publisher: Medical Journals Limited.

[95] G. Cavalli, S. Colafrancesco, G. Emmi, M. Imazio, G. Lopalco, M. C. Maggio, J. Sota, and C. A. Dinarello, “Interleukin 1α: a comprehensive review on the role of il-1α in the

pathogenesis and treatment of autoimmune and inflammatory diseases," *Autoimmunity reviews*, vol. 20, no. 3, p. 102763, 2021.

[96] M. A. Perkins, M. A. Osterhues, M. A. Farage, and M. K. Robinson, "A noninvasive method to assess skin irritation and compromised skin conditions using simple tape adsorption of molecular markers of inflammation," *Skin Research and Technology*, vol. 7, no. 4, pp. 227–237, 2001.

[97] J. Soetens, P. Worsley, D. Bader, and C. Oomens, "Investigating the influence of intermittent and continuous mechanical loading on skin through non-invasive sampling of il-1α," *Journal of Tissue Viability*, vol. 28, no. 1, pp. 1–6, 2019.

[98] L. A. de Wert, D. L. Bader, C. W. Oomens, L. Schoonhoven, M. Poeze, and N. D. Bouvy, "A new method to evaluate the effects of shear on the skin," *Wound Repair and Regeneration*, vol. 23, no. 6, pp. 885–890, 2015.

[99] H. Jayabal, B. M. Bates-Jensen, N. S. Abiakam, P. R. Worsley, and D. L. Bader, "The identification of biophysical parameters which reflect skin status following mechanical and chemical insults," *Clinical Physiology and Functional Imaging*, vol. 41, no. 4, pp. 366–375, 2021.

[100] H. Jayabal, D. L. Bader, and P. Worsley, "Development of an efficient extraction methodology to analyse potential inflammatory biomarkers from sebum," *Skin Pharmacology and Physiology*, 2022.

[101] S. Verdier-Sévrain and F. Bonté, "Skin hydration: a review on its molecular mechanisms," *Journal of cosmetic dermatology*, vol. 6, no. 2, pp. 75–82, 2007.

[102] F. Gioia and L. Celleno, "The dynamics of transepidermal water loss (tewl) from hydrated skin," *Skin research and technology*, vol. 8, no. 3, pp. 178–186, 2002.

[103] N. Abiakam, P. Worsley, H. Jayabal, K. Mitchell, M. Jones, J. Fletcher, F. Spratt, and D. Bader, "Personal protective equipment related skin reactions in healthcare professionals during covid-19," *International Wound Journal*, vol. 18, no. 3, pp. 312–322, 2021.

[104] J. Welzel, M. Bruhns, and H. H. Wolff, “Optical coherence tomography in contact dermatitis and psoriasis,” *Archives of dermatological research*, vol. 295, pp. 50–55, 2003.

[105] J. Welzel, C. Reinhardt, E. Lankenau, C. Winter, and H. Wolff, “Changes in function and morphology of normal human skin: evaluation using optical coherence tomography,” *British Journal of Dermatology*, vol. 150, no. 2, pp. 220–225, 2004.

[106] A. S. Évora, N. Abiakam, H. Jayabal, P. R. Worsley, Z. Zhang, S. A. Johnson, M. J. Adams, and D. L. Bader, “Characterisation of superficial corneocytes in skin areas of the face exposed to prolonged usage of respirators by healthcare professionals during covid-19 pandemic,” *Journal of Tissue Viability*, 2023.

[107] A. Caro-Bretelle, P. Gountsop, P. Ienny, R. Léger, S. Corn, I. Bazin, and F. Bretelle, “Effect of sample preservation on stress softening and permanent set of porcine skin,” *Journal of biomechanics*, vol. 48, no. 12, pp. 3135–3141, 2015.

[108] Y. Lanir and Y. Fung, “Two-dimensional mechanical properties of rabbit skin—ii. experimental results,” *Journal of biomechanics*, vol. 7, no. 2, pp. 171–182, 1974.

[109] A. Kalra, A. Lowe, and A. A. Jumaily, “An overview of factors affecting the skins youngs modulus,” *J. Aging Sci*, vol. 4, no. 2, p. 1000156, 2016.

[110] M. L. Crichton, B. C. Donose, X. Chen, A. P. Raphael, H. Huang, and M. A. Kendall, “The viscoelastic, hyperelastic and scale dependent behaviour of freshly excised individual skin layers,” *Biomaterials*, vol. 32, no. 20, pp. 4670–4681, 2011.

[111] R. Sanders, “Torsional elasticity of human skin in vivo,” *Pflügers Archiv*, vol. 342, pp. 255–260, 1973.

[112] E. Jacquet, S. Joly, J. Chambert, K. Rekik, and P. Sandoz, “Ultra-light extensometer for the assessment of the mechanical properties of the human skin in vivo,” *Skin research and technology*, vol. 23, no. 4, pp. 531–538, 2017.

[113] S. Luebberding, N. Krueger, and M. Kerscher, “Mechanical properties of human skin in vivo: a comparative evaluation in 300 men and women.,” *Skin research and technology:*

official journal of International Society for Bioengineering and the Skin (ISBS)[and] International Society for Digital Imaging of Skin (ISDIS)[and] International Society for Skin Imaging (ISSI), vol. 20, no. 2, pp. 127–135, 2013.

[114] M. J. Blair, J. D. Jones, A. E. Woessner, and K. P. Quinn, "Skin structure–function relationships and the wound healing response to intrinsic aging," *Advances in wound care*, vol. 9, no. 3, pp. 127–143, 2020.

[115] F. Giraud, M. Amberg, B. Lemaire-Semail, and C. Giraud-Audine, "Using an ultrasonic transducer to produce tactile rendering on a touchscreen," in *2014 Joint IEEE International Symposium on the Applications of Ferroelectric, International Workshop on Acoustic Transduction Materials and Devices & Workshop on Piezoresponse Force Microscopy*, pp. 1–4, IEEE, 2014.

[116] E. Enferad, C. Giraud-Audine, F. Giraud, M. Amberg, and B. L. Semail, "Generating controlled localized stimulations on haptic displays by modal superimposition," *Journal of Sound and Vibration*, vol. 449, pp. 196–213, 2019.

[117] T. Sednaoui, E. Vezzoli, B. Dzidek, B. Lemaire-Semail, C. Chappaz, and M. Adams, "Friction reduction through ultrasonic vibration part 2: Experimental evaluation of intermittent contact and squeeze film levitation," *IEEE Transactions on Haptics*, vol. 10, no. 2, pp. 208–216, 2017.

[118] L. Winfield, J. Glassmire, J. E. Colgate, and M. Peshkin, "T-pad: Tactile pattern display through variable friction reduction," in *Second Joint EuroHaptics Conference and Symposium on Haptic Interfaces for Virtual Environment and Teleoperator Systems (WHC'07)*, pp. 421–426, IEEE, 2007.

[119] R. F. Friesen, M. Wiertlewski, and J. E. Colgate, "The role of damping in ultrasonic friction reduction," in *2016 IEEE Haptics Symposium (HAPTICS)*, pp. 167–172, Apr. 2016. ISSN: 2324-7355.

[120] J. Monnoyer, E. Diaz, C. Bourdin, and M. Wiertlewski, "Optimal skin impedance pro-

motes perception of ultrasonic switches," in *2017 IEEE World Haptics Conference (WHC)*, pp. 130–135, June 2017.

[121] F. J. Fuchs, "Ultrasonic cleaning and washing of surfaces," in *Power Ultrasonics* (J. A. Gallego-Juárez and K. F. Graff, eds.), pp. 577–609, Woodhead Publishing, 2015.

[122] P. M. Leung, "Performance characteristics of langevin type sonar transducer made from pzt type 1 ceramic," *Ferroelectrics*, vol. 28, no. 1, pp. 355–358, 1980.

[123] T. Inui, Y. Kurashina, C. Imashiro, and K. Takemura, "Method of localized removal of cells using a bolt-clamped langevin transducer with an ultrasonic horn," *Engineering in Life Sciences*, vol. 19, no. 8, pp. 575–583, 2019.

[124] T. Harada, N. Ishikawa, T. Kanda, K. Suzumori, Y. Yamada, and K.-I. Sotowa, "Droplet generation using a torsional langevin-type transducer and a micropore plate," *Sensors and Actuators A: physical*, vol. 155, no. 1, pp. 168–174, 2009.

[125] T. J. Mason, "Ultrasound in synthetic organic chemistry," *Chemical Society Reviews*, vol. 26, no. 6, pp. 443–451, 1997. Publisher: The Royal Society of Chemistry.

[126] A. Manbachi and R. S. C. Cobbold, "Development and application of piezoelectric materials for ultrasound generation and detection," *Ultrasound*, vol. 19, no. 4, pp. 187–196, 2011. Publisher: SAGE Publications.

[127] T. Harada, N. Ishikawa, T. Kanda, K. Suzumori, Y. Yamada, and K.-I. Sotowa, "Droplets generation by a torsional bolt-clamped langevin-type transducer and micropore plate," in *2008 IEEE Ultrasonics Symposium*, pp. 627–630, 2008. ISSN: 1051-0117.

[128] T. Nishimura, H. Hosaka, and T. Morita, "Resonant-type smooth impact drive mechanism (SIDM) actuator using a bolt-clamped langevin transducer," *Ultrasonics*, vol. 52, no. 1, pp. 75–80, 2012.

[129] S. Ghenna, E. Vezzoli, C. Giraud-Audine, F. Giraud, M. Amberg, and B. Lemaire-Semail, "Enhancing variable friction tactile display using an ultrasonic travelling wave," *IEEE Transactions on Haptics*, vol. 10, no. 2, pp. 296–301, 2017.

[130] J. Kim and J. Lee, “Parametric Study of Bolt Clamping Effect on Resonance Characteristics of Langevin Transducers with Lumped Circuit Models,” *Sensors*, vol. 20, p. 1952, Jan. 2020. Number: 7 Publisher: Multidisciplinary Digital Publishing Institute.

[131] R. Krimholtz, D. A. Leedom, and G. L. Matthaei, “New equivalent circuits for elementary piezoelectric transducers,” *Electronics Letters*, vol. 13, no. 6, pp. 398–399, 1970.

[132] H. Jin, S. Dong, J. K. Luo, and W. Milne, “Generalised butterworth-van dyke equivalent circuit for thin-film bulk acoustic resonator,” *Electronics Letters*, vol. 47, no. 7, pp. 424–426, 2011.

[133] P. Fabijanski and R. Lagoda, “Modeling and identification of parameters the piezoelectric transducers in ultrasonic systems,” *Advances in Ceramics-Electric and Magnetic Ceramics, Bioceramics, Ceramics and Environment*, pp. 155–176, 2011.

[134] F. J. Arnold and P. S. Martins, “New insights into the mechanical pre-stressing of piezotransducers,” *Journal of Intelligent Material Systems and Structures*, vol. 32, pp. 867–879, May 2021. Publisher: SAGE Publications Ltd STM.

[135] M. Takasaki, Y. Maruyama, and T. Mizuno, “Resonance frequency tracing system for langevin type ultrasonic transducers,” in *2007 International Conference on Mechatronics and Automation*, pp. 3817–3822, 2007.

[136] D. Guyomar, N. Aurelle, and L. Eyraud, “Piezoelectric ceramics nonlinear behavior. application to langevin transducer,” *Journal de Physique III*, vol. 7, no. 6, pp. 1197–1208, 1997.

[137] M. Samal, P. Seshu, S. Parashar, U. Von Wagner, P. Hagedorn, B. Dutta, and H. Kushwaha, “Nonlinear behaviour of piezoceramics under weak electric fields: Part-i: 3-d finite element formulation,” *International Journal of Solids and Structures*, vol. 43, no. 6, pp. 1422–1436, 2006.

[138] T. Instruments, “LM675 data sheet, product information and support,” Datasheet SNOSBP3E, Texas Instruments, Mar. 2013.

[139] F. Giraud and C. Giraud-Audine, *Piezoelectric actuators: Vector control method: Basic, Modeling and mechatronic design of ultrasonic devices*. Butterworth-Heinemann, 2019. Google-Books-ID: gWWTDwAAQBAJ.

[140] S. Ghenna, F. Giraud, C. Giraud-Audine, and M. Amberg, "Vector control of piezoelectric transducers and ultrasonic actuators," *IEEE Transactions on Industrial Electronics*, vol. 65, no. 6, pp. 4880–4888, 2018. Conference Name: IEEE Transactions on Industrial Electronics.

[141] J. C. Cohen, J. C. Makous, and S. J. Bolanowski, "Under which conditions do the skin and probe decouple during sinusoidal vibrations?," *Experimental Brain Research*, vol. 129, pp. 211–217, Nov. 1999.

[142] M. Wiertlewski and V. Hayward, "Mechanical behavior of the fingertip in the range of frequencies and displacements relevant to touch," *Journal of Biomechanics*, vol. 45, pp. 1869–1874, July 2012.

[143] A. N. Gent, "On the relation between indentation hardness and young's modulus," *Rubber Chemistry and Technology*, vol. 31, no. 4, pp. 896–906, 1958.

[144] E. M. Sales de Castro, F. Giraud, B. Lemaire-Semail, and M. Amberg, "Vector Controlled Ultrasonic Transducer Applied to Soft Material Mechanical Impedance Estimation," in *2021 IEEE International Workshop of Electronics, Control, Measurement, Signals and their application to Mechatronics (ECMSM)*, pp. 1–5, June 2021.

[145] N. Huloux, C. Bernard, and M. Wiertlewski, "Estimating friction modulation from the ultrasonic mechanical impedance," *IEEE Transactions on Haptics*, vol. 14, no. 2, pp. 409–420, 2021.

[146] Fujicera, "Product line-up," 2022.

[147] V. T. Rathod, "A review of acoustic impedance matching techniques for piezoelectric sensors and transducers," *Sensors*, vol. 20, no. 14, p. 4051, 2020.

[148] R. O. Potts, E. M. Buras Jr, and D. A. Chrisman Jr, "Changes with age in the moisture content of human skin," *Journal of investigative dermatology*, vol. 82, no. 1, pp. 97–100, 1984.

[149] C.-K. Hsu, N.-Y. Cheng, C.-C. Yang, Y.-Y. Yen, and S.-H. Tseng, "Investigating the clinical implication of corneometer and mexameter readings towards objective, efficient evaluation of psoriasis vulgaris severity," *Scientific reports*, vol. 12, no. 1, p. 7469, 2022.

[150] P.-G. Sator, J. B. Schmidt, and H. Hönigsmann, "Comparison of epidermal hydration and skin surface lipids in healthy individuals and in patients with atopic dermatitis," *Journal of the American Academy of Dermatology*, vol. 48, no. 3, pp. 352–358, 2003.

[151] J. MØSS, "The effect of 3 moisturisers on skin surface hydration: Electrical conductance (skicon-200), capacitance (corneometer cm420), and transepidermal water loss (tewl)," *Skin Research and Technology*, vol. 2, no. 1, pp. 32–36, 1996.

[152] K. Shirai and Y. Yamamoto, "Changes in the water content of the corneal layer of newborn infants using a corneometer," in *The 15th International Conference on Biomedical Engineering: ICBME 2013, 4th to 7th December 2013, Singapore*, pp. 821–824, Springer, 2014.

[153] C. K. Sen, G. M. Gordillo, S. Roy, R. Kirsner, L. Lambert, T. K. Hunt, F. Gottrup, G. C. Gurtner, and M. T. Longaker, "Human skin wounds: a major and snowballing threat to public health and the economy," *Wound repair and regeneration*, vol. 17, no. 6, pp. 763–771, 2009.

[154] Z. Hanusz and J. Tarasińska, "Normalization of the kolmogorov–smirnov and shapiro–wilk tests of normality," *Biometrical Letters*, vol. 52, no. 2, pp. 85–93, 2015.

[155] E. L. Lehmann and H. D'Abrera, "Statistical methods based on ranks," *Nonparametrics. San Francisco, CA, Holden-Day*, 1975.

[156] L. GraphPad Software, "Prism 9 user guide," 2019.

[157] J. Adler and I. Parmryd, "Quantifying colocalization by correlation: the pearson correlation coefficient is superior to the mander's overlap coefficient," *Cytometry Part A*, vol. 77, no. 8, pp. 733–742, 2010.

[158] J. Sandby-Moller, T. Poulsen, and H. C. Wulf, "Epidermal thickness at different body sites: relationship to age, gender, pigmentation, blood content, skin type and smoking habits," *Acta Dermato Venereologica*, vol. 83, no. 6, pp. 410–413, 2003.

[159] Z. Ya-Xian, T. Suetake, and H. Tagami, "Number of cell layers of the stratum corneum in normal skin–relationship to the anatomical location on the body, age, sex and physical parameters," *Archives of dermatological research*, vol. 291, pp. 555–559, 1999.

[160] E. Jacquet, J. Chambert, J. Pauchot, and P. Sandoz, "Intra-and inter-individual variability in the mechanical properties of the human skin from in vivo measurements on 20 volunteers," *Skin Research and Technology*, vol. 23, no. 4, pp. 491–499, 2017.

[161] K. Cowley and K. Vanoosthuyze, "The biomechanics of blade shaving," *International journal of cosmetic science*, vol. 38, pp. 17–23, 2016.

[162] M. Maurer, M. Rietzler, R. Burghardt, and F. Siebenhaar, "The male beard hair and facial skin–challenges for shaving," *International journal of cosmetic science*, vol. 38, pp. 3–9, 2016.

[163] "Tips on How to Care for Your Healing Wound | BAND-AID® Brand."

L2EP
Laboratoire d'électrotechnique et d'électronique de puissance de Lille

Titre: Dispositif à ultrasons basse fréquence pour le diagnostic précoce des escarres par impédance mécanique de la peau

Mots clés: Diagnostic, Ultrasons basse fréquence, Piézoélectrique, Escarres, Capteur, Contrôle vectoriel

Résumé: L'intégrité de la peau est un sujet important pour les soins de santé. Les lésions provoquées par la pression, le cisaillement et la friction sur les proéminences osseuses, entre autres conditions, constituent une menace pour la santé de la peau. Ces plaies, notamment les escarres, sont longues et coûteuses à traiter, ce qui nuit à la qualité de vie des patients et coûte cher au système de santé. Jusqu'à présent, le diagnostic de l'escarre repose sur des méthodes imprécises, reposant sur la subjectivité du personnel soignant. STINTS, un réseau européen de formation financé par l'action Marie Skodowska-Curie, a proposé divers projets dans le but de comprendre les voies biomécaniques et biochimiques complexes entraînant la perte de l'intégrité cutanée, dont le projet présenté dans cette thèse. L'objectif de ce travail est de développer un nouveau dispositif de détection précoce des PU. L'impédance mécanique mesurée par approche ultrasonore basse fréquence est encore inexplorée dans le domaine des plaies chroniques. L'appareil développé a été utilisé pour analyser les données sur les participants en bonne santé, afin de créer un ensemble de données pour une peau saine. Des tests modifiant certaines conditions de la peau, telles que l'hydratation et la création d'un microclimat, ont été étudiés et des mesures de la mécanique cutanée et d'autres paramètres, tels que l'humidité et la perte d'eau transépidermique, ont été effectuées. Les résultats de ces tests, sur peau saine, indiquent une association entre les paramètres cutanés et les mesures mécaniques. Cette étude n'a cependant pas pris en compte les patients à risque réel d'escarre. D'autres études sont nécessaires pour étudier plus en détail l'aspect diagnostique.

Title: Low-Frequency Ultrasound Device for Pressure Ulcers Early Stage Diagnosis by Skin Mechanical Impedance

Keywords: Diagnosis, Low-Frequency Ultrasound, Piezoelectric, Pressure Ulcer, Sensor, Vector Control

Abstract: An important topic for the healthcare is skin integrity. Lesions brought on by pressure, shear, and friction over bony prominences, among other conditions, pose a threat to skin health. These wounds, namely Pressure Ulcers, take a long time and a lot of money to treat, which is bad for the patients' quality of life and expensive for the healthcare system. So far, PU diagnosis is made using imprecise methods, relying on the subjectivity of the healthcare staff. STINTS, a European Training Network funded by the Marie Skodowska-Curie Action, proposed various projects with the aim of comprehending the intricate biomechanical and biochemical pathways resulting in the loss of skin integrity, including the project presented in this thesis. The aim of this work is to develop a new device for early stage PU detection. The mechanical impedance measured through low-frequency ultrasound approach is yet unexplored in the field of chronic wounds. The device developed was used to analyse the data on healthy participants, to create a data set for healthy skin. Tests changing certain conditions of skin, such as hydration and microclimate creation were investigated and measurements of skin mechanics and other parameters, such as moisture and trans epidermal water loss were made. The findings from these tests, on healthy skin, indicate an association between skin parameters and the mechanical measurements. This study, however, has not taken into consideration patients in real risk of PU. Further studies are needed to investigate the diagnostic aspect in more detail.

Université de Lille
L2EP / IRCICA
50 Avenue Halley, 59650 Villeneuve-d'Ascq, France